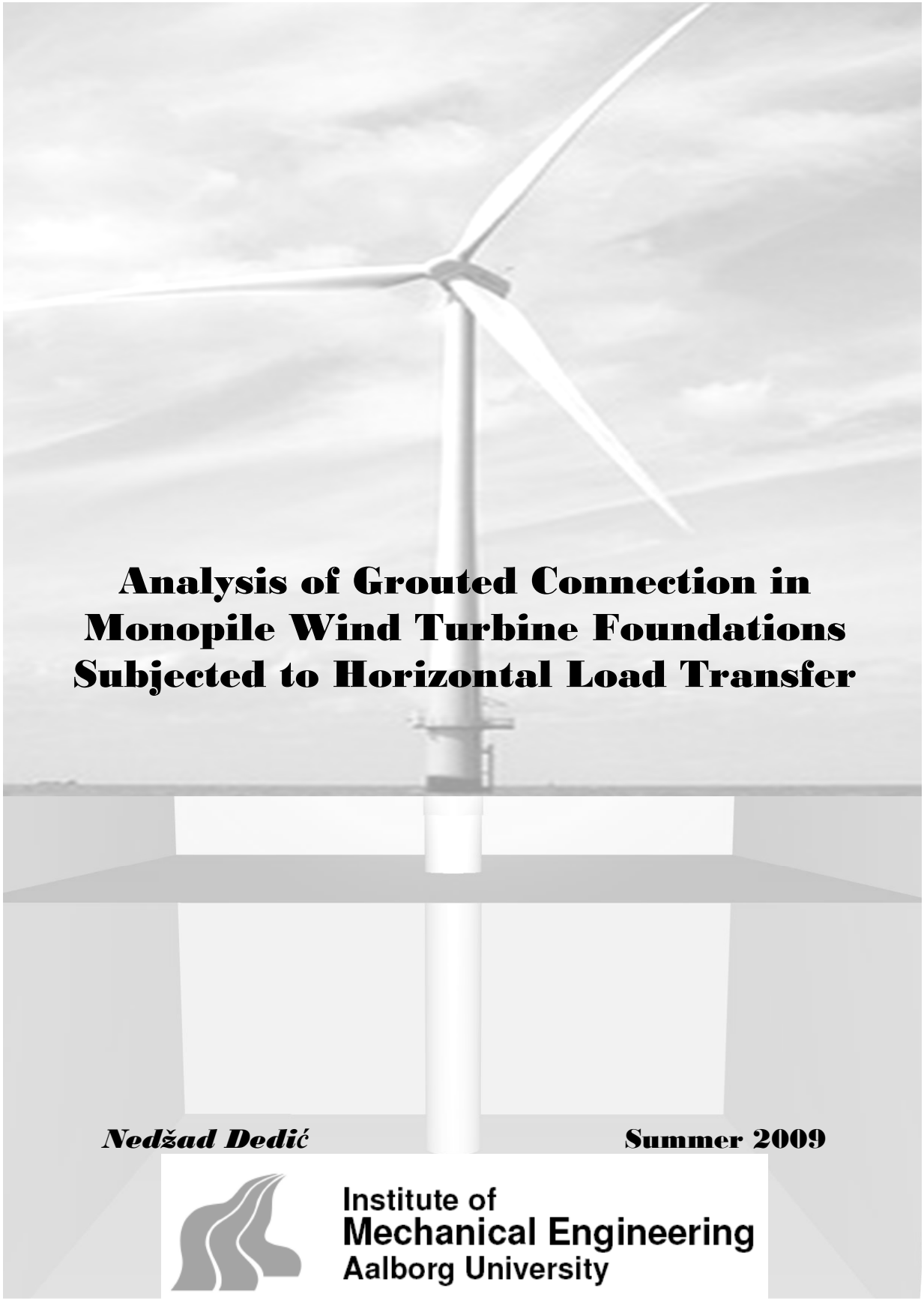

Analysis of Grouted Connection in Monopile Wind Turbine Foundations Subjected to Horizontal Load Transfer

Nedžad Dedić

Summer 2009

Institute of
Mechanical Engineering
Aalborg University

Aalborg University
Institute of Mechanical Engineering

Pontoppidanstraede 101 ▪ DK-9220 Aalborg East Denmark Phone +45 96 35 80 80

Title:

Analysis of Grouted Connection in Monopile Wind Turbine Foundations Subjected to Horizontal Load Transfer

Semester Theme:

Design of Mechanical Systems

Project Period:

February 1st – June 2nd 2009

Project Group:

DMS10, 48J

Group Members:

Nedžad Dedić

Supervisor:

Sergey V. Sorokin

Number of Prints:

3

Number of pages:

77

Enclosures and Appendices:

9 Appendices, 1 CD

This page is intentionally left blank.

CONTENTS

PREFACE

This report is submitted to the Institute of Mechanical Engineering at Aalborg University, Aalborg, DK, and conducted as a partial fulfilment of the requirements for the Master of Science degree within the Design of Mechanical Systems (DMS). The project underlying this report is carried out from February 1st to June 2nd 2009 and is originally proposed by the company ISC Consulting Engineers A/S (ISC), who outlined the project theme, being of current interest in the offshore industries.

The proposed project concerns one of the foundation methods for offshore wind turbines at water depths up to 30 meters, known as *monopile* foundations. These foundations contain pile-sleeve connections that basically consist of two concentric steel pipes cast together by means of high strength concrete. The statutory construction and documentation procedures for such connections are standardized by e.g. Det Norske Veritas (DNV). It is observed that the design formulae in the relevant DNV standard are established for the vertical load transfer in the connection only. So far, this standard refers to Finite Element Analyses (FEA) and experimental methods in order to account for the horizontal load transfer. Consequently, the objective of this report is to analyse a specific connection subjected to horizontal load transfer, in order to establish more general parametric formulations of the field equations. This attempt is carried out by performing analytical 3D analysis based on continuum mechanics, which is compared to a corresponding numerical analysis by means of FEM. The input needed for the analyses is provided by ISC, corresponding to a specific connection used for a 2 *MW* wind turbine at Gunfleet Sands offshore wind farm, DK, owned by DONG Energy A/S.

The literature referencing throughout the report is given as [Author/Source, publication year] and elaborated in the reference list. Selected project related documentation and information is enclosed as appendix, while all program codes, Computer Aided Design (CAD) models, as well as a digital copy of the report are enclosed on a Compact Disc (CD), attached at the back of this report. References to material enclosed on the CD are also detailed in the reference list.

TEXT ARRANGEMENT

Chapter 1: Introduction

The general background of the foundation methods and considerations for offshore wind turbines is introduced in this chapter. Different foundation methods are briefly reviewed, leading to a more specific elaboration of the monopile foundation structure. Subsequently, the overall problem presentation is given, leading to the governing problem statement to be addressed. The chapter is completed by introducing several simplifications and limitations, in order to reduce the complexity of the structure to be analysed.

Chapter 2: Analytical Analysis of the Grouted Connection

The goal of this chapter is to apply the theory of elasticity to characterize a general case of a continuous elastic medium and its response to applied loads, and subsequently apply this to the specific connection in the monopile foundation. Although the initial objective is to account for static results, it is chosen to seek a formulation which involves a dynamic source as well. Therefore, elastodynamic field equations are formulated by which the fundamental boundary value problems can be solved. Next, the potential theory is introduced, which makes it possible to uncouple and express the problem by means of harmonic functions. The proceeding analytical solution is carried out by first considering a simplified 2D elastostatic case and gradually advancing into 3D elastodynamic formulation. Finally, a general expression for the stiffness of the connection, in terms of the obtained stress state, is formulated.

Chapter 3: Finite Element Analysis of the Grouted Connection

The objective of this chapter is to support and verify the analytical results obtained in the previous chapter. The analytical procedures, conditioned by the assumed simplifications, are generally presumed to be more accurate than the numerical methods dealing with discretized models. Through the discretization process, the method sets up an algebraic system of equations for unknown nodal values that merely approximates the continuous solution. However, it is found essential to include FEA in order to provide additional benchmarking for the final conclusion addressing the problem statement. The results obtained by FEA will be compared to the corresponding results from the analytical solution in this chapter as well.

Chapter 4: Discussion

The content in this chapter is evaluation of the obtained results with respect to the posed simplifications and limitations in relation to the original problem. The different assumptions are discussed in order to identify the reservations combined with the proposed mathematical models and solution procedures. Consequently, the quality of the final results will be graded and several ideas for further improvements will be given.

Chapter 5: Conclusion

The final remarks are presented and the overall conclusion for the methodology applied in the project is drawn in this chapter.

ABSTRACT

The constant improvement of offshore wind energy generation has resulted in more efficient, but also larger and heavier offshore wind turbines. Different foundations for these have been developed for different sea depths and one of the most popular is the *monopile* foundation, suitable for water depths up to 30 *m*. It involves steel tubing connected by means of high strength grout. This technology is known from offshore oil- and gas platforms, primarily used to carry vertical loads. However, the primary loads related to wind turbines are the wind and wave induced vibrations and consequently overturning moments. Design guidance for such connections is standardized by Det Norske Veritas, who have developed several parametric design formulae. Nevertheless, these solely comprise formulations for vertical load transfer, while horizontal load transfer is advised to be addressed numerically or/and experimentally.

The overall objective of this work is to generalize the structural behaviour in the grouted connection subjected to a static horizontal load based on a specific connection used at Gunfleet Sands Offshore Wind Farm, DK. This is done by deriving an approximate analytical solution and verifying it by a corresponding numerical solution. The analytical solution is based on derivation of governing field equations that describe the mechanical response of the grout. This is done by considering the connection as a 3D boundary value problem and approximating the displacement boundary conditions, whereby the problem is reduced to a displacement formulation. Although the static effects are of interest, it is chosen to derive this as an elastodynamic formulation in terms of the equations of motion. This leads to a coupled formulation of the problem, which is resolved by introducing an uncoupled expression of the displacement field, based on potential functions. Substitution of this field leads to a problem given by two wave equations. The solution to these is conducted by first considering a 2D formulation and gradually advancing into 3D. The approximate boundary conditions are finally applied, thus solving for the displacement field and thereby the entire boundary value problem. Subsequently, the obtained solution is compared to a corresponding Finite Element Analysis (FEA), carried out in FE computer program ANSYS. Furthermore, the assumptions made in the two analyses are compared to results from a similar but more advanced FEA, carried out by an external source.

The outcome of the analytical analysis is a parametric computer program which approximately yields displacements, strains and stresses at any point of the geometry. The program results are verified by the corresponding FEA with a reasonable agreement. The errors involved are not entirely negligible at all points in the structure, but very reasonable considering the approximated boundary conditions. Additionally, it is demonstrated that the elastodynamic formulation can be applied to elastostatic problems, provided that the applied dynamic disturbance is sufficiently low. Hereby, the statement that considering elastostatics as a limit of elastodynamics is a complete nonsense [Olsson, 1984] has been disconfirmed.

ACKNOWLEDGEMENTS

I grant the deepest gratitude to my supervisor Professor, Ph.D, D.Sci. Sergey V. Sorokin from the Department of Mechanical Engineering at Aalborg University, whose passion and enthusiasm for science has encouraged me to attempt and complete many of the sophisticated tasks within this project. His numerous suggestions and instructions have been invaluable.

I would also like to thank M.Sc. Andreas Laundgaard from ISC Consulting Engineers A/S for the original project proposal and indispensable input for the project. Furthermore, I express my gratitude to the Associate Professor Ph.D. Eigil V. Sørensen from the Department of Civil Engineering at Aaalborg University, who has provided important information and references on the topic of high strength concrete.
At last but not at least, I devote innermost appreciation to my fiancé Edisa, whose love and support during the preparation of this report has been precious.

LIST OF SYMBOLS

a_i	Acceleration vector
c	Phase speed
c_i	Integration constants
$\vec{i}, \vec{j}, \vec{k}$	Unit vectors for rectangular coordinates
$\vec{i}_r, \vec{i}_\theta, \vec{i}_z$	Unit vectors for cylindrical coordinates
f	Function, functional
g	Function, gap
i	Complex number
k	Wave number, rotational stiffness
r	Radial cylindrical coordinate
t	Time dimension
u_0	Initial deflection
$\vec{u}$	Displacement field
v_i	Velocity vector
z	Longitudinal cylindrical coordinate
A,...,D	Integration constants
B_i	Body forces
E_S	Young's Modulus of elasticity of steel
E_G	Young's Modulus of elasticity of grout
F_i	Resulting forces
I	Area moment of inertia
I_n	Modified Bessel function
J_n	Ordinary Bessel function
K_n	Modified Bessel function
L_G	Length of grouted connection
M	Moment
P	Concentrated force
T_i	Traction forces
U	Internal strain energy
U_0	Strain energy density
V	Volume
Y_n	Ordinary Bessel function
$\{d\}$	Nodal DOF vector
$[k]$	Element stiffness matrix
$\{r_e\}$	Nodal load vector
$\{u\}$	Displacement vector
$[B]$	Strain-displacement matrix
$[D]$	Global DOF matrix
$[E]$	Constitutive matrix
$\{F\}$	Volumetric load vector
$[K]$	Global stiffness matrix
$[L]$	Local-global displacement relation matrix
$[N]$	Shape function matrix
$\{P\}$	Vector of concentrated forces
$\{R\}$	Global load vector
$\{T\}$	Surface tractions vector
$[\partial]$	Differential operator matrix
α	Primary/longitudinal phase speed
β	Secondary/shear wave speed
δ	Kronecker's altering symbol
λ	Lamé elastic constant
γ	Rotation angle
θ	Angular cylindrical coordinate
μ	Shear modulus / Lamé elastic constant
ν	Poisson's ratio
ρ	Material density
ε_{ij}	Strain tensor
ε_0	Initial strains
σ_{ij}	Stress tensor
σ_0	Initial stresses
φ	Scalar potential function
$\vec{\psi}$	Vector potential function
ω	Angular frequency
Π_p	Total potential energy
Ω	Potential of externally applied loads
∇	Gradient operator
Δ	Laplace's operator

Chapter 1

1. Introduction

Wind energy generation by means of wind turbines has proven to be of great value for large scale future investment in the energy industries worldwide. A constant search for greater wind potential has pushed the industry from onshore towards offshore solutions with superior wind conditions. Aiming for more effective wind conditions corresponds to seeking for more remote offshore sites and consequently higher sea depths. Installing the wind turbines at such depths involves high stakes and high expenses, both from the financial and the engineering point of view. Nonetheless, several different foundation structures for various sea depths and soil conditions have been proposed for the offshore wind turbines. Among many excellent proposals for water depths up to 30 *m*, one specific foundation type has proven its effectiveness considering both the structural simplicity, manufacturing and installation expenses. This type of foundation is known as *monopile* foundation. One of the biggest offshore wind farms with 80 Vestas 2 *MW* wind turbines is Horns Rev near Esbjerg, DK, where all turbines are founded on such monopiles. Furthermore, around 75 % of all installations to date are founded on monopiles [Densit, 2009].

Prior to a more precise problem presentation, different types of foundations and some of the governing factors that the designer should account for are compared and introduced in the following section, respectively. Subsequently, the monopile foundation is characterized in detail in order to enlighten the problem treated in the remainder of this report.

1.1 Foundation of Offshore Wind Turbines

One of the major problems encountered in relation to offshore wind turbine foundations is the connection of the structure to the ground and in particular how the loads applied to the structure should safely be transferred to the surrounding soil. Furthermore, both offshore wind turbines and their foundation structures must be more reliable than onshore due to higher service and repair costs at such sites. As stated earlier, several different solutions have been developed for different water depths, all of which meet these criteria. The main concepts are illustrated in Figure 1-1.

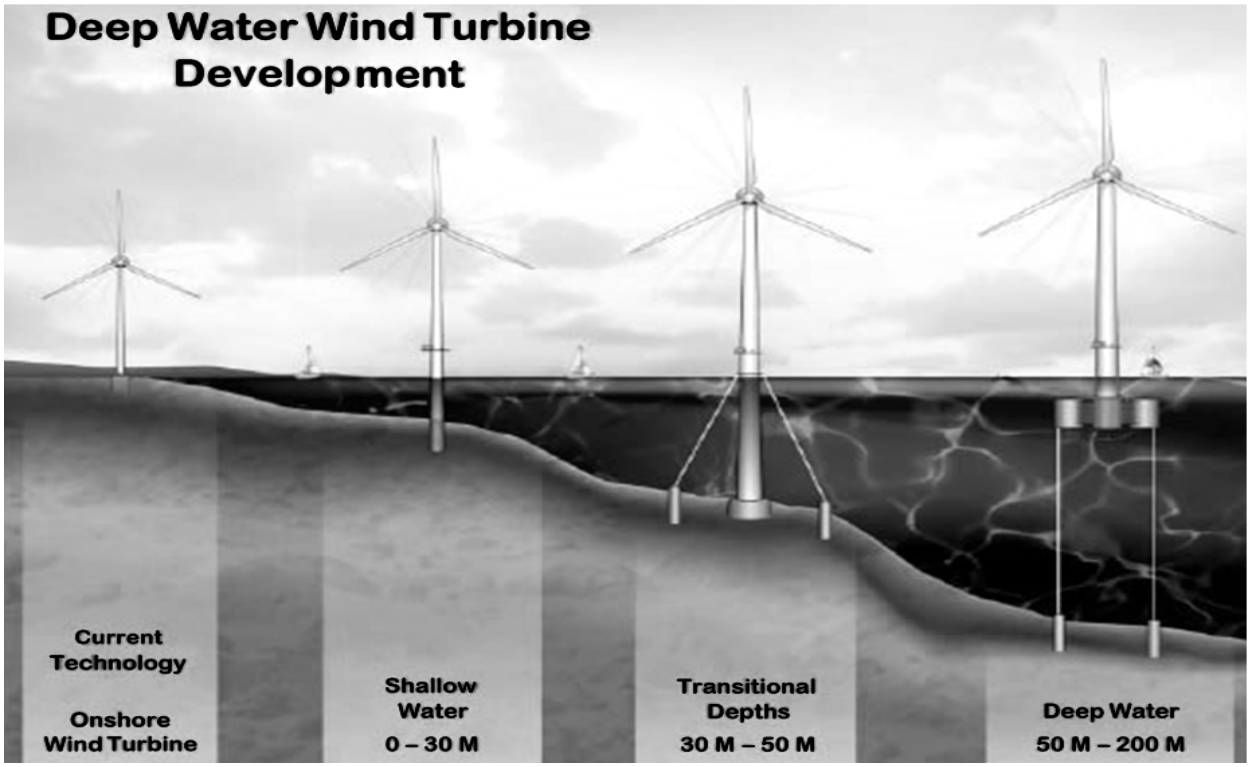

Figure 1-1: Foundation structure characterization for offshore wind turbines [OffshoreWind, 2009].

As illustrated in Figure 1-1, water depth is one of the driving variables for the design of offshore foundation structures. Locations with shallow waters reaching up to 30 *m* depth allow for relatively simple structures with no need for specific reinforcements, as depicted. Exceeding this depth towards transitional depths up to 50 *m* introduces larger stability problems due to greater tidal and wave effects, demanding more sophisticated solutions. Finally, founding structures directly to the seabed at depths above 50 *m* is both costly and impractical, which is why several floating solutions have been proposed that rely on buoyancy of the structure to resist overturning. One disadvantage in these is the floating motion which raises additional dynamic loads to the structure. Thus, in despite of the larger wind potential at such depths far from shore, these solutions are still under development and mostly on the prototype basis [OffshoreWind, 2009].

Consequently, foundations at shallow and transitional water depths are used in most of the offshore wind projects to date. Some of the different structures used at these locations are depicted in Figure 1-2 and subsequently briefly reviewed. A more detailed description can be found in e.g. [WindEnergy, 2009].

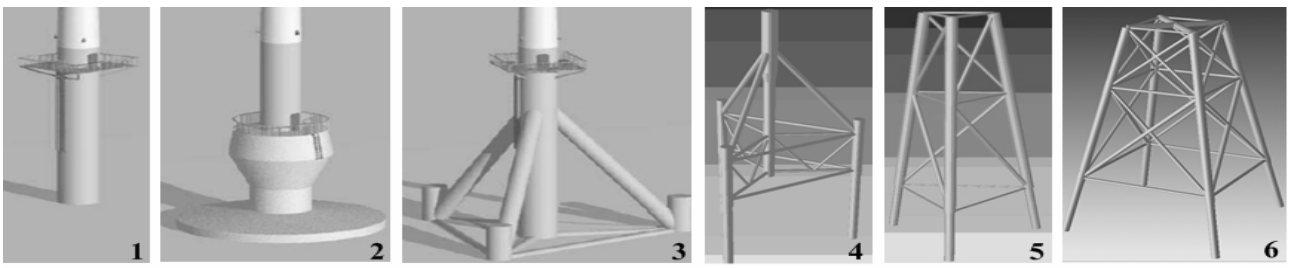

Figure 1-2: Typical structures for shallow (1,2,3) *and transitional* (4,5,6) *water depths.*

Structure 1 – Monopile Foundation

This is a simple structure consisting of a steel pipe piled into the seabed by driving and/or drilling methods. A larger diameter sleeve is attached to the pile by concrete casting, where its top rim is a flange that accommodates fixation of the turbine tower by bolting.

Structure 2 – Gravity Based Foundation

This structure is currently used on most offshore wind projects at shallow water depths up to 5 *m*. It consists of a large base constructed from steel and concrete, resting on the seabed. It relies on weight of the structure to resist overturning; hence the turbine is dependent on gravity to remain erect. The structure is resistant to scour and deformation due to its massive weight. The wind turbine tower is attached similarly to monopile foundations.

Structure 3 – Tripod Foundation

This design is typically used for platforms in the oil and gas industry. It is made from steel tubes welded together, typically 1 to 2.5 *m* in diameter. It is anchored 20 to 40 *m* into the seabed by means of driven or drilled piles from 1 to 2.5 *m* in diameter. The transition piece is typically attached onto the centre column by means of concrete casting as well.

Structures 4, 5, 6 – Jacket Foundations

Jacket structures are made from steel tubes, typically 0.5 – 1.5 *m* in diameter, welded together to from a structure similar to lattice towers. They are anchored to the seabed by driven or drilled piles, ranging from 1 – 2.5 *m* in diameter. Several 3 to 4 legged jacket structures have been proposed as illustrated in Figure 1-2.

1.2 General Design Choice Considerations

Choosing the appropriate design from the previously reviewed foundation structures could be assisted by considering the following overall design inputs:

- Water depth and soil conditions to determine the appropriate foundation structures, as well as if reinforcement is needed
- Turbine loads and wave loads to determine the overall size of the structure and the extent of reinforcement
- Manufacturing and installation demands based on statutory requirements and expected lifetime

In addition to the abovementioned, the economic perspective must be considered as well. Ooffshore wind farms are in general more expensive than onshore farms due to foundation costs, access difficulties, water depths, weather delays, and corrosion protection requirements. Nevertheless, offshore wind farms offer up to 40 % more energy potential due to higher wind speeds and less turbulence which counterbalances the investment costs [Irvine et. al., 2003]. Furthermore, the public opinion is no less important. It has often played a role for site locations near shore, as improper designs could interfere with the surrounding ambient. The

visual impact that the turbines have on the horizon is important, as e.g. 64 *m* tall turbine is visible above the horizon almost 40 *km* away. Additionally, beacons may be required to alert airlines and ships at night [Rogers et. al., 2003].

Consequently, the choice of the foundation design has to be considered from many aspects, but both the public opinion and investment costs agree with simple and discrete foundation structures. It is conspicuous that the monopile foundation structure in Figure 1-2 appears quite simple compared to the other designs. This is also the reason for its popularity in the majority of projects located at water depths up to 30. The certification company DNV covers the technical documentation for such structures with a set of design rules given in the standard [DNV-OS-J101, 2007] – Design of Offshore Wind Turbine Structures. Detailed elaboration of a monopile foundation and the overall design criteria according to this standard are given in the next section.

1.3 Monopile Foundation Structure

Monopile foundations have been used for offshore oil and gas platform foundation for decades. In this context, they are known as pile-sleeve connections. A pile-sleeve connection consists of a sleeve mounted concentrically on a pile that is driven into the seabed, with the larger diameter sleeve placed around the smaller diameter pile forming annuli between them. The connection is finally fixed by filling these annuli with specially developed grout that settles into high strength concrete. This technology has been transferred to the offshore wind turbines by utilizing the improved properties of the reinforced grout. The sleeve related to wind turbines is also known as transition piece, as it joins the wind turbine tower to the pile. An illustration of the grouted connection concept, as well as images of an installed structure is shown in Figure 1-3.

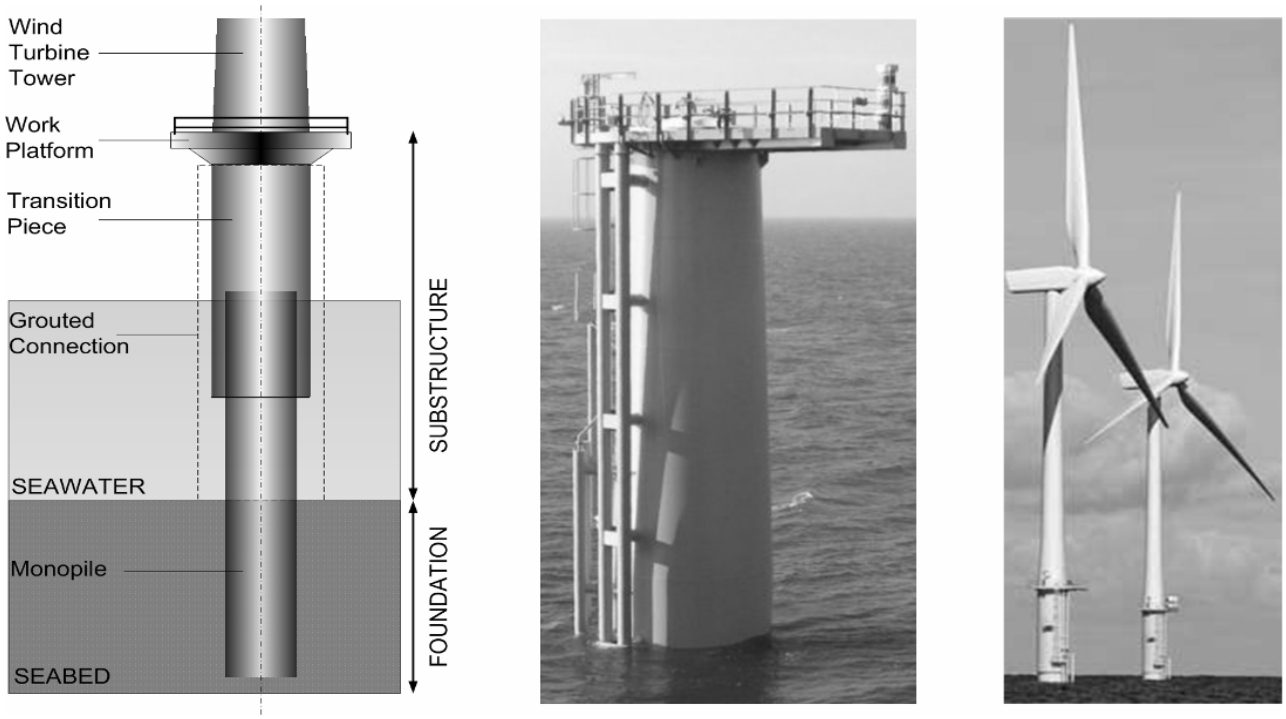

Figure 1-3: Grouted connection illustration and photos of installed arrangements.

The pre-fabricated transition piece in Figure 1-3 is usually embracing the pile, although the opposite is possible, but impractical for mounting external equipment such as ladder and cables. Additionally, the tolerances that occur during pile driving or drilling are accounted for during transition piece installation, which ensures adjustment of both horizontal and vertical inaccuracies. Adjustment of verticality is done by e.g. a pump connected to hydraulic adjustment cylinders mounted on the inside of the transition piece [Densit, 2009]. The grout is pumped through flexible hoses or by hand pumping into the annuli and trapped at the bottom of the transition piece by specially developed rubber seals, mounted on the inside of the transition piece.

The monopile foundation is divided into two regions. The substructure is the structure between the wind turbine tower and seabed, while the actual foundation is the remaining structure that penetrates the seabed, as shown in Figure 1-3. A technical representation of the substructure the monopile foundation in Figure 1-3 is shown in Figure 1-4.

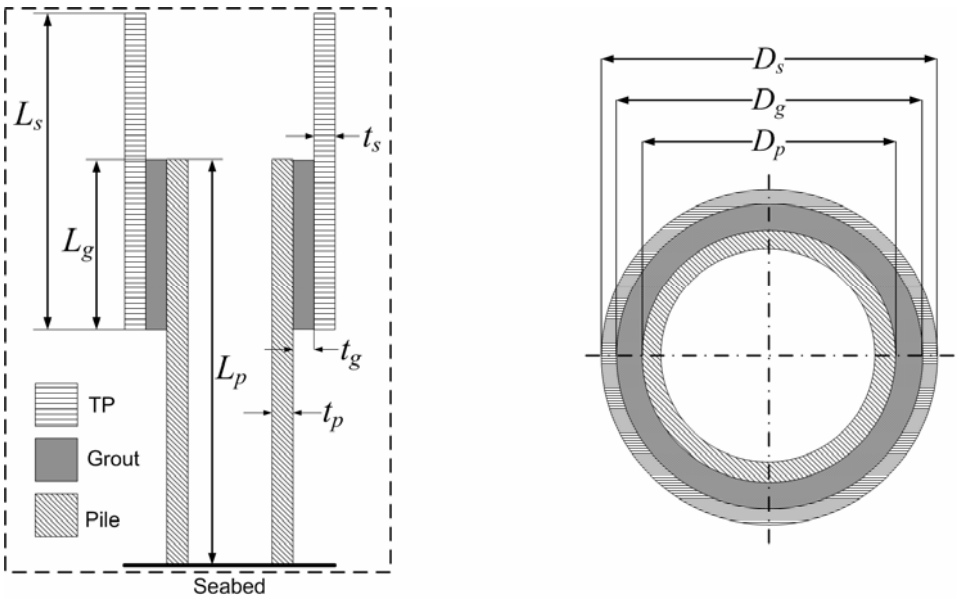

Figure 1-4: Technical representation of the grouted connection.

The illustration in Figure 1-4 represents the overall and idealized monopile foundation structure composed of a pile, transition piece and the grout that joins the two together. An overview of the most typical component sizes in the connection depicted in Figure 1-4 is outlined in Table 1-1.

Appropriate for water depths:	5 – 30 *m*
Outer pile diameter, D_p:	3 – 6 *m*
Length of the grouted connection, L_g:	1.3 – 1.6 × pile outside diameter, D_p
Thickness of the grout / annuli, t_g:	50 – 125 *mm*
Thicknesses of the pile and transition piece, t_p and t_s:	40 – 80 *mm*
Penetration into the soil:	20 – 40 *m*, depending on the soil

Table 1-1: Typical dimensions of grouted connections [Densit, 2009].

The size of a monopile foundation varies significantly, as seen in Table 1-1. As stated in section 1.2, it is the size of the turbine as well as the seabed characteristics that determines the overall size. As an example, a 2 MW wind turbine is usually mounted on a transition piece of $D_s \approx 5\ m$, with $t_g \approx 100\ mm$ and $L_g \approx 7\ m$ [Laundgaard A., 2009].

Advantages for the monopile foundations include minimal seabed preparation requirements, resistance to seabed movement, scour, and relatively inexpensive production costs due to the simplicity of the structure. The disadvantages include substructure flexibility at greater depths, expensive and time consuming installation due to time the grout needs to set, and decreased stiffness relative to other foundation types [Westgate et. al., 2005]. A flowchart of the mounting procedure is illustrated in Appendix 1. The grout materials typically used in the grouted connections as well as their basic properties are described in the next section.

1.3.1 Grout Properties

The basic information of some typical grout materials is given in this subsection, while more detailed information can be found in Appendix 2. The grout used for offshore casting can be characterized as a composite material, as its physical properties are highly dependent on the composition of the mixture, i.e. the water-cement ratio in the grout material as well as the size, amount and the properties of sand particles and the reinforcing steel fibres. The grouting process can be carried out above and below sea level using standard processing equipment.

Some of the most efficient grout materials on the market for offshore purposes are developed by Densit ApS, owned by Illinois Tool Works Inc. [Densit, 2009]. Their main products, known as S1, S5 and D4, underlie the internationally registered trademark Ducorit®, which are pumpable, ultra-high performance grouts specially developed for offshore use. The core of the Ducorit® products is a uniquely developed binder and they are characterized by:

- High strength and stiffness
- Low shrinkage
- High early-age strength
- High inner cohesion i.e. no mixing with seawater
- Good fatigue performance

In addition to the benefits outlined above, steel fibres are added to Ducorit® S5 and D4 which improves the tensile and bending strengths as the material shows significant ductility and high fracture energy, i.e. low formation of a new fracture surfaces [Andreasen, 2007]. The most common properties of the three materials are summarized in Table 1-2, with index g denoting the grout.

PROPERTY	Ducorit ® S1	Ducorit ® S5	Ducorit ® D4
Compressive strength, $f_C\left[MPa\right]$	110	130	210
Tension strength, $f_T\left[MPa\right]$	5	7	10
Modulus of elasticity, $E_G\left[GPa\right]$	35	55	70
Density, $\rho_G\left[kg/m^3\right]$	2250	2440	2740
Poisson's ratio, ν_G	0.19	0.19	0.19
Static coefficient of friction (Grout-Steel), μ_{GS}	0.6	0.6	0.6
The given values correspond to minimum 20 days of concrete curing at 20 °C, with 1.9 % by volume of steel fibres. Concrete curing is a process yielding accelerated early strength gain of concrete for more efficient use of cement, additives and space [Kraft, 2009].			

Table 1-2: Basic properties of the typical grout materials.

The properties given in Table 1-2 indicate that Ducorit® D4 is the strongest of the three materials with compressive strength up to 210 *MPa* and the elastic modulus of 70 *GPa* which are approximately two times the values for material S1, containing no reinforcement. It is well known and also seen in Table 1-2 that the brittle materials like the grout exhibit highly non-isotropic and nonlinear behavior. Consequently, analyzing grout must include a nonlinear constitutive model to relate the applied stresses or forces to strains or deformations. Such models are proposed by different plasticity based crack models to describe the behaviour of the grout [Chan et.al., 2005]. An example is the *Drucker-Prager* yield criterion, which is a pressure-dependent model for determining if material has failed or undergone plastic yielding, originally introduced to deal with plastic deformation in soils [Drucker & Prager, 1952].

Besides relying on the improved properties of the grout, several mechanical effects must be considered in grouted connections as well. Some of these are elaborated in the next subsection.

1.3.2 Main Effects in Grouted Connections

The limiting design condition in the monopile foundations is the overall deflection and vibration during loading. For this reason, typical monopiles with no lateral support are suitable for water depths up to 30 *m*, while supported monopiles are suitable for depths up to 40 *m*, and are better suited for inhomogeneous soils. Furthermore, monopile foundations should generally be avoided in deep soft soils due to the required length of the foundation pile [Westgate et. al., 2005].

During the grout casting process, no particular adhesion between the grout and steel surfaces can be achieved. The fixation of the pile and transition piece by means of grout is obtained by the static friction due to the surface roughness of the contact areas [Sørensen, 2009]. So far, the mathematical models are calibrated to experimental models with a transition piece of 1 *m* in diameter and grit blasted steel surface, from which a static coefficient of friction in the grout-steel interface of $\mu = 0.4$ to 0.6 has been obtained [Laund-

gaard, 2009]. These scaled models correspond to a connection 5 times smaller than a typical one used for a 2 *MW* wind turbine, as exemplified in section 1.3. The experimental correction- and friction coefficients in design formulas based on these scaled models are possibly out of range when dealing with a full scale structure. This could be inspected by full scale models, but has not been preformed so far due to high expenses and practical issues. Nevertheless, the scaled models are probably well suited in order to draw conclusions about the overall behaviour of the connection subjected to different loadings. However, these results should not be directly transferred to full scale models but treated very precautiously, due to the rough effects discussed previously.

Furthermore, possible irregularities in the walls of the two steel pipes constitute some of the rough imperfections, which combined with the fine grain size of the grout, contribute to the frictional effects [Sørensen, 2009]. This is also confirmed according to [Jensen, 2009], stating that the micro-properties in the grout-steel interface for full scale structures are much less important than the macro-inaccuracies in the pipe walls, since these act as shear-locks in the connection. These inaccuracies are primarily buckles or dents in the walls, caused by e.g. material creep due to welding, production tolerances and transportation collisions. However, additional resistance to shearing in the connection has been proposed in form of mechanical *shear keys*, as illustrated in Figure 1-5b).

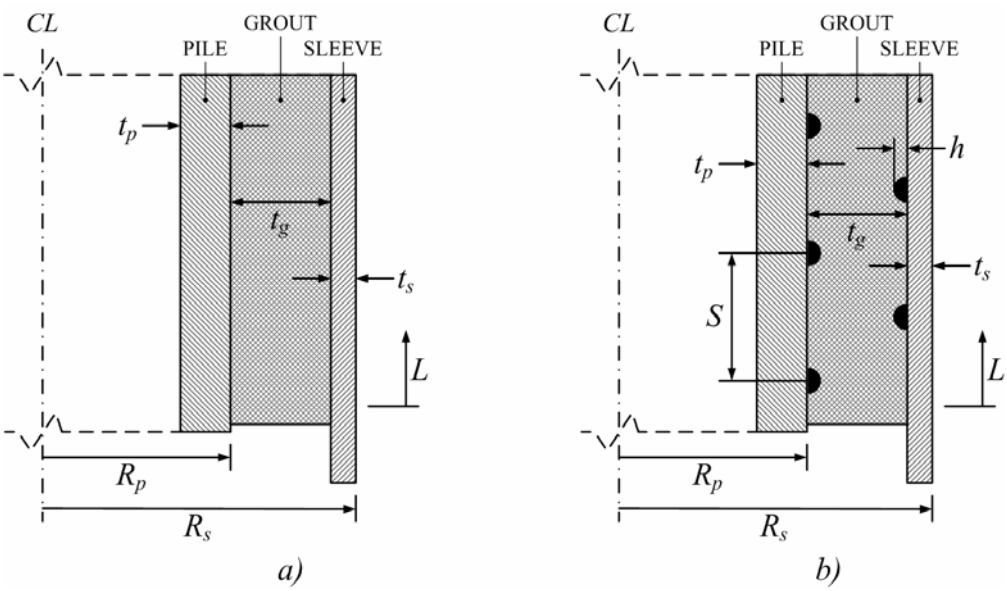

Figure 1-5: Connection with and without shear keys. Reprinted from [DNV-OS-J101, 2007, pp.89].

The shear keys in Figure 1-5b) are usually formed as steel rings and attached by means of welding. They are applied on the inner wall of the transition piece and the outer wall of the pile to obtain the shear resistance in the connection more efficiently. However, a major disadvantage in applying these is introduction of stress concentrations around the weld beads that become critical areas when considering lifetime estimation of the structure. Consequently, the dimensions, the positions and the amount of these should be well chosen as the

lifetime of the structure can be significantly reduced. With some of the mechanical effects in the connection described, the statutory demands by DNV are introduced in the following.

1.3.3 Design Criteria According to DNV

The standard [DNV-OS-J101, 2007] covers a set of state-of-the-art design rules required to be fulfilled in order to achieve a complete certification and approval of an offshore wind turbine structure. This includes wind turbine, substructure and foundation in Figure 1-3 and site-specific approval of wind turbine structure, comprising the three aforementioned parts. Some of the main technical tasks to be considered in the structural analysis, according to the standard, are outlined below.

Design criteria comprise:

- Environmental forces, operational forces, dead weight
- Structural materials and surface corrosion protection of metallic structural parts
- Fatigue analysis due to an operation period of usually 20-30 years
- Penetration length of the foundation pile as a function of its diameter and thickness (considering the impact force of the forging hammer and the shear reaction of the soil)
- Effects of the soil reaction to the loads transmitted by foundation piles

Site characteristics comprise:

- Seabed characteristics, such as stratigraphic description, bearing capacity of the soil, depth and slope of the sea bed
- Wind / sea actions such as wind speed and direction at specific height, height of the waves at the site, peak period, deep currents and scouring effects
- Effects produced by the wind turbine on the supporting structure comprising bending moments, shear forces, vertical and torsional forces

In addition to the technical tasks outlined above, the strength of a grouted connection may also depend on the following factors according to Clause A104 in [DNV-OS-J101, 2007]:

- Grout strength and modulus of elasticity
- Tubular and grout annulus geometries
- Application of mechanical shear keys
- Grouted length to pile diameter ratio, i.e. L_g / D_p
- Surface conditions of tubular surfaces in contact with grout
- Grout shrinkage or expansion
- Load history (mean stress level, stress ranges)

Consequently, a considerable number of tasks must be taken into account when analyzing monopile foundation structures involving grouted connections. Guidance notes for monopile foundation structures are given in Section 9 of [DNV-OS-J101, 2007], entitled Design and Construction of Grouted Connections. However, it is observed that one specific area has not been covered by the standard, which is elaborated in the following section, leading to the overall objective of the subsequent work in the remainder of this report.

1.4 Problem Presentation

The overall characterization of monopile foundations including the general tasks the designer should account for in grouted connections are presented in the previous section. These tasks are treated by means of general design rules, which according to Clause A201 in Section 9 of [DNV-OS-J101, 2007] involve axial loading combined with torque and bending moment combined with shear loading. A guidance note from Clause A201 is quoted below:

> *"Long experience with connections subjected to axial load in combination with torque exists, and parametric formulae have been established for design of connection subjected to this type of loading. For connections subjected to bending moment and shear force, no parametric design formulae have yet been established. Therefore, detailed investigations must be carried out for such connections."*

The guidance note also states that it may be conservative to assume that axial load and bending moment do not interact. If considering offshore oil/gas platforms founded by grouted connections, these predominantly expose the connections to axial loading. In addition, this makes use of mechanical shear keys quite evident to transfer the axial loads properly. However, the governing load from wind turbines is the overturning moment due to wind loading, which does not necessarily require use of shear keys in the connection. Consequently, splitting the loads and evaluating their effects in the connection separately may be conservative but also reasonable.

As stated by the former part of the quote, the parametric formulae for axial, i.e. vertical, and torsional load transfer are well known, which describe the stress state in the connection. However, these will not be presented here as they are fully described in the standard and the reference is given to Clause B in [DNV-OS-J101, 2007]. Nevertheless, it is rather the latter part of the quote that appears more conspicuous, stating that no parametric formulae have been established for horizontal load transfer. On account of this part, the problem statement is formulated in the following section.

1.5 Problem Statement

Based on the discussions made in problem presentation, the problem statement to be addressed in this report is:

To develop parametric formulae for the governing field equations concerning grouted connections in monopile wind turbine foundations subjected to horizontal load transfer.

The above problem statement is elaborated by the following sub-problems:

1. To analytically establish generalized parametric expressions for the field equations in the grout
2. To estimate the stress state and express the stiffness of a specific connection
3. To support and confirm the analytical results by means of a corresponding Finite Element Model

In order to address the sub-problems stated above, several initial simplifications and restrictions are made. These are elaborated in the following subsection.

1.5.1 Simplifications, Assumptions and Restrictions

The many technical tasks involved in constructing monopile foundation structures, as described in subsection 1.3.3, are much more sophisticated and complex in reality than exact mathematical models can describe. Consequently, simplified solution procedures and thereby approximated results must be accepted. Nowadays, many designers might state that the best way of modelling such real system is by discretizinig it into a Finite Element Model to obtain numerical results. However, large and complicated systems usually require large number of elements, which demands large computer capacities. Although the computer capacities have been increasing rapidly, there is still a long way to go if desiring to solve such large models in a matter of seconds or minutes and not hours or days. For this reason, even discretized models need additional simplifications in order to obtain numerical results within reasonable and affordable time span. The same is necessary for analytical models in order to obtain well-arranged and manageable results on limited number of pages. In general, simplifying a model basically corresponds to reducing the number of state variables and parameters of the real system. However, every simplification must be well posed and argued in order to preserve the uniqueness and essentiality of the system to be analyzed.

The present problem dealing with grouted connection in monopile foundation structures is generally described in section 1.3 with respect to the three main elements in the overall structure, i.e. the pile, transition piece and the grout. The following simplifications and assumptions for the three elements are presumed:

- All external equipment, such as work platform, cables and ladders, welded or bolted to the structure is disregarded, such that the structure is idealized as illustrated in Figure 1-4 and Figure 1-5a).

- The two pipes and the grout filling the annuli shall be taken as concentric and cylindrical geometries with no significant surface irregularities, i.e. smooth and homogeneous contact surfaces are assumed. Thus, the effect of shear-keys will not be treated.

- Contact effects, such as friction, are disregarded and the grout is initially taken as linear and isotropic continuous material.

The assumptions outlined above will be further discussed in Chapter 4. In addition to the simplifications outlined above, the following restrictions are presumed:

- In the analytical part of the work, the grout will be treated as linearly elastic material with the compressive strength, modulus of elasticity, Poisson's ratio and density taken for Ducorit® D4, as shown in Table 1-2.
- Only static, horizontal load acting at the turbine shall be accounted for. Here, the equivalent horizontal load at the top of transition piece, provided by ISC, will be used, see Appendix 3. Steel properties of the pile and transition piece are given in Appendix 3 as well. The remaining structure above the transition piece is omitted.

Additional assumptions and simplifications will be made throughout the report and discussed in the relevant context. However, the most essential ones have been presented and will be put to use in the analytical approach, carried out in the following chapter.

Chapter 2

2. Analytical Analysis of the Grouted Connection

The horizontal wind load at the wind turbine results in a certain load transfer and consequently distribution of stresses in the grouted connection. The field of science covering these kinds of problems is *continuum mechanics*, which addresses the behaviour of a continuous deformable material subjected to external loadings such as forces, moments, gravitational forces, displacements, velocities and thermal changes. This requires though, that the effects of the microstructure of the grout are disregarded and that it is in stead considered as a fully continuous media. As a continuum is composed of closely packed particles, the material density, force and displacement can be treated as continuous and differentiable functions [Schjødt, 2005]. Consequently, the governing field equations from theory of elasticity are differential equations, dealing with the infinitesimal differences in quantities between the neighbouring particles.

The objective of this chapter is to apply the governing field equations to the present problem of the grouted connection, governed by the simplifications and restrictions given in subsection 1.5.1. Some of the theories utilized in this chapter will be derived in detail, in order to clarify the subsequent procedures and simplify the henceforward referencing. The governing field equations and solution strategies in theory of elasticity, followed by a more comprehensive analysis of the present problem, are presented in the following section.

2.1 Governing Field Equations in Linear Elasticity

As restricted in section 1.5.1, the grout shall be taken as linear elastic, homogeneous and isotropic material, whereby the governing field equations for such materials are presented here. These relations will be expressed in index form, but written and elaborated explicitly when appropriate. They are expressed by means of the following quantities [Stegmann, 2003]:

- $\varepsilon_{ij} = \varepsilon_{ji}$ is Cauchy's strain tensor, linearized and infinitesimal
- u_i is the displacement vector
- $\sigma_{ij} = \sigma_{ji}$ is the Cauchy's stress tensor

- B_i are the body forces
- C_{ijkl} is the elasticity/stiffness tensor
- λ, μ and E, ν are the material constants, where $\lambda = \frac{\nu E}{(1+\nu)(1-2\nu)}$ and $\mu = \frac{E}{2(1+\nu)}$ are also known as Lamé's parameters for isotropic materials

The six infinitesimal strain-displacement relations in a deformed body can be expressed by Cauchy's strain tensor as:

$$\varepsilon_{ij} = \frac{1}{2}\left(u_{i,j} + u_{j,i}\right) \tag{2.1}$$

The three equations of equilibrium are expressed by balancing the internal stresses due to tractions acting on every point of the body surface to the body forces per unit volume acting on every point in the body volume, as:

$$\sigma_{ij,j} + B_i = 0 \tag{2.2}$$

The six constitutive relations between the strain and stress tensor for linear elastic materials are expressed by Hooke's generalized law as:

$$\sigma_{ij} = C_{ijkl}\varepsilon_{kl} \Leftrightarrow \sigma_{ij} = \lambda\varepsilon_{kk}\delta_{ij} + 2\mu\varepsilon_{ij} \Leftrightarrow \varepsilon_{ij} = \frac{1+\nu}{E}\sigma_{ij} - \frac{\nu}{E}\sigma_{kk}\delta_{ij} \tag{2.3}$$

Furthermore, compatibility equations can be expressed to ensure that the displacement of a body is taking place in a continuous and compatible matter and are generally applied when the strains in the problem are arbitrarily specified [Stegmann, 2003]. They are expressed as:

$$\varepsilon_{ij,km} + \varepsilon_{km,ij} - \varepsilon_{ik,jm} - \varepsilon_{jm,ik} = 0 \tag{2.4}$$

The system in (2.4) is a set of 81 relations between the six strain components, but can be reduced to six independent equations due to symmetry in the *ij* and *kl* indices and furthermore to three equations due to linear dependency between the six. A proof of this is demonstrated in e.g. [P7, 2007]. However, if a given problem formulation includes the displacements, the strain compatibility is generally satisfied and the compatibility relations can be omitted.

Consequently, the general system of field equations in linear elasticity is composed of the six strain-displacement relations in (2.1), the three equilibrium equations in (2.2) and the six constitutive relations in (2.3). These are solved by the three displacement components u_i, the six strains components ε_{ij} and the six stress components σ_{ij}. Hence, there are 15 independent equations with 15 unknowns, which make up a consistent and determinate system of equations for an isotropic homogeneous media. The entire system is summarized in Figure 2-1, with $T_i^{(\nu)}$ denoting the surface tractions and B.C. the boundary conditions.

$$\boxed{External\ loads: T_i^{(v)}, B_i}$$

$$\Downarrow Equations\ of\ equilibrium\ (3\ equations)$$

$$\boxed{Stresses: \sigma_{ij}}\ (6\ unknowns) \Leftarrow \textbf{B.C. = Prescribed surface tractions}$$

$$\Downarrow Hooke's\ generalised\ law\ (6\ equations)$$

$$\boxed{Strains: \varepsilon_{ij}}\ (6\ unknowns)$$

$$\Downarrow Lagrange's\ strain\ tensor\ (6\ equations)$$

$$\boxed{Displacements: u_i}\ (3\ unknowns) \Leftarrow \textbf{B.C. = Prescribed displacements}$$

Figure 2-1: Governing field equations for a linear elastic continuum.

The schematic overview in Figure 2-1 comprises a system of differential relations among the three quantities resulting from external loads. These express the particular behaviour at every point within the elastic continuum being examined. The figure also shows that this general formulation is completed by introducing appropriate boundary conditions, which specify the physical behaviour of the body at one or more boundaries. Specifying these provides the necessary loading inputs used to solve a specific problem described by the system in Figure 2-1, also known as a boundary value problem [Shames & Dym, 2003]. A brief classification of fundamental boundary value problems is conducted in the following section.

2.2 Classification of Boundary Value Problems

As shown in the previous section, a boundary value problem for an isotropic-homogeneous media is a system of 15 independent differential equations and equal number of unknowns. A solution to this problem corresponds to the solution of the differential equations which simultaneously satisfies the boundary conditions. In order to complete and solve the system of field equations, three fundamental boundary value problems have been defined. These are classified below with reference to [Shames & Dym, 2003] and [Schjødt, 2005].

1. The boundary value problem of the 1st kind is characterized as the determination of the stress and displacement distribution in a body under a given body force distribution and prescribed *surface tractions* over the boundary. This is also known as a *Dirichlet* boundary condition, named after the German mathematician Johann Peter Gustav Lejeune Dirichlet (1805-1859).

2. The boundary value problem of the 2nd kind is characterized as the determination of stress and displacement distribution in a body under a given body force distribution and prescribed *displacement distribution* over the entire boundary. This is also known as a *Neumann* boundary condition, named after Carl Neumann (1832-1925), who was also a German mathematician.

3. The third boundary value problem involves *mixed boundary conditions*, corresponding to imposing both the Dirichlet and Neumann boundary conditions**.** For a partial differential equation, this kind of problem indicates that different boundary conditions are used on different parts of the boundary. These are also known as *Cauchy* boundary conditions, named after the French mathematician Augustin Louis Cauchy (1789-1857).

The general idea for the three kinds of boundary conditions is illustrated in Figure 2-2, with different boundaries specified on the body ***R*** with the surface ***S***.

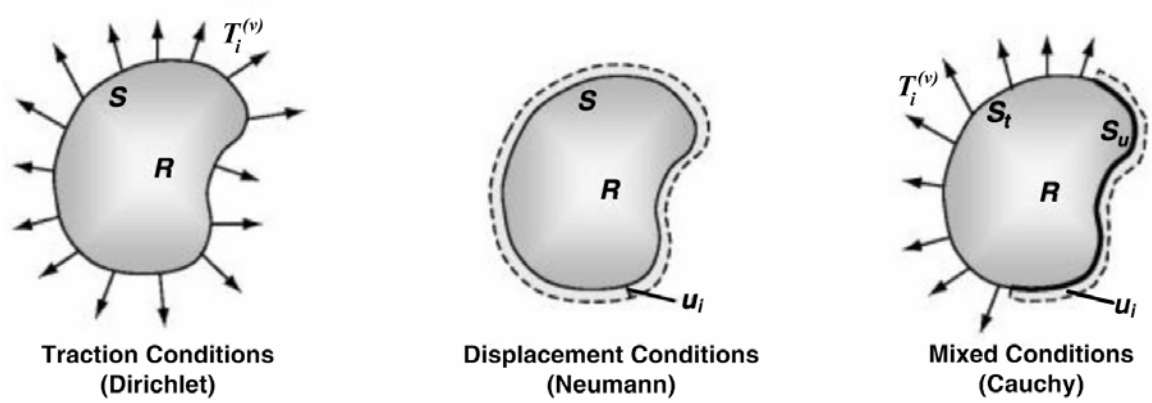

Figure 2-2: Illustration of Dirichlet, Neumann and Cauchy boundary conditions.

The Dirichlet and the Neumann conditions in Figure 2-2 are given over the entire body surface ***S***, while the Cauchy conditions are represented by tractions $T_i^{(v)}$ specified on the boundary $\boldsymbol{S_t}$ and displacements u_i on the remaining portion $\boldsymbol{S_u}$, thus giving the total boundary by $\boldsymbol{S} = \boldsymbol{S_t} + \boldsymbol{S_u}$ [Sadd, 2004]. Cauchy boundary conditions can be exemplified by the theory of 2nd order ordinary differential equations (ODE's), where to have a particular solution, e.g. $y(x)$, the value of the function and the value of the derivative at a given initial or boundary point, e.g. $x = a$, must be specified. For α, β being the values of the function and its derivative, respectively, this is written as $y(a) = \alpha$ and $y'(a) = \beta$. Consequently, these two types of boundary values specify how the body is supported and loaded. Most real systems are in fact governed by these mixed Cauchy conditions.

Depending on the geometric and loading complexity, the outlined boundary value problems are often difficult to solve. However, several different solution strategies for such problems have been generalized and two of them are briefly reviewed in the following section.

2.3 General Solution Principles

The system in Figure 2-1 with the number of equations matching the number of unknowns has a prepossessing appearance. However, solving this system for any of the three boundary value problems by analytical methods is not as straightforward. Nevertheless, depending on the prescribed boundary conditions, the sys-

tem can be simplified by reducing the number of unknowns. For the boundary value problem implying Dirichlet conditions, i.e. traction boundary conditions only, it appears convenient to relate the field equations solely in terms of stresses. Similarly, as the boundary value problem dealing with Neumann conditions, i.e. displacement boundary conditions, relations in terms of displacements can be posed. Consequently, a *stress formulation* for the 1st kind and a *displacement formulation* for the 2nd kind of boundary value problems can be developed to explicitly determine the reduced system of field equations [Sadd, 2004].

Since the displacement boundary conditions are prescribed in the present problem, it is convenient to present the displacement formulation. Therefore, no detailed elaboration of the stress formulation will be presented here and the reference is given to e.g. [Sadd, 2004]. In brief, the stress formulation is conducted by eliminating the displacements and strains in the field equations in Figure 2-1 and including the compatibility equations in stead. Hooke's law in (2.3) is then applied to express these equations in terms of stresses, followed by incorporation of the equilibrium equations given in (2.2). This results in compatibility equations in terms of stresses, also known as *Beltrami-Michell compatibility equations* [Sadd, 2004], which describe the deformation of an elastic continuum, solely subjected to surface tractions on the boundary. There are originally six of these, be can be reduced into three, as shown in e.g. [Borodachev, 1995]. In index form, the Beltrami-Mitchell equations are written as

$$\sigma_{ij,kk} + \frac{1}{1+\nu}\sigma_{kk,ij} = -\frac{\nu}{1-\nu}\delta_{ij}B_{k,k} - B_{i,j} - B_{j,i}$$

Analytical solution to this system can be obtained by use of stress functions, such as those proposed by G.B. Airy (1801-1892) for a 2D case, see [P7, 2007, pp. 60-61]. Prior to a detailed elaboration of the displacement formulation, a general overview of the stress and displacement formulations is illustrated in Figure 2-3.

General System of Field Equations

15 Equations:	*15 Unknowns:*
$e_{ij} = \frac{1}{2}\left(u_{i,j} + u_{j,i}\right)$	u_i
$\sigma_{ij,j} + B_i = 0$	σ_{ij}
$\sigma_{ij} = \lambda e_{kk}\delta_{ij} + 2\mu e_{ij}$	e_{ij}

↙ ↘

Stress Formulation	**Displacement Formulation**
6 Equations:	*3 Equations:*
$\sigma_{ij,j} + B_i = 0$	$(\lambda+\mu)u_{k,ki} + \mu u_{i,kk} + B_i = 0$
$\sigma_{ij,kk} + \frac{1}{1+\nu}\sigma_{kk,ij} = -\frac{\nu}{1-\nu}\delta_{ij}B_{k,k} - B_{i,j} - B_{j,i}$	*3 Unknowns:*
6 Unknowns:	u_i
σ_{ij}	

Figure 2-3: The governing and the reduced systems of field equations [Sadd M.H, 2004].

The flowchart summarised in Figure 2-3 comprise the two main solution principles for the general field equations in theory of elasticity. It can be seen that the stress formulation involves six equations with six unknowns, i.e. three equilibrium and three independent Beltrami-Mitchell compatibility equations, while the displacement formulation involves three only. However, this does not necessarily imply that the solution effort is halved as well. Nonetheless, many mathematical techniques can be applied in order to solve these reduced elasticity field equations. Some involve the development of exact analytical solutions, while others deal with construction of approximate solutions. Another procedure involves the establishment of numerical solution methods, such as FEM carried out in Chapter 3. The next subsection encloses a detailed analytical development of the displacement formulation shown in Figure 2-3, followed by a solution procedure of the present problem.

2.4 The Displacement Formulation

The reduced set of field equations solely in terms of displacements can be obtained both for elastostatics and elastodynamics. Although the objective of this report is primarily to account for static effects in the connection, it is convenient to perform static analyses with respect to both time and space. Thus, a quas-istatic loading is considered, which by definition occurs infinitely slowly. This is supported by the fact that time always increases monotonically, and most things in nature happen over a period of time, however brief the period may be [Ansys, 2009]. For this reason, the displacement formulation for elastodynamics will be presented in the following. The advantage of this choice will be discussed later in this text.

To derive the displacement formulation in elastodynamics, it is essential to introduce Newton's second law. According to this law, the rate of change of the momentum of a particle is proportional to the resultant force acting on the particle and is in the direction of that force. In the case of a body of constant mass dm, Newton's 2nd law states that

$$dF_i = (dm)a_i \tag{2.5}$$

In equation (2.5) F_i is the resultant force acting on the body and a_i is the acceleration which can be expressed in terms of the velocity vector as

$$a_i = \frac{Dv_i}{Dt} = \left(\frac{\partial v_i}{\partial x}\frac{dx}{dt} + \frac{\partial v_i}{\partial y}\frac{dy}{dt} + \frac{\partial v_i}{\partial z}\frac{dz}{dt} \right) + \frac{\partial v_i}{\partial t} \tag{2.6}$$

In expression (2.6) D/Dt is the material derivative along a certain path moving with velocity v_i. The rightmost expression indicates that the time derivative d/dt is obtained both as a function of space, combined with the motion of the body, and time. For small body movements, the product terms in the brackets can be neglected as these are minute compared to the time derivative. Hence, the material derivative becomes approximately equal the time derivative, i.e. $D/Dt \approx d/dt$. Hereby, Newton's 2nd law can be written as

$$dF_i = (dm)\frac{dv_i}{dt} \tag{2.7}$$

Noticing that the forces dF_i are the sum of all forces acting on the body, Newton's 2nd law can be expressed in terms of body forces B_i, acting on the volume V and the surface tractions T_i^v acting on the surface S by integration over the entire volume and surface as given in (2.8).

$$dF_i = (dm)\frac{dv_i}{dt} \Rightarrow \int_S T_i^v dS + \int_V B_i dV = \int_V \rho \frac{dv_i}{dt} dV \tag{2.8}$$

Applying Cauchy's relationship between the traction vector and the stress tensor and the Gauss's divergence theorem that converts the surface integral over the surface S into the volume integral over the volume V [Stegmann, 2003], equation (2.8) can be expressed as

$$\int_V \sigma_{ij,j} dV + \int_V B_i dV = \int_V \rho \frac{dv_i}{dt} dV \Leftrightarrow \int_V \left(\sigma_{ij,j} + B_i\right) dV = \int_V \rho \frac{dv_i}{dt} dV \tag{2.9}$$

It is noted that the density ρ of the body material is assumed nonzero and constant such that its time derivative is zero and thus omitted in equation (2.9). Furthermore, for an arbitrary body contained in a constant volume V, this equation is satisfied simply by omitting the integration, i.e. setting the integrand to zero. Consequently, this leads to *equations of motion* expressed by Cauchy's relation given as [Aster R., 2008]

$$\sigma_{ij,j} + B_i = \rho \frac{dv_i}{dt} \tag{2.10}$$

The equations of motion in (2.10) are valid for any continuum, as they satisfy Newton's 2nd law, describing the behaviour of a continuum as a function of space and time. In other terms, the acceleration of an element within the continuum results from the application of surface and body forces. Assuming that the continuum is free of body forces and by writing the inertial term as the product of the density ρ and the second derivative of the displacement vector $u_i(x,y,z,t)$, equation (2.10) becomes

$$\sigma_{ij,j}(x,y,z,t) = \rho \frac{\partial^2 u_i(x,y,z,t)}{\partial t^2} \Leftrightarrow \sigma_{ij,j}(x,y,z,t) - \rho \frac{\partial^2 u_i(x,y,z,t)}{\partial t^2} = 0 \tag{2.11}$$

The next step is to show that equations (2.11) can be written solely in terms of displacements. This is possible as the stresses are related to the strains, which are formed from the first derivatives of the displacement components, as demonstrated in Figure 2-1. This implies that the equations of motion do not depend on the elastic constants, while their solutions do. Furthermore, it can be seen that the equations of motion in the form given in (2.11) relate the spatial derivatives of the stress tensor to the time derivative of the displacement vector. Consequently, the resulting solutions of these equations express the displacement vector, the stress and strain tensors as functions of both space and time. Keeping this in mind, the most of the hencefor-

ward notation will exclude these dependencies for convenience and the denotations will be u, σ_{ij} and ε_{ij}, respectively. Thus, expressing equation (2.11) explicitly for the three Cartesian coordinate axes gives:

$$\begin{aligned} x-direction: &\quad \frac{\partial \sigma_{xx}}{\partial x}+\frac{\partial \sigma_{xy}}{\partial y}+\frac{\partial \sigma_{xz}}{\partial z}-\rho\frac{\partial^2 u_x}{\partial t^2}=0 \\ y-direction: &\quad \frac{\partial \sigma_{yx}}{\partial x}+\frac{\partial \sigma_{yy}}{\partial y}+\frac{\partial \sigma_{yz}}{\partial z}-\rho\frac{\partial^2 u_y}{\partial t^2}=0 \\ z-direction: &\quad \frac{\partial \sigma_{zx}}{\partial x}+\frac{\partial \sigma_{zy}}{\partial y}+\frac{\partial \sigma_{zz}}{\partial z}-\rho\frac{\partial^2 u_z}{\partial t^2}=0 \end{aligned} \tag{2.12}$$

As discussed, the stresses in (2.12) can be expressed in terms of displacements, since these are related by the strains. This is elaborated in the following, by first introducing some basic, but important, properties of the strain tensor. The strain tensor in terms of the displacement components is given as [Stegmann, 2003]

$$\varepsilon_{ij}=\frac{1}{2}\left(\frac{\partial u_i}{\partial x_j}+\frac{\partial u_j}{\partial x_i}\right)=\begin{pmatrix} \frac{\partial u_x}{\partial x} & \frac{1}{2}\left(\frac{\partial u_x}{\partial y}+\frac{\partial u_y}{\partial x}\right) & \frac{1}{2}\left(\frac{\partial u_x}{\partial z}+\frac{\partial u_z}{\partial x}\right) \\ \frac{1}{2}\left(\frac{\partial u_y}{\partial x}+\frac{\partial u_x}{\partial y}\right) & \frac{\partial u_y}{\partial y} & \frac{1}{2}\left(\frac{\partial u_y}{\partial z}+\frac{\partial u_z}{\partial y}\right) \\ \frac{1}{2}\left(\frac{\partial u_z}{\partial x}+\frac{\partial u_x}{\partial z}\right) & \frac{1}{2}\left(\frac{\partial u_z}{\partial y}+\frac{\partial u_y}{\partial z}\right) & \frac{\partial u_z}{\partial z} \end{pmatrix} \tag{2.13}$$

The strain tensor in (2.13) is diagonal as the basis vectors of the coordinate system are collinear with the principal strain axes. Consequently, the sum of the diagonal terms in the strain tensor is written as

$$\varepsilon_{ii}=u_{i,i}=\frac{\partial u_x}{\partial x}+\frac{\partial u_y}{\partial y}+\frac{\partial u_z}{\partial z}=\nabla\cdot\vec{u} \tag{2.14}$$

The summation in (2.14) is the divergence of the three dimensional displacement field $\vec{u}$. In general, the divergence of an arbitrary vector field at a given point (x, y, z) is just a signed scalar that represents the magnitude of the displacement at that point in the three directions, also known as the cubic dilatation. This is depicted in Figure 2-4 showing the change in volume of a small cube due to the principal strains.

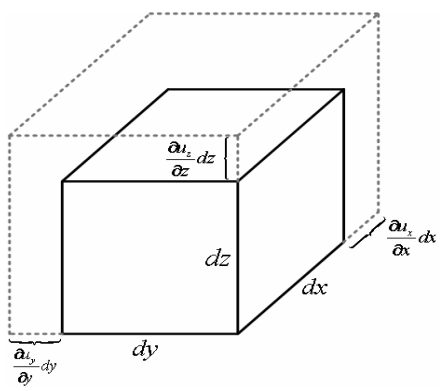

Figure 2-4: The dilatation is the fractional expansion in volume, i.e. the sum of the principal strains.

Additionally, the displacement field contains information of the direction in which each particle in the field rotates, as well as the speed at which they rotate. This information is extracted by applying the *curl*, i.e. rotation operation of the displacement field. Curl is a vector operator that describes the rotation of the field and is represented by a vector that points along the axis of the rotation, whose length corresponds to the speed of the rotation. The curl of a displacement field $\vec{u}$ is written as the determinant

$$\nabla \times \vec{u} = \begin{vmatrix} \vec{i} & \vec{j} & \vec{k} \\ \frac{\partial}{\partial x} & \frac{\partial}{\partial y} & \frac{\partial}{\partial z} \\ u_x & u_y & u_z \end{vmatrix} = \left(\frac{\partial u_z}{\partial y} - \frac{\partial u_y}{\partial z} \right) \vec{i} + \left(\frac{\partial u_x}{\partial z} - \frac{\partial u_z}{\partial x} \right) \vec{j} + \left(\frac{\partial u_y}{\partial x} - \frac{\partial u_x}{\partial y} \right) \vec{k}$$

Hence, the curl is a vector while the divergence is a scalar, both of which are important operators in this chapter. Another useful operator is the *Laplacian* defined as the divergence of the gradient, see Appendix 4, i.e. $\nabla \cdot \nabla$, and is given for a displacement field $\vec{u}$ as

$$\nabla \cdot \nabla \vec{u} = \nabla^2 \vec{u} = \Delta \vec{u} = \frac{\partial^2 \vec{u}}{\partial x^2} + \frac{\partial^2 \vec{u}}{\partial y^2} + \frac{\partial^2 \vec{u}}{\partial z^2} \tag{2.15}$$

Hence, the Laplacian is the second order partial differential operator and its importance will be discussed later in this chapter.

Returning to the stresses, since these are related to the strains by the constitutive relation in terms of Lamé constants defined in section 2.1, the expressions in (2.12) can be written in a single equation as [Stegmann, 2003]

$$\sigma_{ij} = \lambda \varepsilon_{kk} \delta_{ij} + 2\mu \varepsilon_{ij} \tag{2.16}$$

The summation of principal strains, i.e. the divergence in (2.14), can be substituted in equation (2.16) to finally obtain

$$\sigma_{ij} = \lambda \left(\nabla \cdot \vec{u} \right) \delta_{ij} + 2\mu \varepsilon_{ij} \tag{2.17}$$

which are the stress-strain equations for an isotropic inhomogeneous continuum. Next, substituting expression (2.13) in (2.17), the three stresses used in the *x*-directional equation of motion in (2.12) are written as

$$\begin{aligned} \sigma_{xx} &= \lambda \nabla \cdot \vec{u} \delta_{xx} + 2\mu \varepsilon_{xx} = \lambda \nabla \cdot \vec{u} + 2\mu \frac{\partial u_x}{\partial x} \\ \sigma_{xy} &= \lambda \nabla \cdot \vec{u} \delta_{xy} + 2\mu \varepsilon_{xx} = 2\mu \varepsilon_{xy} = \mu \left(\frac{\partial u_x}{\partial y} + \frac{\partial u_y}{\partial x} \right) \\ \sigma_{xz} &= \lambda \nabla \cdot \vec{u} \delta_{xz} + 2\mu \varepsilon_{xz} = 2\mu \varepsilon_{xz} = \mu \left(\frac{\partial u_x}{\partial z} + \frac{\partial u_z}{\partial x} \right) \end{aligned} \tag{2.18}$$

Recalling that the elastic constants for an isotropic material are invariant, i.e. do not vary with position, the spatial derivatives of the stress components in (2.18) are easily obtained as given in (2.19).

$$\begin{aligned}
\frac{\partial \sigma_{xx}}{\partial x} &= \lambda \frac{\partial \nabla \cdot \vec{u}}{\partial x} + 2\mu \frac{\partial^2 u_x}{\partial x^2} \\
\frac{\partial \sigma_{xy}}{\partial y} &= \mu \left(\frac{\partial^2 u_x}{\partial y^2} + \frac{\partial^2 u_y}{\partial y \partial x} \right) \\
\frac{\partial \sigma_{xz}}{\partial z} &= \mu \left(\frac{\partial^2 u_x}{\partial z^2} + \frac{\partial^2 u_Z}{\partial z \partial x} \right)
\end{aligned} \tag{2.19}$$

The derivatives in (2.19) can now be substituted into e.g. the *x*-directional equation of motion in (2.12) yielding

$$\begin{aligned}
&\frac{\partial \sigma_{xx}}{\partial x} + \frac{\partial \sigma_{xy}}{\partial y} + \frac{\partial \sigma_{xz}}{\partial z} - \rho \frac{\partial^2 u_x}{\partial t^2} = 0 \Leftrightarrow \\
&\lambda \frac{\partial}{\partial x} \left(\frac{\partial u_x}{\partial x} + \frac{\partial u_y}{\partial y} + \frac{\partial u_z}{\partial z} \right) + 2\mu \frac{\partial^2 u_x}{\partial x^2} + \mu \left(\frac{\partial^2 u_x}{\partial y^2} + \frac{\partial^2 u_y}{\partial y \partial x} \right) + \mu \left(\frac{\partial^2 u_x}{\partial z^2} + \frac{\partial^2 u_z}{\partial z \partial x} \right) - \rho \frac{\partial^2 u_x}{\partial t^2} = 0
\end{aligned} \tag{2.20}$$

The obtained is found to be a lengthy expression. However, as the displacement component u_x appears in every term of equation (2.20), it is convenient to apply the definition of the Laplacian in (2.15) giving

$$\Delta u_x = \frac{\partial^2 u_x}{\partial x^2} + \frac{\partial^2 u_x}{\partial y^2} + \frac{\partial^2 u_x}{\partial z^2} \tag{2.21}$$

Likewise, it is convenient to substitute the divergence of the displacement field given in (2.14), to finally reduce the equation of motion for the *x*-directional displacement component in (2.20) to

$$\begin{aligned}
&\lambda \underbrace{\left(\frac{\partial^2 u_x}{\partial x^2} + \frac{\partial^2 u_y}{\partial y \partial x} + \frac{\partial^2 u_z}{\partial z \partial x} \right)}_{\frac{\partial \nabla \cdot \vec{u}}{\partial x}} + \mu \underbrace{\left(\frac{\partial^2 u_x}{\partial x^2} + \frac{\partial^2 u_y}{\partial y \partial x} + \frac{\partial^2 u_Z}{\partial z \partial x} \right)}_{\frac{\partial \nabla \cdot \vec{u}}{\partial x}} + \mu \underbrace{\left(\frac{\partial^2 u_x}{\partial x^2} + \frac{\partial^2 u_x}{\partial y^2} + \frac{\partial^2 u_x}{\partial z^2} \right)}_{\Delta u_x} - \rho \frac{\partial^2 u_x}{\partial t^2} = 0 \Leftrightarrow \\
&(\lambda + \mu) \frac{\partial \nabla \cdot \vec{u}}{\partial x} + \mu \Delta u_x - \rho \frac{\partial^2 u_x}{\partial t^2} = 0
\end{aligned} \tag{2.22}$$

The equations of motion for the remaining displacement components are determined similarly and the complete set of equations of motion for the three coordinate directions can be combined by means of the vector Laplacian, see Appendix 4, for the displacement field given as

$$\Delta \vec{u} = \left(\Delta u_x,\ \Delta u_y,\ \Delta u_z \right)$$

Consequently the general expression for the equations of motion can be expressed as a single vector equation as given below

$$(\lambda+\mu)\nabla\left(\nabla\cdot\vec{u}\right)+\mu\Delta\vec{u}-\rho\frac{\partial^2\vec{u}}{\partial t^2}=0 \tag{2.23}$$

The expression in (2.23) comprises the equations of motion for an isotropic and elastic continuum expressed entirely in terms of the displacements, remembering that these are chosen as both space and time dependent. This corresponds to the reduced system of field equations presented in index form in Figure 2-3, free of body forces B_i but with dynamic source in stead, i.e.:

$(\lambda+\mu)u_{j,ji}+\mu u_{i,jj}+B_i=0$ in Figure 2-3 becomes $(\lambda+\mu)u_{j,ji}+\mu u_{i,jj}=\rho u_{i,tt}$ ((2.23) in index form)

Consequently, the displacement formulation of the field equations in terms of the three displacement components only has been derived. However, further rewriting of this linear system of partial differential equations can be done by using the vector identity for the Laplacian, see Appendix 4, stating that

$$\Delta\vec{u}=\nabla(\nabla\cdot\vec{u})-\nabla\times(\nabla\times\vec{u}) \tag{2.24}$$

such that equation (2.23) can be rewritten as

$$\begin{aligned}&(\lambda+\mu)\nabla(\nabla\cdot\vec{u})+\mu\left(\nabla(\nabla\cdot\vec{u})-\nabla\times(\nabla\times\vec{u})\right)-\rho\frac{\partial^2\vec{u}}{\partial t^2}=0\Leftrightarrow\\&(\lambda+2\mu)\nabla(\nabla\cdot\vec{u})-\mu\nabla\times(\nabla\times\vec{u})-\rho\frac{\partial^2\vec{u}}{\partial t^2}=0\end{aligned} \tag{2.25}$$

Solving the system of PDE's in (2.25) by finding an expression for the displacement field $\vec{u}$ allows for obtaining the remaining field equations in a given continuum free of body forces. However, this system is obviously coupled, as its solutions and their derivatives must satisfy more than one field equation, i.e. solving one of them depends on the solution to another. This introduces an additional difficulty that must be accounted for in the solutions of the system. Several mathematical techniques have been developed to simplify the system, which allows employment of several analytical solution methods. An overview of such techniques is given in e.g. [Sadd, 2004]. For the specific problem treated in this report, it is chosen to employ one of the analytical methods based on potential functions, which is elaborated in the following subsection.

2.4.1 Solution Method by Displacement Potentials

The objective of this section is to simplify the system in (2.25) by obtaining uncoupled governing equations in terms of the displacement potentials. One approach can be carried out by expressing the displacement field by utilizing *Helmholtz's* theorem, after the German mathematician *Hermann Ludwig Ferdinand von Helmholtz* (1821-1894).

His theorem is also known as the fundamental theorem of vector calculus and states that any sufficiently smooth and continuous vector field can be resolved into the sum of an irrotational, i.e. curl-free, and a solenoidal, i.e. divergence-free, vector field [Sadd, 2004]. This implies that any such vector field is expressed as a sum of two potentials known as *Lamé* potentials, after the French physicist and mathematician Gabriel Lamé (1795-1870). The two are the scalar potential φ associated with the dilatational part and the vector potential $\vec{\psi}$ associated with the rotational part of the displacement field. Thus, this theory suggests that if we know the divergence and the curl of a vector field, then we know everything there is to know about the field [Fitzpatrick, 2006]. Consequently, the displacement field can be written as a sum of the two fields, i.e. the gradient of a scalar field and the curl of a vector field, as

$$\vec{u} = \text{grad}\ \varphi + \text{rot}\ \vec{\psi} = \nabla\varphi + \nabla\times\vec{\psi} \tag{2.26}$$

The expression in (2.26) is referred to as *Helmholtz* decomposition. In general, when dealing with 3D problems, the vector potential is composed of three functions, i.e. one for each coordinate. Hence, the displacement field in (2.26) is composed of four unknown potentials to be obtained;

$$\varphi(x,y,z,t)\ ;\ \psi_x(x,y,z,t)\ ;\ \psi_y(x,y,z,t)\ ;\ \psi_z(x,y,z,t) \tag{2.27}$$

Hence, the potential representation specifies the three displacement components in terms of four potential components. In terms of these four potentials, equation (2.26) is explicitly and in vector form expressed as given in (2.28).

$$\vec{u} = \nabla\varphi + \nabla\times\vec{\psi} \Leftrightarrow \begin{Bmatrix} u_x \\ u_y \\ u_z \end{Bmatrix} = \begin{Bmatrix} \dfrac{\partial\varphi}{\partial x} \\ \dfrac{\partial\varphi}{\partial y} \\ \dfrac{\partial\varphi}{\partial z} \end{Bmatrix} + \begin{Bmatrix} \dfrac{\partial\psi_z}{\partial y} - \dfrac{\partial\psi_y}{\partial z} \\ \dfrac{\partial\psi_x}{\partial z} - \dfrac{\partial\psi_z}{\partial x} \\ \dfrac{\partial\psi_y}{\partial x} - \dfrac{\partial\psi_x}{\partial y} \end{Bmatrix} = \begin{Bmatrix} \dfrac{\partial\varphi}{\partial x} + \dfrac{\partial\psi_z}{\partial y} - \dfrac{\partial\psi_y}{\partial z} \\ \dfrac{\partial\varphi}{\partial y} + \dfrac{\partial\psi_x}{\partial z} - \dfrac{\partial\psi_z}{\partial x} \\ \dfrac{\partial\varphi}{\partial z} + \dfrac{\partial\psi_y}{\partial x} - \dfrac{\partial\psi_x}{\partial y} \end{Bmatrix} \tag{2.28}$$

The Helmholtz decomposition in (2.26) separates the displacement field into two parts. The gradient term in is defined as irrotational such that it has zero curl, and is written as

$$\nabla\times(\nabla\varphi) = 0 \tag{2.29}$$

which applies for any scalar field, φ. The vector part is solenoidal such that it has zero divergence, and is written as

$$\nabla\cdot\left(\nabla\times\vec{\psi}\right) = 0 \tag{2.30}$$

The solenoidal part in (2.30) is valid for any vector field, $\vec{\psi}$. By substituting the displacement vector expressed by (2.26) into system of equations in (2.25), the following is obtained

$$
\begin{aligned}
&(\lambda+2\mu)\nabla(\nabla\cdot\vec{u})-\mu\nabla\times(\nabla\times\vec{u})-\rho\frac{\partial^2\vec{u}}{\partial t^2}=0\Rightarrow\\
&(\lambda+2\mu)\nabla\left(\nabla\cdot\left(\nabla\varphi+\nabla\times\vec{\psi}\right)\right)-\mu\nabla\times\left(\nabla\times\left(\nabla\varphi+\nabla\times\vec{\psi}\right)\right)-\rho\frac{\partial^2\left(\nabla\varphi+\nabla\times\vec{\psi}\right)}{\partial t^2}=0
\end{aligned}
\tag{2.31}
$$

Noting that both the divergence of a curl operation and the curl of a gradient are per definition identical zero, see (2.30) and (2.29), as well as that the divergence of a gradient equals the Laplacian, i.e. $\nabla\cdot\left(\nabla\vec{u}\right)=\Delta\vec{u}$, see Appendix 4, the expression in (2.31) is reduced to

$$
(\lambda+2\mu)\nabla\left(\Delta\varphi\right)-\mu\nabla\times\left(\nabla\times\nabla\times\vec{\psi}\right)-\rho\frac{\partial^2\left(\nabla\varphi+\nabla\times\vec{\psi}\right)}{\partial t^2}=0 \tag{2.32}
$$

The second part of the left hand side in (2.32) contains three curl operations, but can be reduced by applying the rearranged form of the calculation rule in (2.24) and setting $\vec{u}=\left(\nabla\times\vec{\psi}\right)$ such that

$$
\Delta\vec{u}=\nabla(\nabla\cdot\vec{u})-\nabla\times(\nabla\times\vec{u})\Rightarrow\nabla\times\left(\nabla\times\nabla\times\vec{\psi}\right)=\nabla\left(\nabla\cdot\left(\nabla\times\vec{\psi}\right)\right)+\nabla^2\left(\nabla\times\vec{\psi}\right)=\Delta\left(\nabla\times\vec{\psi}\right)
$$

Using this rule, equation (2.32) becomes

$$
(\lambda+2\mu)\nabla\left(\Delta\varphi\right)+\mu\Delta\left(\nabla\times\vec{\psi}\right)-\rho\frac{\partial^2\left(\nabla\varphi\right)}{\partial t^2}-\rho\frac{\partial^2\left(\nabla\times\vec{\psi}\right)}{\partial t^2}=0 \tag{2.33}
$$

By rearranging the terms in (2.33) and subsequently pulling out the gradient and the curl operators, the following is finally obtained

$$
\begin{aligned}
&\left((\lambda+2\mu)\nabla\left(\Delta\varphi\right)-\rho\frac{\partial^2\left(\nabla\varphi\right)}{\partial t^2}\right)+\left(\mu\Delta\left(\nabla\times\vec{\psi}\right)-\rho\frac{\partial^2\left(\nabla\times\vec{\psi}\right)}{\partial t^2}\right)=0\Leftrightarrow\\
&\nabla\left[(\lambda+2\mu)\Delta\varphi-\rho\frac{\partial^2\varphi}{\partial t^2}\right]+\nabla\times\left[\mu\Delta\vec{\psi}-\rho\frac{\partial^2\vec{\psi}}{\partial t^2}\right]=0
\end{aligned}
\tag{2.34}
$$

The final deduction in (2.34) is possible as the order of differentiation has no effect and the elastic constants do not vary with position. Consequently, the first term in equation (2.34) is the gradient of the scalar potential function φ, and the second term is the curl of the vector potential function $\vec{\psi}$, both of which are functions of time and space. As the right hand side is zero, the two terms must be equal. Hence, one possible solution of the equation is to set each term in brackets to zero as

$$
(\lambda+2\mu)\Delta\varphi-\rho\frac{\partial^2\varphi}{\partial t^2}=0\Leftrightarrow\boxed{\Delta\varphi-\frac{\rho}{\lambda+2\mu}\frac{\partial^2\varphi}{\partial t^2}=0} \tag{2.35}
$$

and

$$\mu\Delta\vec{\psi} - \rho\frac{\partial^2\vec{\psi}}{\partial t^2} = 0 \Leftrightarrow \boxed{\Delta\vec{\psi} - \frac{\rho}{\mu}\frac{\partial^2\vec{\psi}}{\partial t^2} = 0} \tag{2.36}$$

Consequently, the introduction of the Helmholtz's theorem and decomposition has made it possible to separate the coupled elastodynamic equations of motion for an isotropic medium, equation (2.25), into two uncoupled 2nd order differential equations, i.e. (2.35) and (2.36).

This observation is an important turning point, as it is recognizable that equations (2.35) and (2.36) are the scalar wave equation and vector wave equation, respectively, i.e. two homogeneous, 2nd order partial differential equations. This statement is easily shown by observing the general form of a wave equation given by [Sadd, 2004]

$$\frac{\partial^2\vec{u}}{\partial x^2} - \frac{1}{c^2}\frac{\partial^2\vec{u}}{\partial t^2} = 0 \tag{2.37}$$

with c being the phase speed of a wave, which is the rate at which the phase of the wave propagates in space. Comparing the wave equation to equations (2.35) and (2.36), these have the following phase speeds

$$\Delta\varphi - \frac{\rho}{\lambda+2\mu}\frac{\partial^2\varphi}{\partial t^2} = 0 \Rightarrow \frac{\partial^2\varphi}{\partial x^2} - \frac{\rho}{\lambda+2\mu}\frac{\partial^2\vec{u}}{\partial t^2} = 0 \Rightarrow \frac{1}{\alpha^2} = \frac{\rho}{\lambda+2\mu} \Leftrightarrow \alpha = \sqrt{\frac{\lambda+2\mu}{\rho}}$$

and (2.38)

$$\Delta\vec{\psi} - \frac{\rho}{\mu}\frac{\partial^2\vec{\psi}}{\partial t^2} = 0 \Rightarrow \frac{\partial^2\vec{\psi}}{\partial x^2} - \frac{\rho}{\mu}\frac{\partial^2\vec{u}}{\partial t^2} = 0 \Rightarrow \frac{1}{\beta^2} = \frac{\rho}{\mu} \Leftrightarrow \beta = \sqrt{\frac{\mu}{\rho}}$$

respectively. It can be seen that the two phase speeds, α and β, for the two wave equations are proportional to the square root of the elastic constants and inversely proportional to the square root of the material density. A more precise definition of the two is the following:

- α - The speed of free dilatation waves in an unbounded elastic medium, also known as primary or *P*-waves
- β - The speed of free shear waves, also known as secondary or *S*-waves

Hence, the *P*-waves are associated with the change of volume in an elastic medium, i.e. dilatational disturbance, and thereby with the scalar potential φ. Equivalently, the rotational *S*-waves are associated with the vector potential ψ. Thus, the *P*-waves involve no rotation and propagate in the interior of an elastic medium at speed α, while rotational *S*-waves, involving no volume changes, propagate at speed β. The ratio of the two wave speeds can be expressed as

$$k = \frac{\alpha}{\beta} = \sqrt{\frac{\lambda+2\mu}{\mu}} = \sqrt{\frac{2-2\nu}{1-2\nu}} \tag{2.39}$$

For e.g. the grout having the Poisson's ratio $\nu = 0.19$, the ratio in (2.39) is $k \simeq \sqrt{2.6129}$. As the Poisson's ratio never exceeds 0.5, it can be seen that $\alpha > \beta$, thus *P*-waves are the primary waves.

Consequently, the elastic wave equations in (2.35) and (2.36) describe the propagation of the two types of waves in an isotropic and homogeneous elastic continuum, also known as seismic body waves studied in e.g. geology [Stein, 1994]. Due to this observation, the two wave equations can be expressed as

$$\begin{aligned} \Delta\varphi - \frac{1}{\alpha^2}\frac{\partial^2\varphi}{\partial t^2} &= 0 \\ \Delta\vec{\psi} - \frac{1}{\beta^2}\frac{\partial^2\vec{\psi}}{\partial t^2} &= 0 \end{aligned} \tag{2.40}$$

Consequently, the four potential components describing the displacement field by the Helmholtz decomposition, must satisfy the two equations in (2.40). With that being the case, the entire problem can be solved, presuming that the displacements along the boundaries are prescribed. However, the four potentials solving the problem are not unique, as several different combinations of the four may generate the same displacement field $\vec{u}$. This is easily reasoned, because there are four unknown potentials, as given in (2.27), but only three displacement components, u_x, u_y and u_z. One way of calibrating this inconsistence is by utilizing the part of Helmholtz theorem stating that the vector potential associated with the rotational part of the displacement field must be divergence-free. Thus, as its divergence is arbitrary, it is convenient to choose $\vec{\psi}$ with zero divergence [Sadd, 2004], i.e.

$$\nabla \cdot \vec{\psi} = 0 \tag{2.41}$$

Applying the definition in (2.41) to a 3D problem allows for obtaining a consistent system with the number of unknown potential functions matching the number of displacement components. However, before proceeding with application of the theory presented so far, it is convenient to present the problem in cylindrical coordinates, considering that the present problem is axis-symmetric. This is conducted in the following subsection, followed by the derivation of the boundary conditions of the present problem.

2.4.2 Problem Presentation in Cylindrical Coordinates

Various calculation rules and vector identities in both Cartesian and cylindrical coordinates are summarized in Appendix 4. Furthermore, the basic field equations are given for these sets of coordinates in Appendix 5. Prior to further derivation of the solution to the present problem in cylindrical coordinates, the theory presented so far is summarized in the following, remembering that $\vec{u} = u(r,\theta,z,t)$, $\varphi = \varphi(r,\theta,z,t)$ and $\vec{\psi} = \psi(r,\theta,z,t)$ in cylindrical coordinates.

The elastodynamic equations of motion from (2.25) are given as:

$$(\lambda+2\mu)\nabla\left(\nabla\cdot\vec{u}\right)-\mu\nabla\times\left(\nabla\times\vec{u}\right)-\rho\frac{\partial^2\vec{u}}{\partial t^2}=0$$

The displacement field solving these equations can be obtained by (2.26):

$$\vec{u}=\nabla\varphi+\nabla\times\vec{\psi}$$

The potentials φ and $\vec{\psi}$ must satisfy the wave equations in (2.40):

$$\Delta\varphi-\frac{1}{\alpha^2}\frac{\partial^2\varphi}{\partial t^2}=0$$

$$\Delta\vec{\psi}-\frac{1}{\beta^2}\frac{\partial^2\vec{\psi}}{\partial t^2}=0$$

To obtain consistency, the vector potential must satisfy (2.41):

$$\nabla\cdot\vec{\psi}=0$$

Consequently, the system outlined above is finally dependent on the condition in (2.41). An expression for the displacement field that satisfies this condition has been derived for the case of cylindrical coordinates in e.g. [Guz, 1986] and [Morse, 1953]. This expression is composed of three independent scalar potential functions, φ,ψ_1,ψ_2 as

$$u(r,\theta,z)=\nabla\varphi(r,\theta,z)+\nabla\times e_3\psi_1(r,\theta,z)+\nabla\times\nabla\times e_3\psi_2(r,\theta,z) \tag{2.42}$$

with e_3 = (0,0,1) being the unit vector collinear with the z axis. It can be seen that the displacement field in (2.42) does not include the time dependence. Recalling that (2.40) are the elastic wave equations in three dimensions describing the propagation of waves in an isotropic elastic medium, they account for both the transverse and the longitudinal motion of the medium. The order of these equations implies that the potential functions must be twice continuously differentiable functions. This is generally the property of *harmonic* functions, which is also governed by the fact that potential theory is often characterized as the study of harmonic functions [Weisstein, 2009].

In relation to the abovementioned, the grout in the grouted connection can be assumed to exhibit *time-harmonic* behaviour. This implies that all the displacement, force and moment components contain a harmonic factor $e^{i\omega t}$, which contains the complex number $i=\sqrt{-1}$ and the angular frequency ω, measuring the rate of rotation. More details can be found in Appendix 6 and e.g. [Rao, 2004]. Consequently, by introducing this harmonic factor, expression in (2.42) can be written as

$$u(r,\theta,z,t)=u(r,\theta,z)e^{i\omega t} \tag{2.43}$$

By applying the displacement field expressed by (2.43), it is finally possible to approach the problem in all four dimensions. However, to solve for the potential functions that describe the displacements, it is necessary

to define the boundary conditions in the grouted connection which must be satisfied. This is elaborated in the next section.

2.4.3 Boundary Conditions for the Grouted Connection

In order to obtain boundary conditions in the grouted connection, it is necessary to determine the behavior of the whole structure under the loading condition specified in section 1.5.1. The idealized monopile foundation structure presented in Figure 1-4 in Chapter 1 is repeated, and loaded by a horizontal force P at the top of the transition piece, as shown in Figure 2-5*a)*.

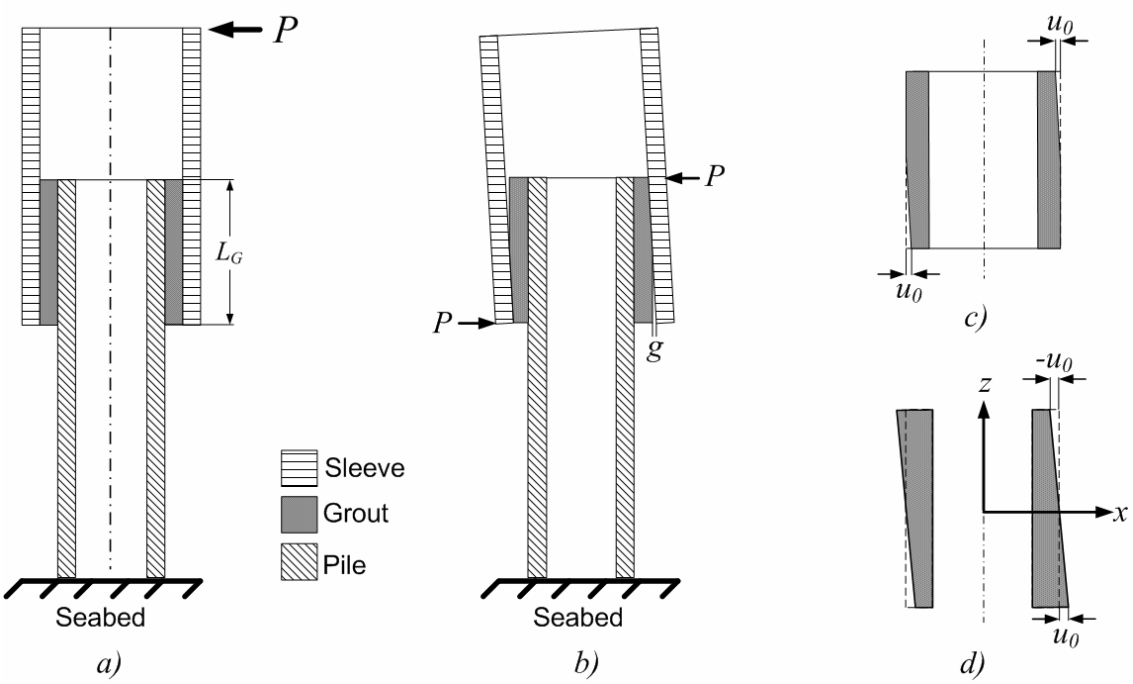

Figure 2-5: Structural behaviour of the grout due to horizontal load transfer.

It is presumed that the pile is fully fixed at the seabed surface. The load is transferred to the grouted connection as a moment produced by the force P acting through the length of the transition piece L_s. This moment is assumed transferred as a force-couple in the connection, as shown in Figure 2-5*b)*, which compress the one side of the grout at the top and the opposite side at the bottom of the connection.

As discussed in section 1.3.2, there is no physical bonding between the grout and the steel, a minor gap g may occur at the opposite sides of the force-couples. It is reasonable to state that the grout will be the first to deform and gradually fail, as its strength is much lower compared to the steel pipes in the connection; see Appendix 3. An exaggerated deformed state of the grout is illustrated in Figure 2-5*c)*, where the magnitude of displacement at the two ends is assumed equal due to symmetry and denoted u_0. Furthermore, the presence of the gap involves nonlinear description of the displacement, which introduces significant difficulties in the analytical treatment. For this reason, it is assumed that the grout *is bonded* to the steel. In that case, the ex-

pected deformed state of the grout is shown in Figure 2-5*d)*, where the undeformed grout surface is shown by the dashed line and the referencing coordinate system is shown as well. Consequently, the displacement of one side of the grout surface is assumed linearly decreasing from the maximum value $u(z = L_G/2) = -u_0$ at the top, corresponding to compression, to the equivalent but positive value at the bottom $u(z = -L_G/2) = u_0$, corresponding to tension. Additionally, it is assumed that the minimum effective contact length in the connection will be approximately one half of the connection length L_G, such that the displacement $u(z = 0) = 0$, as shown in Figure 2-5*d)*. A representation of the grout cylinder in cylindrical coordinates as well as definition of its boundary surfaces is illustrated in Figure 2-6*a)* and *b)*.

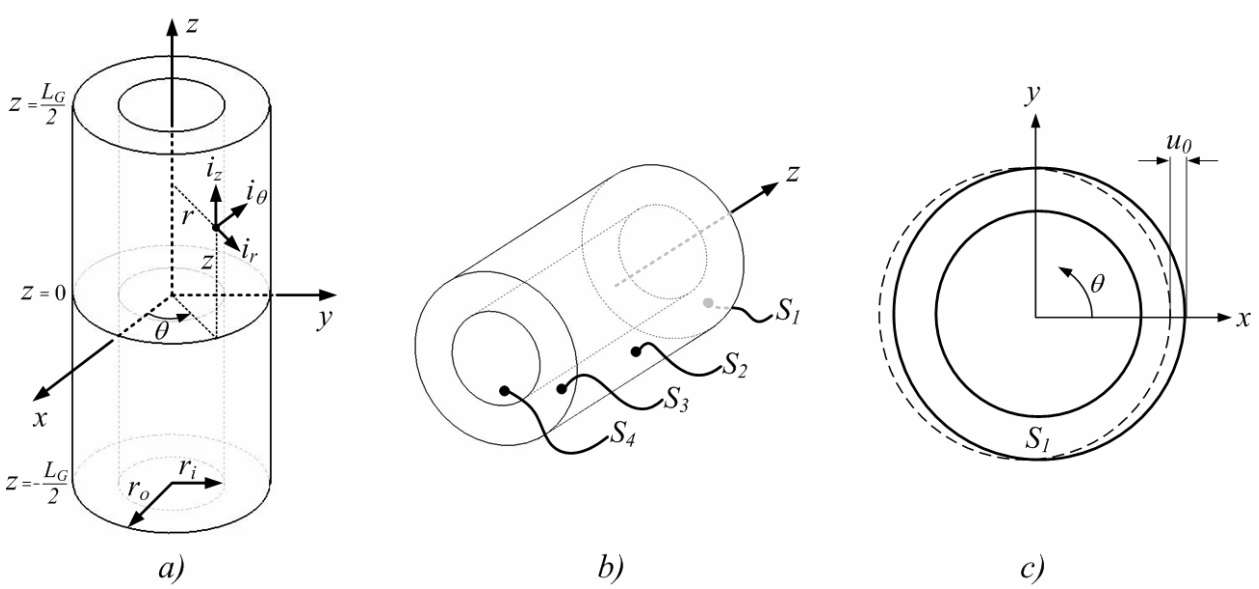

Figure 2-6: Illustration of the grout cylinder boundaries with the referencing coordinate system.

The previously discussed simplifications finally provide the conditions along the boundary surfaces of the grout. However, an additional assumption is illustrated in Figure 2-6*c)*, proposing that the displacement of the grout boundary surfaces S_1 and S_2, i.e. the top and the bottom of the connection, is taking place in a rigid manner. This is presumed due to the fact that the steel tubes are much stiffer than the grout and are therefore assumed to retain their circular shapes with no ovalization. Consequently, the displacement at surface S_1 and equivalently S_3 can be advantageously described by the trigonometric functions *cosine* and *sine*. Thus, the boundary conditions for these surfaces can be written in terms of the circumferential coordinate and time as

$$\begin{aligned} S_1(r = r_o, z = L_G/2) &: \quad u^*_{r1}(\theta,t) = -u_0\cos(\theta)e^{i\omega t} \;;\; u^*_{\theta 1}(\theta,t) = -u_0\sin(\theta)e^{i\omega t} \;;\; u^*_{z1}(\theta,t) = 0 \\ S_3(r = r_o, z = -L_G/2) &: \quad u^*_{r3}(\theta,t) = u_0\cos(\theta)e^{i\omega t} \;;\; u^*_{\theta 1}(\theta,t) = u_0\sin(\theta)e^{i\omega t} \;;\; u^*_{z1}(\theta,t) = 0 \end{aligned} \tag{2.44}$$

From the definition in (2.44), it can be seen that the angular dependence can be factored out from the expression for the displacement field in (2.43) as well, without loss of consistency. In Figure 2-6*c)*, it is also assumed that the inner boundary surface of the grout S_4 is completely fixed, such that the boundaries become

$$S_4(r=r_i): \qquad u_{r1}^*(\theta,z,t)=0 \quad ; \quad u_{\theta 1}^*(\theta,z,t)=0 \quad ; \quad u_{z1}^*(\theta,z,t)=0 \tag{2.45}$$

The boundary condition for S_2, i.e. the outer vertical surface along the length L_G, can be obtained from the assumption shown in Figure 2-6*d)*, where the displacement can be expressed linearly as

$$u(z)=2u_0\frac{z}{L_G} \tag{2.46}$$

Finally, applying the circumferential dependence to equation (2.46) lead to the boundary conditions for surface S_2 as

$$S_2(r=r_o): \quad u_{r1}^*(\theta,z,t)=-2u_0\frac{z}{L_G}\cos(\theta)e^{i\omega t} \quad ; \quad u_{\theta 1}^*(\theta,z,t)=-2u_0\frac{z}{L_G}\sin(\theta)e^{i\omega t} \quad ; \quad u_{z1}^*(\theta,z,t)=0 \tag{2.47}$$

Consequently, the displacement boundary conditions have been defined for the entire grout cylinder. The total results are summarized in Table 2-1 below.

Boundary Surface	*Boundary Condition*
$S_1(r=r_o, z=L_G/2)$	$u_{r1}^*(\theta,t)=-u_0\cos(\theta)e^{i\omega t} \quad ; \quad u_{\theta 1}^*(\theta,t)=-u_0\sin(\theta)e^{i\omega t} \quad ; \quad u_{z1}^*(\theta,t)=0$
$S_3(r=r_o, z=-L_G/2)$	$u_{r3}^*(\theta,t)=u_0\cos(\theta)e^{i\omega t} \quad ; \quad u_{\theta 3}^*(\theta,t)=u_0\sin(\theta)e^{i\omega t} \quad ; \quad u_{z3}^*(\theta,t)=0$
$S_2(r=r_o)$	$u_{r2}^*(\theta,z,t)=-2u_0\frac{z}{L_G}\cos(\theta)e^{i\omega t} \quad ; \quad u_{\theta 2}^*(\theta,z,t)=-2u_0\frac{z}{L_G}\sin(\theta)e^{i\omega t} \quad ; \quad u_{z2}^*(\theta,z,t)=0$
$S_4(r=r_i)$	$u_{r4}^*(\theta,z,t)=0 \quad ; \quad u_{\theta 4}^*(\theta,z,t)=0 \quad ; \quad u_{z4}^*(\theta,z,t)=0$

Table 2-1: Overview of the boundary conditions for the grout cylinder.

Having the full description of the boundary conditions in Table 2-1 and the consistent expression for the displacement field in (2.43), it is now possible to advance with the solution of this field for the three dimensional grout cylinder. This is elaborated in the next section.

2.5 Application of Potential Functions on the Grouted Connection

It has been demonstrated in the previous section that solution to a problem in continuum mechanics can be approached by means of three potential functions only. The three functions are obtained by solving the three wave equations, given as

$$\begin{aligned}
&\Delta\varphi(r,\theta,z,t)-\frac{1}{\alpha^2}\frac{\partial^2\varphi(r,\theta,z,t)}{\partial t^2}=0\\
&\Delta\psi_1(r,\theta,z,t)-\frac{1}{\beta^2}\frac{\partial^2\psi_1(r,\theta,z,t)}{\partial t^2}=0\\
&\Delta\psi_2(r,\theta,z,t)-\frac{1}{\beta^2}\frac{\partial^2\psi_2(r,\theta,z,t)}{\partial t^2}=0
\end{aligned} \tag{2.48}$$

Observing the expressions in (2.48), it is noticeable that one of the parts contains spatial derivatives with respect to space and the other one solely with respect to time. Therefore it is convenient to assume that separation of variables is applicable. This is exemplified by e.g. the first wave equation in (2.48), which can be expressed by factoring out the time-harmonic part as $\varphi(r,\theta,z,t)=\varphi(r,\theta,z)e^{-i\omega t}$. Substituting this product in (2.48) and rearranging, the following is obtained

$$\Delta\varphi(r,\theta,z)e^{-i\omega t}=\frac{1}{\alpha^2}\frac{\partial^2\varphi(r,\theta,z)e^{-i\omega t}}{\partial t^2} \tag{2.49}$$

Noting that $\frac{\partial^2}{\partial t^2}e^{-i\omega t}=i^2\omega^2e^{-i\omega t}$, substituting this into equation (2.49) and reducing yields

$$\Delta\varphi(r,\theta,z)e^{-i\omega t}=\frac{1}{\alpha^2}i^2\omega^2\varphi(r,\theta,z)e^{-i\omega t}\Leftrightarrow\left(\Delta+\frac{\omega^2}{\alpha^2}\right)\varphi(r,\theta,z)=0 \tag{2.50}$$

Utilizing the definition $\omega=k\cdot\alpha$ and rearranging to $k^2=\omega^2/\alpha^2$, with k being the wave vector representing the wave, equation (2.50) is in fact just a form of *Helmholtz equation* [Franca, 2009]. Consequently, the result from applying the technique of separation of variables is the Helmholtz equation, which represents the time-independent form of the original wave equation. This reduces the complexity of the analysis considerably. Applying the same procedure to the two other wave equations, the three equations in (2.48) are simplified to

$$\left(\Delta+\frac{\omega^2}{\alpha^2}\right)\varphi(r,\theta,z)=0\quad;\quad\left(\Delta+\frac{\omega^2}{\beta^2}\right)\psi_1(r,\theta,z)=0\quad;\quad\left(\Delta+\frac{\omega^2}{\beta^2}\right)\psi_2(r,\theta,z)=0 \tag{2.51}$$

Consequently, obtaining the three potential functions that solve the three equations in (2.51) solves the displacement field expressed by (2.43) as well. The displacement components derived by (2.43) are given in Table 2-2, noticing that the time dependence can now be omitted.

The Displacement Components
$u_r(r,\theta,z)=\frac{\partial\varphi(r,\theta,z)}{\partial r}+\frac{1}{r}\frac{\partial\psi_1(r,\theta,z)}{\partial\theta}+\frac{\partial^2\psi_2(r,\theta,z)}{\partial r\partial z}$
$u_\theta(r,\theta,z)=-\frac{1}{r}\frac{\partial\varphi(r,\theta,z)}{\partial\theta}-\frac{\partial\psi_1(r,\theta,z)}{\partial r}+\frac{1}{r}\frac{\partial^2\psi_2(r,\theta,z)}{\partial z\partial\theta}$
$u_z(r,\theta,z)=\frac{\partial\varphi(r,\theta,z)}{\partial z}-\frac{1}{r}\frac{\partial\psi_2(r,\theta,z)}{\partial r}-\frac{\partial^2\psi_2(r,\theta,z)}{\partial r^2}-\frac{1}{r^2}\frac{\partial^2\psi_2(r,\theta,z)}{\partial\theta^2}$

Table 2-2: The displacement components generated by three potential functions.

As discussed in the previous subsection, the circumferential dependence in can be factored out without loss of generality. Comparing the displacement components in Table 2-2 and the boundary conditions for surface S_2 in Table 2-1, the potential functions are chosen as

$$\varphi(r,\theta,z)=\tilde{\varphi}(r,z)\cos\theta \;\; ; \; \psi_1(r,\theta,z)=\tilde{\psi}_1(r,z)\sin\theta \;\; ; \; \psi_2(r,\theta,z)=\tilde{\psi}_2(r,z)\cos\theta \tag{2.52}$$

Consequently, the three potential functions are in fact *functionals*, which are by definition "functions of functions". However, the term functions will be used anyway. The choice of trigonometric functions for φ and ψ_1 directly follow from the boundary conditions, while this is chosen arbitrary for ψ_2, as the displacement component u_z is assumed zero everywhere. Furthermore, it appears convenient to factor out the z dependence as well. The u_r and u_θ components for boundary surface S_2 vary along the z-axis as explicitly expressed in Table 2-1 and shown in Figure 2-5*d)*. The figure illustrates the odd characteristic of the displacement, i.e. skew-symmetric, as it changes sign across the centre of the grout, i.e. $z = 0$. For the interval [$-L_G$ / 2, L_G / 2], this can be written as

$$u_{odd}(z)=\begin{cases} u(z) \;\; , & 0<z<L_G/2 \\ -u(-z), & -L_G/2<z<0 \end{cases}$$

This odd behavior can be expressed by utilizing the odd property of the *sine* function. Hence, the *sine* series of $u(z)$ with the period L_G are given by the Fourier expansion series as

$$\sum_{n=1}^{\infty}\sin\left(\frac{n\pi z}{L}\right) \tag{2.53}$$

As the expansion series in (2.53) contains infinitely many terms, it is chosen to use one-term approximation, i.e. $n = 1$. So far, the expressions for the potential functions in (2.52) have been exact. Introducing this approximation reduces the quality of the results. However, this can always be improved by including additional terms. Consequently, the following guesses are assumed for the three potential functions

$$\begin{aligned} \varphi(r,\theta,z)&=\tilde{\varphi}_0(r)\cos\theta\sin\frac{\pi z}{L_G} \\ \psi_1(r,\theta,z)&=\tilde{\psi}_{10}(r)\sin\theta\sin\frac{\pi z}{L_G} \\ \psi_2(r,\theta,z,t)&=\tilde{\psi}_{20}(r)\cos\theta\cos\frac{\pi z}{L_G} \end{aligned} \tag{2.54}$$

With the new guesses, the three functions contain functions which are solely dependent on the radial coordinate, as expressed in (2.54). These can now be substituted into the displacement components in Table 2-2. Starting off with u_r and applying the corresponding boundary condition from Table 2-1, in which time dependence is omitted, the following is obtained

$$u_r(r,\theta,z)=u_{r2}^{*}(r,\theta,z)\Leftrightarrow\left(\frac{\partial\varphi(r,\theta,z)}{\partial r}+\frac{1}{r}\frac{\partial\psi_1(r,\theta,z)}{\partial\theta}+\frac{\partial^2\psi_2(r,\theta,z)}{\partial r\partial z}\right)\sin\frac{\pi z}{L_G}=-2u_0\frac{z}{L_G} \tag{2.55}$$

As the left side of equation (2.55) is the approximated expression unlike the exact right side, it is necessary to calibrate the equation. This can be done by means of *Galerkin averaging method* [Shames & Dym, 2003]. This averaging is in this case preformed by multiplying each side in equation (2.55) by the trigonometric part of the left hand side and subsequently integrating both sides over the grout length L_G. Doing this yields the following

$$\begin{gathered}\int_{-L/2}^{L/2}\left(\frac{\partial\tilde{\varphi}_0(r)}{\partial r}+\frac{1}{r}\tilde{\psi}_{1,0}(r)-\frac{\pi}{L_G}\frac{\partial\tilde{\psi}_{2,0}(r)}{\partial r}\right)\sin^2\left(\frac{\pi z}{L_G}\right)dz=\int_{-L/2}^{L/2}-2u_0\frac{z}{L_G}\sin\left(\frac{\pi z}{L_G}\right)dz\Leftrightarrow\\ \frac{\partial\tilde{\varphi}_0(r)}{\partial r}+\frac{1}{r}\tilde{\psi}_{1,0}(r)-\frac{\pi}{L_G}\frac{\partial\tilde{\psi}_{2,0}(r)}{\partial r}=-u_0\frac{8}{\pi^2}\end{gathered}\tag{2.56}$$

Consequently, the Galerkin averaging method has advantageously eliminated the trigonometric dependence, whereby the original equation has been additionally simplified. The same procedure is completed for the remaining displacement components and boundary conditions, conducted in Appendix 8. A general overview of the entire problem is summarized in Table 2-3.

Requirements at the Boundaries	
At surface S_2:	$u_r(r_o)=u_{r2}^*(r_o)\Leftrightarrow\frac{d\tilde{\varphi}_0(r_o)}{dr}+\frac{1}{r_o}\tilde{\psi}_{1,0}(r_o)-\frac{\pi}{L_G}\frac{d\tilde{\psi}_{2,0}(r_o)}{dr}=-u_0\frac{8}{\pi^2}$
	$u_\theta(r_o)=u_{\theta2}^*(r_o)\Leftrightarrow-\frac{1}{r_o}\tilde{\varphi}_0(r_o)-\frac{d\tilde{\psi}_{1,0}(r_o)}{dr}+\frac{\pi}{L_G r_o}\tilde{\psi}_{2,0}(r_o)=u_0\frac{8}{\pi^2}$
	$u_z(r_o)=u_{z2}^*(r_o)\Leftrightarrow\frac{\pi}{L_G}\tilde{\varphi}_0(r_o)-\frac{1}{r_o}\frac{d\tilde{\psi}_{2,0}(r_o)}{dr}-\frac{d^2\tilde{\psi}_{2,0}(r_o)}{dr^2}+\frac{1}{r_o^2}\tilde{\psi}_{2,0}(r_o)=0$
At surface S_4:	$u_r(r_i)=u_{r4}^*(r_i)\Leftrightarrow\frac{d\tilde{\varphi}_0(r_i)}{dr}+\frac{1}{r_i}\tilde{\psi}_{1,0}(r_i)-\frac{\pi}{L_G}\frac{d\tilde{\psi}_{2,0}(r_i)}{dr}=0$
	$u_\theta(r_i)=u_{\theta4}^*(r_i)\Leftrightarrow-\frac{1}{r_i}\tilde{\varphi}_0(r_i)-\frac{d\tilde{\psi}_{1,0}(r_i)}{dr}+\frac{\pi}{L_G r_i}\tilde{\psi}_{2,0}(r_i)=0$
	$u_z(r_i)=u_{z4}^*(r_i)\Leftrightarrow\frac{\pi}{L_G}\tilde{\varphi}_0(r_i)-\frac{1}{r_i}\frac{d\tilde{\psi}_{2,0}(r_i)}{dr}-\frac{d^2\tilde{\psi}_{2,0}(r_i)}{dr^2}+\frac{1}{r_i^2}\tilde{\psi}_{2,0}(r_i)=0$
Requirements for the Potential Functions by Substituting (2.54) **into** (2.51)**:**	
$\left(\Delta+\frac{\omega^2}{\alpha^2}\right)\tilde{\varphi}_0(r)\cos\theta\sin\frac{\pi z}{L_G}=0\Leftrightarrow\frac{d^2\tilde{\varphi}_0(r)}{dr^2}+\frac{1}{r}\frac{d\tilde{\varphi}_0(r)}{dr}-\left(\frac{1}{r^2}+\frac{\pi^2}{L_G^2}-\frac{\omega^2}{\alpha^2}\right)\tilde{\varphi}_0(r)=0$	
$\left(\Delta+\frac{\omega^2}{\beta^2}\right)\tilde{\psi}_{10}(r)\sin\theta\sin\frac{\pi z}{L_G}=0\Leftrightarrow\frac{d^2\tilde{\psi}_{10}(r)}{dr^2}+\frac{1}{r}\frac{d\tilde{\psi}_{10}(r)}{dr}-\left(\frac{1}{r^2}+\frac{\pi^2}{L_G^2}-\frac{\omega^2}{\beta^2}\right)\tilde{\psi}_{10}(r)=0$	
$\left(\Delta+\frac{\omega^2}{\beta^2}\right)\tilde{\psi}_{2,0}(r)\cos\theta\cos\frac{\pi z}{L_G}=0\Leftrightarrow\frac{d^2\tilde{\psi}_{2,0}(r)}{dr^2}+\frac{1}{r}\frac{d\tilde{\psi}_{2,0}(r)}{dr}-\left(\frac{1}{r^2}+\frac{\pi^2}{L_G^2}-\frac{\omega^2}{\beta^2}\right)\tilde{\psi}_{2,0}(r)=0$	

Table 2-3: General overview of the entire 3D boundary value problem.

The system in Table 2-3 represents six equations that must satisfy the six boundary conditions on the two interface surfaces of the grout. Furthermore, the equations that must be satisfied by the potential functions

solely in terms of the radial coordinate are presented as well. In fact, these second-order ordinary differential equations are just a modified form of the Bessel's equation in cylindrical coordinates, after the German mathematician and astronomer Friedrich Wilhelm Bessel (1784 – 1846). In general, Bessel's equation arises when applying the method of separation of variables to Laplace's equation and the Helmholtz equation in cylindrical or spherical coordinates [Britanica, 2009]. Solutions to this equation will be discussed later in this section.

When attempting to solve the system in Table 2-3, it is erroneous to set the angular frequency ω in the three equations to zero and thereby assume pure elastostatics [Slepyan, 1972]. To evaluate this statement, it is convenient to reduce the complexity of the problem by considering a 2D approximation. This is done in the following subsection.

2.5.1 2D Elastostatic Solution by Assuming $\omega = 0$

In this analysis, it is assumed that the 3D grout cylinder can be sliced into horizontal plane segments of the cross section, and solve for these one by one. This is consistent as the boundary conditions are fully described. With the results for the 3D case presented in Table 2-3, this is just a matter of reducing the system variables to 2D. By omitting the z-coordinate dependence and setting the angular frequency to $\omega = 0$, the three Bessel's equations reduce to following two

$$\frac{d^2\tilde{\varphi}_0(r)}{dr^2}+\frac{1}{r}\frac{d\tilde{\varphi}_0(r)}{dr}-\frac{1}{r^2}\tilde{\varphi}_0(r)=0 \quad ; \quad \frac{d^2\tilde{\psi}_{1,0}(r)}{dr^2}+\frac{1}{r}\frac{d\tilde{\psi}_{1,0}(r)}{dr}-\frac{1}{r^2}\tilde{\psi}_{1,0}(r)=0 \tag{2.57}$$

Furthermore, the boundary conditions to be satisfied in 2D are

$$\begin{array}{ll} \text{For boundary surface } S_2: & \text{For boundary surface } S_4: \\ \dfrac{\partial\tilde{\varphi}_0(r)}{\partial r}+\dfrac{1}{r}\tilde{\psi}_{1,0}(r)=-u_0\dfrac{8}{\pi^2} & \dfrac{\partial\tilde{\varphi}_0(r)}{\partial r}+\dfrac{1}{r}\tilde{\psi}_{1,0}(r)=0 \\ -\dfrac{1}{r}\tilde{\varphi}_0(r)-\dfrac{\partial\tilde{\psi}_{1,0}(r)}{\partial r}=u_0\dfrac{8}{\pi^2} & -\dfrac{1}{r}\tilde{\varphi}_0(r)-\dfrac{\partial\tilde{\psi}_{1,0}(r)}{\partial r}=0 \end{array} \tag{2.58}$$

The equations in (2.57) correspond to Laplace's equations in cylindrical coordinates, i.e. $\Delta\tilde{\varphi}_0=0$ and $\Delta\tilde{\psi}_{1,0}=0$. Since these are second-order differential equations, there must be two linearly independent solutions for each. By simple integration, the general solutions to these is given in terms of polynomial functions as

$$\tilde{\varphi}_0(r)=c_1 r+\frac{c_2}{r} \quad ; \quad \tilde{\psi}_{1,0}(r)=c_3 r+\frac{c_4}{r} \tag{2.59}$$

with c_i being the integration constants. Substituting the general solutions from (2.59) into (2.58), the following is obtained

For boundary surface S_2: For boundary surface S_4:

$$u_r(r_o):\ c1-\frac{c2}{r_o^2}+c3+\frac{c4}{r_o^2}=-u_0\frac{8}{\pi^2} \qquad u_r(r_i):\ c1-\frac{c2}{r_i^2}+c3+\frac{c4}{r_i^2}=0 \tag{2.60}$$

$$u_\theta(r_o):\ -c1-\frac{c2}{r_o^2}-c3+\frac{c4}{r_o^2}=u_0\frac{8}{\pi^2} \qquad u_\theta(r_i):\ -c1-\frac{c2}{r_i^2}-c3+\frac{c4}{r_i^2}=0$$

It is noticeable that each of the four conditions in (2.60) contains the four constants which in pair are of the same form. For instance taking the $u_r(r_o)$ for surface S_2, the constants c_1 and c_3 are of the same form, as is the case for c_2 and c_4. This means that they can be summed to a single constant, say $A = c_1 + c_3$, and equivalently say $B = -c_2 + c_4$. such that the condition becomes

$$u_r(r_o):\ c1-\frac{c2}{r_o^2}+c3+\frac{c4}{r_o^2}=-u_0\frac{8}{\pi^2}\Rightarrow A+\frac{B}{r_o^2}=-u_0\frac{8}{\pi^2}$$

Consequently, it has been shown that the four constants can be expressed by just two, and by still having the four equations in (2.60) to be satisfied, this leads to an over defined system, which cannot be solved. Thus, simplifying the elastodynamic case to elastostatic by simply reducing the original Bessel's equations into Laplace's, i.e. setting $\omega = 0$, is not a valid option. However, in stead of omitting the dynamic source completely, it is tempting to include this to solve the system in 2D and evaluate the effect of varying the angular frequency ω. Before performing this, it is essential to have an exact solution of corresponding elastostatic 2D problem for comparison. One method is elaborated in the next subsection.

2.5.2 2D Elastostatic Solution

Since it has been proven unfortunate to directly omit the dynamic source, another theory that returns to the original wave equations presented in (2.48) can be applied. The simple forms of these in 2D as well as their general solutions obtained by simple integration, are given as

$$\Delta\varphi-\frac{1}{\alpha^2}\frac{\partial^2\varphi}{\partial t^2}=0 \quad ; \quad \Delta\psi_1-\frac{1}{\beta^2}\frac{\partial^2\psi_1}{\partial t^2}=0$$
$$\varphi=\varphi_1+t^2A+tB \quad ; \quad \psi=\psi_1+t^2C+tD \tag{1.61}$$

According to [Slepyan, 1972], the integration constants A, B, C and D in the solutions in (1.61) must satisfy the following conditions:

$$\begin{aligned}&1.\quad \Delta A=\Delta B=\Delta C=\Delta D=0\\&2.\quad \nabla A+\nabla\times C=\nabla B+\nabla\times D=0\end{aligned} \tag{1.62}$$

Substituting the solutions into equations in (1.61) the following is obtained

$$\Delta\varphi - \frac{1}{\alpha^2}\frac{\partial^2\varphi}{\partial t^2} = 0 \Leftrightarrow \Delta\varphi_1 + t^2\Delta A + t\Delta B - \frac{1}{\alpha^2}(2A) = 0$$

and (1.63)

$$\Delta\psi - \frac{1}{\beta^2}\frac{\partial^2\psi}{\partial t^2} = 0 \Leftrightarrow \Delta\psi_1 + t^2\Delta C + t\Delta D - \frac{1}{\beta^2}(2C) = 0$$

Due to the 1st set of conditions in (1.62), the constants A, B, C and D in (1.63) are easily isolated giving

$$\Delta\varphi_1 - \frac{1}{\alpha^2}(2A) = 0 \Leftrightarrow A = \frac{\alpha^2}{2}\Delta\varphi_1 \;;\; B = 0 \quad ; \quad \Delta\psi_1 - \frac{1}{\beta^2}(2C) = 0 \Leftrightarrow C = \frac{\beta^2}{2}\Delta\psi_1 \;;\; D = 0 \tag{1.64}$$

Applying the 1st set of conditions in (1.62) on A and C again gives

$$\begin{aligned}
\Delta A = 0 \Leftrightarrow \Delta\left(\frac{\alpha^2}{2}\Delta\varphi_1\right) = \Delta\Delta\varphi_1 = \left(\frac{\partial^2}{\partial r^2} + \frac{1}{r}\frac{\partial}{\partial r} + \frac{1}{r^2}\frac{\partial^2}{\partial\theta^2}\right)\left(\frac{\partial^2\varphi_1}{\partial r^2} + \frac{1}{r}\frac{\partial\varphi_1}{\partial r} + \frac{1}{r^2}\frac{\partial^2\varphi_1}{\partial\theta^2}\right) = 0 \\
\Delta C = 0 \Leftrightarrow \Delta\left(\frac{\beta^2}{2}\Delta\psi_1\right) = \Delta\Delta\psi_1 = \left(\frac{\partial^2}{\partial r^2} + \frac{1}{r}\frac{\partial}{\partial r} + \frac{1}{r^2}\frac{\partial^2}{\partial\theta^2}\right)\left(\frac{\partial^2\psi_1}{\partial r^2} + \frac{1}{r}\frac{\partial\psi_1}{\partial r} + \frac{1}{r^2}\frac{\partial^2\psi_1}{\partial\theta^2}\right) = 0
\end{aligned} \tag{1.65}$$

Hence, the two potential functions φ_1 and ψ_1 must satisfy the biharmonic equations in (1.65), also written as $\nabla^4 f = 0$. As these are 4th order differential equations, there must be four linearly independent solutions and thereby four unknown integration constants for each. Furthermore the 2nd condition in (1.62) must be satisfied for A and C as well. This gives:

$$\nabla A + \nabla\times C = 0 \Leftrightarrow \alpha^2\nabla\Delta\varphi_1 + \beta^2\nabla\times\Delta\psi_1 = 0 \tag{1.66}$$

As the potential functions φ_1 and ψ_1 are here functions of two coordinates and equation (1.66) is a differential equation, there are all together three differential equations that must be satisfied, i.e. two in (1.65) and one in (1.66), containing eight unknown constants altogether. Factoring out the circumferential dependence as done in (2.52), the two 2D potential functions are written as

$$\varphi_1(r,\theta) = \varphi_{10}(r)\cos(\theta) \quad ; \quad \psi_1(r,\theta) = \psi_{10}(r)\sin(\theta) \tag{2.67}$$

Substituting these into the biharmonic equations in (1.65) yields

$$\frac{1}{r^3}\frac{d\Phi_i(r)}{dr} - \frac{1}{r^2}\left(\frac{d^2\Phi_i(r)}{dr^2}\right) + 2\frac{1}{r}\left(\frac{d^3\Phi_i(r)}{dr^3}\right) + \left(\frac{d^4\Phi_i(r)}{dr^4}\right) = 0 \;,\; \Phi_i = \{\varphi_{10}(r), \psi_{10}(r)\} \tag{2.68}$$

It can be seen that the angular coordinate can be cancelled out in (2.68), such that the general solution for the two in terms of radial coordinate only is given as:

$$\varphi_{10}(r) = c_1 r + c_2 r^3 + \frac{1}{r}c_3 + r\ln(r)c_4 \quad ; \quad \psi_{10}(r) = c_5 r + c_6 r^3 + \frac{1}{r}c_7 + r\ln(r)c_8 \tag{1.69}$$

Next, the general solutions can be substituted to obtain the displacement components. Using the general solutions of the wave equations in (1.61) and applying the 2nd condition in (1.62) the displacement field of the form given in (2.42), reduces to

$$\vec{u} = \nabla\varphi_1 + t^2\underbrace{\left(\nabla A + \nabla\times C\right)}_{0} + t\underbrace{\left(\nabla B + \nabla\times D\right)}_{0} + \nabla\times\psi_1 = \nabla\varphi_1 + \nabla\times\psi_1 \tag{1.70}$$

Consequently, the time dependence can be omitted as a direct result of the prescribed conditions in (1.62). Substituting the general solutions from (1.69) into (2.67), the displacement field in (1.70) becomes:

$$\begin{bmatrix} u_r(r,\theta) \\ u_\theta(r,\theta) \end{bmatrix} = \begin{bmatrix} \left(c_1 + 3c_2r^2 - \frac{c_3}{r^2} + c_4\ln(r) + c_4 + c_5 + c_6r^2 + \frac{c_7}{r^2} + c_8\ln(r)\right)\cos(\theta) \\ \left(-c_1 - c_2r^2 - \frac{c_3}{r^2} - c_4\ln(r) - c_5 - 3c_6r^2 + \frac{c_7}{r^2} - c_8\ln(r) - c_8\right)\sin(\theta) \end{bmatrix} \tag{1.71}$$

Hence, there are eight unknown integration constants in the displacement field in (1.71) but only four boundary conditions in the 2D problem, which at first glance suggests inconsistency. However, vector equation (1.66) must be satisfied as well. Substituting the general solutions into (1.66) yields

$$\begin{gathered} \alpha^2\nabla\Delta\left(c_1r + c_2r^3 + \frac{1}{r}c_3 + r\ln(r)c_4\right) + \beta^2\nabla\times\Delta\left(c_5r + c_6r^3 + \frac{1}{r}c_7 + r\ln(r)c_8\right) = 0 \\ \Updownarrow \\ 8\alpha^2c_2 - \frac{2\alpha^2c_4}{r^2} + 8\beta^2c_6 + \frac{2\beta^2c_8}{r^2} = 0 \quad ; \quad -8\alpha^2c_2 - \frac{2\alpha^2c_4}{r^2} - 8\beta^2c_6 + \frac{2\beta^2c_8}{r^2} = 0 \end{gathered} \tag{2.72}$$

Observing the two conditions in (2.72), there are two pairs of comparable parts in each. Therefore, the following relations must be valid

$$\left.\begin{aligned} \alpha^2 8c_2 - \frac{\alpha^2 2c_4}{r^2} + \beta^2 8c_6 + \frac{\beta^2 2c_8}{r^2} = 0 &\Rightarrow \begin{matrix} \alpha^2c_2 + \beta^2c_6 = 0 \\ -\alpha^2c_4 + \beta^2c_8 = 0 \end{matrix} \\ -\alpha^2 8c_2 - \frac{\alpha^2 2c_4}{r^2} - \beta^2 8c_6 + \frac{\beta^2 2c_8}{r^2} = 0 &\Rightarrow \begin{matrix} -\alpha^2c_2 - \beta^2c_6 = 0 \\ -\alpha^2c_4 + \beta^2c_8 = 0 \end{matrix} \end{aligned}\right\} \Leftrightarrow \boxed{\begin{matrix} c_2 = -c_6\dfrac{\beta^2}{\alpha^2} \\ c_4 = c_8\dfrac{\beta^2}{\alpha^2} \end{matrix}} \tag{2.73}$$

Consequently, there are only two out of four independent unknowns in (2.72), which reduces the total number of integration constants in the general solution in (1.69) from eight to six. However, there are still only four boundary conditions. Thus, two of the constants must somehow be redundant. To inspect this, it is opportune to observe the reduced form of the obtained solutions to the biharmonic equations in (1.69), now being

$$\varphi_1(r,\theta) = \left(c_1r - c_6\frac{\beta^2}{\alpha^2}r^3 + \frac{c_3}{r} + c_8\frac{\beta^2}{\alpha^2}r\ln(r)\right)\cos\theta \;\; ; \;\; \psi_1(r,\theta) = \left(c_5r + c_6r^3 + \frac{c_7}{r} + c_8r\ln(r)\right)\sin\theta \tag{2.74}$$

As the functions in (2.74) satisfy the biharmonic equation, which is the squared Laplacian, it is noticeable that two of the parts in these cancel out by a single Laplace operation due to the orders of these parts. Hence

$$\Delta\varphi_1(r,\theta)=\left(-8c_6\frac{\beta^2}{\alpha^2}r+c_8\frac{\beta^2}{\alpha^2}\frac{2}{r}\right)\cos\theta \quad ; \quad \Delta\psi_1(r,\theta)=\left(8c_6r+c_8\frac{2}{r}\right)\sin\theta \tag{2.75}$$

Consequently, the parts containing constants c_1, c_3 , c_5 and c_7 vanish, which means that these can be taken arbitrary, e.g. zero or equal in each of the two solutions. Thus

$$\Delta\left(c_1r+\frac{c_3}{r}\right)=0 \quad \textit{and} \quad \Delta\left(c_5r+\frac{c_7}{r}\right)=0 \quad ; \quad c_1=c_3=0 \;\vee\; c_5=c_7=0 \;\vee\; c_1=c_5 \;\vee\; c_3=c_7$$

Taking e.g. $c_1=c_3=0$, the solutions reduce to:

$$\varphi_1(r,\theta)=\left(-c_6\frac{\beta^2}{\alpha^2}r^3+c_8\frac{\beta^2}{\alpha^2}r\ln(r)\right)\cos\theta \quad ; \quad \psi_1(r,\theta)=\left(c_5r+c_6r^3+\frac{c_7}{r}+c_8r\ln(r)\right)\sin\theta \tag{2.76}$$

Hence, there are four unknowns in (2.76), i.e. c_5, c_6, c_7 and c_8, matching the four boundary conditions for the planar case. The displacement field in (1.71) finally reduces to

$$\begin{bmatrix} u_r(r,\theta) \\ u_\theta(r,\theta) \end{bmatrix}=\begin{bmatrix} \left(-c_6\frac{3\beta^2}{\alpha^2}r^2+c_8\frac{\beta^2}{\alpha^2}\ln(r)+c_8\frac{\beta^2}{\alpha^2}+c_5+c_6r^2+\frac{c_7}{r^2}+c_8\ln(r)\right)\cos(\theta) \\ \left(c_6\frac{\beta^2}{\alpha^2}r^2-c_8\frac{\beta^2}{\alpha^2}\ln(r)-c_5-c_8-3c_6r^2+\frac{c_7}{r^2}-c_8\ln(r)\right)\sin(\theta) \end{bmatrix} \tag{2.77}$$

The entire 2D system, describing the elastostatic boundary value problem for the grouted connection, is reviewed below

$$\begin{aligned} &\textit{At surface } S_2: \begin{cases} -c_6\frac{3\beta^2}{\alpha^2}r^2+c_8\frac{\beta^2}{\alpha^2}\ln(r)+c_8\frac{\beta^2}{\alpha^2}+c_5+c_6r^2+\frac{c_7}{r^2}+c_8\ln(r)=-u_0\frac{8}{\pi^2} \\ \left(c_6\frac{\beta^2}{\alpha^2}r^2-c_8\frac{\beta^2}{\alpha^2}\ln(r)-c_5-c_8-3c_6r^2+\frac{c_7}{r^2}-c_8\ln(r)\right)=u_0\frac{8}{\pi^2} \end{cases} \\ &\textit{At surface } S_4: \begin{cases} -c_6\frac{3\beta^2}{\alpha^2}r^2+c_8\frac{\beta^2}{\alpha^2}\ln(r)+c_8\frac{\beta^2}{\alpha^2}+c_5+c_6r^2+\frac{c_7}{r^2}+c_8\ln(r)=0 \\ \left(c_6\frac{\beta^2}{\alpha^2}r^2-c_8\frac{\beta^2}{\alpha^2}\ln(r)-c_5-c_8-3c_6r^2+\frac{c_7}{r^2}-c_8\ln(r)\right)=0 \end{cases} \end{aligned} \tag{2.78}$$

The system of four equations with four unknowns can be easily solved by mathematical software such as *Wolfram Mathematica*. As the objective of this static solution is to serve for comparison, the next step is to obtain a solution for the 2D elastodynamic case which includes the dynamic source. Detailed procedure follows in the next subsection.

2.5.3 2D Elastodynamic Solution

The 2D elastodynamic solution can be obtained by reducing the explicit solution scheme for the 3D case, presented in Table 2-3. Consequently, the 2D scheme to be solved is summarized in Table 2-4.

Requirements at the Boundaries	
At surface S_2:	$u_r(r_o)=u_{r2}^*(r_o)\Leftrightarrow \frac{d\tilde{\varphi}_0(r_o)}{dr}+\frac{1}{r_o}\tilde{\psi}_{1,0}(r_o)=-u_0\frac{8}{\pi^2}$ $u_\theta(r_o)=u_{\theta 2}^*(r_o)\Leftrightarrow -\frac{1}{r_o}\tilde{\varphi}_0(r_o)-\frac{d\tilde{\psi}_{1,0}(r_o)}{dr}=u_0\frac{8}{\pi^2}$
At surface S_4:	$u_r(r_i)=u_{r4}^*(r_i)\Leftrightarrow \frac{d\tilde{\varphi}_0(r_i)}{dr}+\frac{1}{r_i}\tilde{\psi}_{1,0}(r_i)=0$ $u_\theta(r_i)=u_{\theta 4}^*(r_i)\Leftrightarrow -\frac{1}{r_i}\tilde{\varphi}_0(r_i)-\frac{d\tilde{\psi}_{1,0}(r_i)}{dr}=0$
Requirements for the Potential Functions	
$\left(\Delta+\frac{\omega^2}{\alpha^2}\right)\tilde{\varphi}_0(r)\cos\theta=0\Leftrightarrow \frac{d^2\tilde{\varphi}_0(r)}{dr^2}+\frac{1}{r}\frac{d\tilde{\varphi}_0(r)}{dr}-\left(\frac{1}{r^2}-\frac{\omega^2}{\alpha^2}\right)\tilde{\varphi}_0(r)=0$ $\left(\Delta+\frac{\omega^2}{\beta^2}\right)\tilde{\psi}_{10}(r)\sin\theta=0\Leftrightarrow \frac{d^2\tilde{\psi}_{10}(r)}{dr^2}+\frac{1}{r}\frac{d\tilde{\psi}_{10}(r)}{dr}-\left(\frac{1}{r^2}-\frac{\omega^2}{\beta^2}\right)\tilde{\psi}_{10}(r)=0$	

Table 2-4: Overview of the solution scheme for the 2D elastodynamic case.

As presented earlier, the two equations in Table 2-4 are in the form of Bessel's equations in cylindrical coordinates. The general form of Bessel's differential equation in cylindrical coordinates is defined as

$$r^2\frac{d^2R}{dr^2}+r\frac{dR}{dr}-\left(n^2-r^2\right)R=0\Leftrightarrow \frac{d^2R}{dr^2}+\frac{1}{r}\frac{dR}{dr}-\left(\frac{n^2}{r^2}-1\right)R=0 \tag{2.79}$$

where n is an arbitrary real number. The solutions of this equation are called *Bessel* functions of order n. These functions are also known as cylinder functions or cylindrical harmonics, as they are associated with problems described for systems with polar or cylindrical symmetry. Since Bessel's equation in (2.79) is an ordinary differential equation of second order, the two functions expressing the solution are the Bessel function of the first kind $J_n(r)$ and Bessel function of the second kind $Y_n(r)$. A brief description of the main properties of the two functions is given in Appendix 9. The general solution generated by these is expressed as

$$R(r)=c_1J_n(r)+c_2Y_n(r) \quad \text{or} \quad R(r)=c_1J(n,r)+c_2Y(n,r) \tag{2.80}$$

with n being the order, r the argument and c_i the unknown constants. Comparing the two equations in Table 2-4 with the general form given by (2.79), it can be seen that order of the Bessel functions is n = 1. Furthermore, it is seen that the arguments in the two are $(\omega/\alpha)r$ for the first one and $(\omega/\beta)r$ for the second one. Thus, the general solutions of the two are

$$\tilde{\varphi}_0(r) = c_1 J\left(1, \frac{\omega}{\alpha} r\right) + c_1 Y\left(1, \frac{\omega}{\alpha} r\right) \quad ; \quad \tilde{\psi}_{1,0}(r) = c_3 J\left(1, \frac{\omega}{\beta} r\right) + c_4 Y\left(1, \frac{\omega}{\beta} r\right) \tag{2.81}$$

Consequently, the two solutions are given in terms of four constants, which is consistent with the four boundary conditions. Choosing $\omega/\alpha = A_1$ and $\omega/\beta = A_2$ in (2.81), the following displacement field is obtained

$$\begin{bmatrix} u_r(r,\theta) \\ u_\theta(r,\theta) \end{bmatrix} = \begin{bmatrix} \left(-c_1 A_1 J(1, A_1 r) - c_2 A_1 Y(1, A_1 r) + \frac{c_3}{r} J(0, A_2 r) + \frac{c_4}{r} Y(0, A_2 r)\right)\cos(\theta) \\ \left(c_3 A_2 J(1, A_2 r) + c_4 A_2 Y(1, A_2 r) - \frac{c_1}{r} J(0, A_1 r) - \frac{c_2}{r} Y(0, A_1 r)\right)\sin(\theta) \end{bmatrix} \tag{2.82}$$

The four unknown constants in (2.82) are easily obtained by applying the four boundary conditions given in Table 2-4. This is preformed in *Mathematica* as well, and the solutions can finally be compared to the ones obtained for the 2D elastostatic case, derived in the previous subsection. A full comparison of the displacements, strains and stresses is performed in the following section.

2.6 Comparison of 2D Elastostatic and 2D Elastodynamic Solutions

The key issue in this section is to evaluate the effect of introducing the dynamic source, by comparing the results with the exact 2D elastostatic case. This evaluation will verify whether or not the elastodynamic approach can be applied in the original three dimensional case, presented in Table 2-3. The input needed for this comparison is given in Table 2-5.

Geometry Input			**Grout Material Constants**			**Loading Input**	
L_G $[m]$	r_i $[m]$	r_o $[m]$	E_G $[GPa]$	ν	ρ $[kg/m^3]$	u_0 $[m]$	f $[Hz]$
7.10	2.35	2.44	70	0.19	2740	10^{-4}	10
The Boundary Conditions: $u_r(r_i) = 0, \quad u_\theta(r_i) = 0, \quad u_r(r_o) = -8u_0/\pi^2, \quad u_\theta(r_o) = 8u_0/\pi^2$							

Table 2-5: Data used for comparison.

The displacement provided in Table 2-5 is taken arbitrary here. As discussed earlier, the angular frequency cannot be set zero, but setting it to a very low value in stead does not violate the any conditions. Thus, the dynamic source of 10 *Hz* will be applied for comparison, which is assumed to more or less resemble the quasi-static behaviour considering the dimensions of the plane geometry given in Figure 2-6. However, it can be shown that much higher frequencies should be applied in order to see the effect of the dynamic disturbance at all. This is easily shown by considering the two wave speeds for the grout which are calculated to

$$\alpha = \sqrt{\frac{\lambda + 2\mu}{\rho}} = 5296 m/s \text{ and } \beta = \sqrt{\frac{\mu}{\rho}} = 3276 m/s \tag{2.83}$$

The wave length in terms of the two wave speeds can be expressed by means of wave number, which is the number of times a wave has the same phase. For the two wave speeds in (2.83), this is given as

$$k_\alpha = \frac{\omega}{\alpha} = \frac{2\pi f}{\alpha} \quad \text{and} \quad \beta = \frac{\omega}{\beta} = \frac{2\pi f}{\beta} \tag{2.84}$$

The wave length of the two different waves is expressed as

$$\lambda_\alpha = \frac{2\pi}{k_\alpha} = \frac{\alpha}{f} \quad \text{and} \quad \lambda_\beta = \frac{2\pi}{k_\beta} = \frac{\beta}{f} \tag{2.85}$$

Substituting the two wave speeds from (2.83) and the chosen frequency of 10 *Hz* into (2.85), it is found that

$$\lambda_\alpha = \frac{5296m/s}{10s^{-1}} \simeq 530m \quad \text{and} \quad \lambda_\beta = \frac{3276m/s}{10s^{-1}} \simeq 328m \tag{2.86}$$

Comparing the wave lengths in (2.86) with the thickness of the grout given in Table 2-5, i.e. $r_o - r_i = 0.09m$, it is seen that this is just an insignificant fraction of the two wave lengths. Consequently, choosing the frequency of $10Hz$ is very suitable to resemble a quasi-static case as this should be in the order of $5 \times 10^4 Hz$ and more in order to spot a nonlinear wave shape across the thickness of the grout.

Both the elastostatic system of equations, obtained in subsection 2.5.2 and the elastodynamic system, presented in subsection 2.5.3, are computed in Mathematica. A digital version of the mathematical codes is included on the CD attached in the back of this report. The results computed by these are reviewed in the following subsections.

2.6.1 Comparison of the Displacement Fields

For convenience, the displacement fields obtained for the two solution methods repeated. These are expressed via polynomial functions for the elastostatic case, and via Bessel functions for the elastodynamic case as show below.

Elastostatic:

$$\begin{bmatrix} u_r(r,\theta) \\ u_\theta(r,\theta) \end{bmatrix} = \begin{bmatrix} \left(-c_6 \frac{3\beta^2}{\alpha^2} r^2 + c_8 \frac{\beta^2}{\alpha^2} \ln(r) + c_8 \frac{\beta^2}{\alpha^2} + c_5 + c_6 r^2 + \frac{c_7}{r^2} + c_8 \ln(r)\right) \cos\theta \\ \left(c_6 \frac{\beta^2}{\alpha^2} r^2 - c_8 \frac{\beta^2}{\alpha^2} \ln(r) - c_5 - c_8 - 3c_6 r^2 + \frac{c_7}{r^2} - c_8 \ln(r)\right) \sin\theta \end{bmatrix}$$

Elastodynamic:

$$\begin{bmatrix} u_r(r,\theta) \\ u_\theta(r,\theta) \end{bmatrix} = \begin{bmatrix} \left(-c_1 A_1 J(1, A_1 r) - c_2 A_1 Y(1, A_1 r) + \frac{c_3}{r} J(0, A_2 r) + \frac{c_4}{r} Y(0, A_2 r)\right) \cos\theta \\ \left(c_3 A_2 J(1, A_2 r) + c_4 A_2 Y(1, A_2 r) - \frac{c_1}{r} J(0, A_1 r) - \frac{c_2}{r} Y(0, A_1 r)\right) \sin\theta \end{bmatrix}$$

The displacements at two points, $(r, \theta) = (2.38m, 0)$ and $(r, \theta) = (2.42m, 0)$, between the radial boundary distances r_i and r_o are compared in Table 2-6, noticing that these are scaled up for easier overview.

$f\ [s^{-1}]$	$u_r\ [mm]\ \times 10^6$		$u_\theta\ [mm] \times 10^6$	
	2D Dynamic	*2D Static (exact)*	*2D Dynamic*	*2D Static (exact)*
	$r = 2.38m,\ \theta = \pi/4$,			
10	-23.68	-23.68	24.35	24.35
	$r = 2.42m,\ \theta = \pi/4$			
	-55.09	-55.09	55.59	55.59

Table 2-6: Comparison of the displacements at two different points.

The results given in Table 2-6 indicate perfect conformity between the displacements. The two displacement components between the two boundaries, r_i and r_o, are plotted in Figure 2-7, where $\theta = \pi/4$.

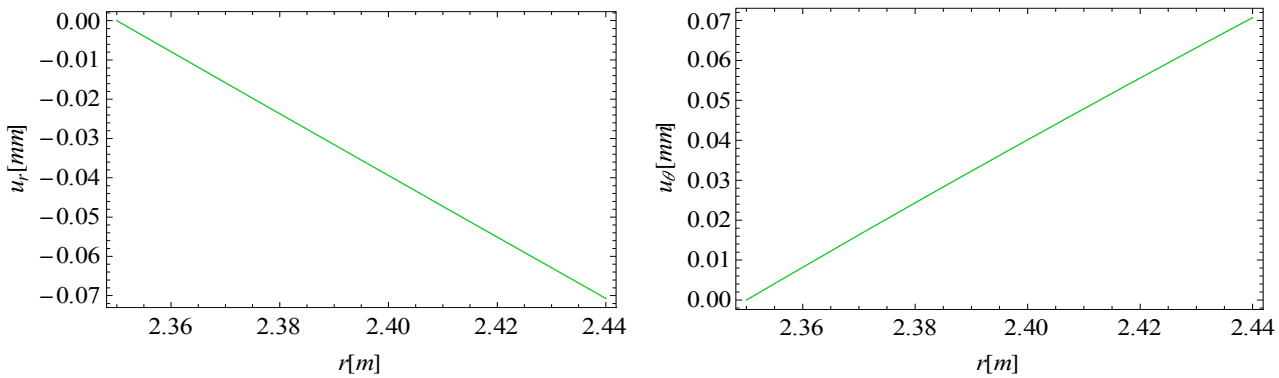

Figure 2-7: Displacement components with $f = 10Hz$ for elastostatic and elastodynamic cases.

The plots in Figure 2-7 clearly show that the dynamic effect of $10Hz$ in the elastodynamic solution is perfectly in accordance with the static solution across the entire thickness, as the two graphs are collinear. Consequently, this method seems applicable for both elastostatics and elastodynamics, provided that the geometry is small compared to the wave speeds of the given material. As the displacements are found to be in such excellent accordance, the strains and the stresses must be in accordance as well. These are presented in the following subsections.

2.6.2 Comparison of Strains

A brief overview of the strain components in cylindrical coordinates is shown below for convenience.

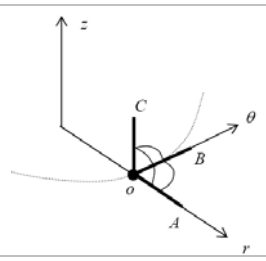

ε_{rr} = unit elongation of point oA
$\varepsilon_{\theta\theta}$ = unit elongation of point oB
ε_{zz} = unit elongation of point oC
$\varepsilon_{r\theta}$ = ½ change in angle $\angle\ AoB$
$\varepsilon_{\theta z}$ = ½ change in angle $\angle\ BoC$
ε_{zr} = ½ change in angle $\angle\ AoC$

The strain components are derived from the displacement components by means of the strain-displacement relations expressed by the Cauchy's strain tensor presented in section 2.1. These relations are summarized

for all six components in, both in Cartesian and cylindrical coordinates. As a perfect correspondence was found in comparison of the displacement components, the same is expected for the strains. The resulting strains computed for the data in Table 2-5 are reviewed in Table 2-7. The results are scaled up for convenience.

$f\ [s^{-1}]$	$\varepsilon_{rr} \times 10^5$		$\varepsilon_{\theta\theta} \times 10^5$		$\varepsilon_{r\theta} \times 10^5$	
	2D Dynamic	*2D Static*	*2D Dynamic*	*2D Static*	*2D Dynamic*	*2D Static*
	$r = 2.38m,\ \theta = \pi/4$					
10	-78.76	-78.76	0.028	0.028	79.81	79.81
	$r = 2.41m,\ \theta = \pi/4$					
	-78.25	-78.25	0.021	0.021	76.40	76.40

Table 2-7: The strains obtained at two points by the two methods.

The values in Table 2-7 show the apparent results. This additionally verifies the applicability of the utilized method. Nonetheless, the stresses must be verified as well. This is completed in the following.

2.6.3 Comparison of Stresses

The stresses are obtained by means of the constitutive relations expressed by Hooke's generalized law, as presented in section 2.1. Overview of general cylindrical stress components in 3D is illustrated below, while the explicit formulae in cylindrical coordinates are summarized in Appendix 5.

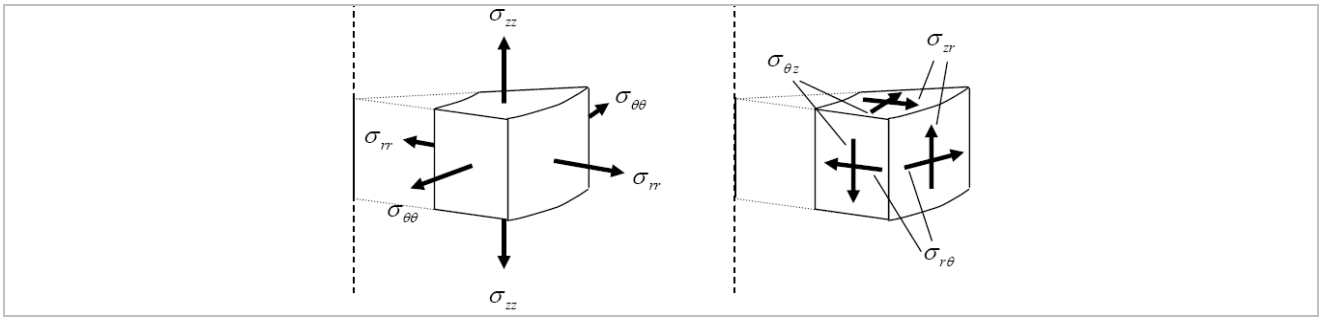

Since it was demonstrated that both the displacement and strain components are in conformity for the two methods, the linear constitutive relation suggests the same result for the stresses. The results obtained at the two points are given in Table 2-8.

$f\ [s^{-1}]$	$\sigma_{rr}\ [MPa]$		$\sigma_{\theta\theta}\ [MPa]$		$\sigma_{r\theta}\ [MPa]$	
	2D Dynamic	*2D Static*	*2D Dynamic*	*2D Static*	*2D Dynamic*	*2D Static*
	$r = 2.38m,\ \theta = \pi/4$					
10	-60.52	-60.52	-14.18	-14.18	46.95	46.95
	$r = 2.42m,\ \theta = \pi/4$					
	-60.13	-60.13	-14.09	-14.09	44.94	44.94

Table 2-8: The stresses obtained at the two points by the two methods.

As expected, Table 2-8 shows the excellent conformity between the stresses obtained by the two methods. For graphical overview, the three stress components are plotted between the radial boundaries of the grout as shown in Figure 2-8.

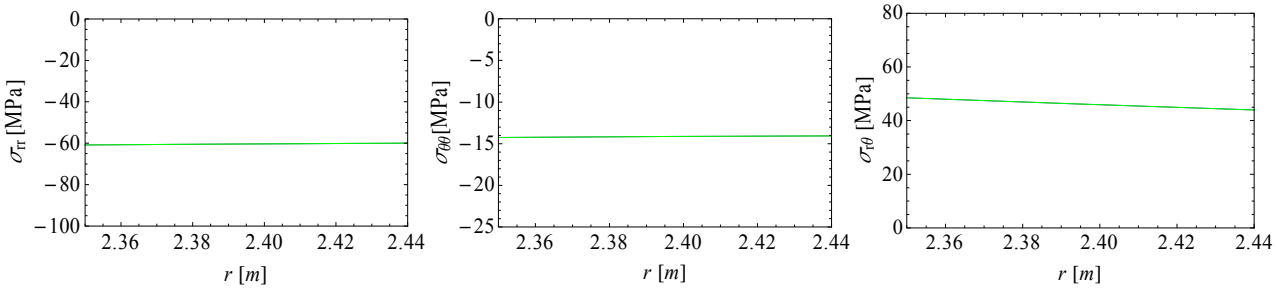

Figure 2-8: Stress components with $f = 10Hz$ for elastostatic and elastodynamic cases ($\sigma_{rr}, \sigma_{\theta\theta}, \sigma_{r\theta}$).

Figure 2-8 confirms the expected, i.e. the two graphs overlap. These results, together with the ones obtained in subsection 2.6.1 and 2.6.2, provide excellent confidence in the applicability of the model described by 2D elastodynamics in elastostatics. This encourages the fact that the same can be achieved in the 3D analysis. Consequently, the next step is to evaluate the results described by the 3D boundary value problem and subsequently compare the results at the boundaries considered in the 2D analysis. This is carried out in the following subsection.

2.7 3D Elastodynamic Solution

The full system of equations and boundary conditions for the 3D case has been presented in Table 2-3. As earlier discussed, this system contains three equations in form of Bessel's differential equation. Consequently, these can be solved similarly as done for 2D case in subsection 2.5.3, i.e. by means of Bessel functions. The three equations are all given in the following form

$$\frac{d^2R}{dr^2} + \frac{1}{r}\frac{dR}{dr} - \left(\frac{1}{r^2} + \frac{\pi^2}{L_G{}^2} - \frac{\omega^2}{\alpha^2}\right)R = 0 \tag{2.87}$$

Comparing the form in (2.87) with the general Bessel's equation given in (2.79), it is immediately seen that the order is $n = 1$ as in the 2D case, while the argument is now

$$\left(\sqrt{\frac{\omega^2}{\alpha^2} - \frac{\pi^2}{L_G{}^2}}\right)r \tag{2.88}$$

With the argument given in (2.88), the general solution of the three equations have the following form

$$\tilde{\varphi}_0(r) = c_1 J\left(1, \sqrt{\frac{\omega^2}{\alpha^2} - \frac{\pi^2}{L_G{}^2}} r\right) + c_1 Y\left(1, \sqrt{\frac{\omega^2}{\alpha^2} - \frac{\pi^2}{L_G{}^2}} r\right)$$
$$\tilde{\psi}_{1,0}(r) = c_3 J\left(1, \sqrt{\frac{\omega^2}{\alpha^2} - \frac{\pi^2}{L_G{}^2}} r\right) + c_4 Y\left(1, \sqrt{\frac{\omega^2}{\alpha^2} - \frac{\pi^2}{L_G{}^2}} r\right) \tag{2.89}$$
$$\tilde{\psi}_{2,0}(r) = c_5 J\left(1, \sqrt{\frac{\omega^2}{\alpha^2} - \frac{\pi^2}{L_G{}^2}} r\right) + c_6 Y\left(1, \sqrt{\frac{\omega^2}{\alpha^2} - \frac{\pi^2}{L_G{}^2}} r\right)$$

The solutions expressed in (2.89) to the three equations in the form given in (2.87) are next substituted into the three expressions for the displacement components given in Table 2-3. Subsequently, these are equated to the six boundary conditions, constituting a fully determinate system of six equations with six unknowns. The system is solved by Mathematica and the results are presented and compared to the exact elastostatic 2D case in the following subsection.

2.7.1 Comparison of Displacements, Strains and Stresses by 2D and 3D Solutions

The 3D displacement field has been evaluated the same two points as before, by calibrating the z-coordinate to the surface S_2 of the grout, i.e. $z = L_G/2$ in Figure 2-6, in order to obtain consistency with the 2D case. The displacements obtained by the 3D elastodynamic and the 2D elastostatic system are compared in Table 2-9.

f [s^{-1}]	u_r [mm] $\times 10^6$		u_θ [mm] $\times 10^6$	
	3D Dynamic	*2D Static (exact)*	*3D Dynamic*	*2D Static (exact)*
	$r = 2.38m,\ \theta = \pi/4$			
10	-24.46	-23.68	20.99	24.35
	$r = 2.42m,\ \theta = \pi/4$			
	-55.67	-55.09	53.02	55.59

Table 2-9: Comparison of the displacement components at two different points on boundary S_1.

Comparing the displacement components indicate more or less the same characteristics as before, with slightly larger difference between some of the values. Nevertheless, the results in Table 2-9 are acceptable as the tolerances involved are quite low. Next, the comparison of strains is given in Table 2-10.

f [s^{-1}]	ε_{rr} $\times 10^5$		$\varepsilon_{\theta\theta}$ $\times 10^5$		$\varepsilon_{r\theta}$ $\times 10^5$	
	3D Dynamic	*2D Static*	*3D Dynamic*	*2D Static*	*3D Dynamic*	*2D Static*
	$r = 2.38m,\ \theta = \pi/4$					
10	-79.99	-78.76	-0.15	0.03	74.51	79.81
	$r = 2.41m,\ \theta = \pi/4$					
	-76.12	-78.25	-0.11	0.02	85.82	76.40

Table 2-10: Comparison of the strains at two different points on boundary S_1.

The values in Table 2-10 illustrate acceptable conformity between the strain components on boundary surface S_1. The errors involved in these are slightly larger than those for the displacements in Table 2-9, which follows directly from the division involved in derivation. Finally, the comparison of the three stress components is given in Table 2-11.

f [s^{-1}]	σ_{rr} [MPa]		$\sigma_{\theta\theta}$ [MPa]		$\sigma_{r\theta}$ [MPa]	
	3D Dynamic	*2D Static*	*3D Dynamic*	*2D Static*	*3D Dynamic*	*2D Static*
	$r = 2.38m,\ \theta = \pi/4$					
10	-61.50	-60.52	-14.53	-14.18	43.83	46.95
	$r = 2.42m,\ \theta = \pi/4$					
	-58.52	-60.13	-13.81	-14.09	50.48	44.94

Table 2-11: Comparison of the stresses at two points on boundary surface S_1.

As before, the conformity of the strains leads to the same for the stress components. The graphical comparison of the stresses between the two boundaries is given in Figure 2-9.

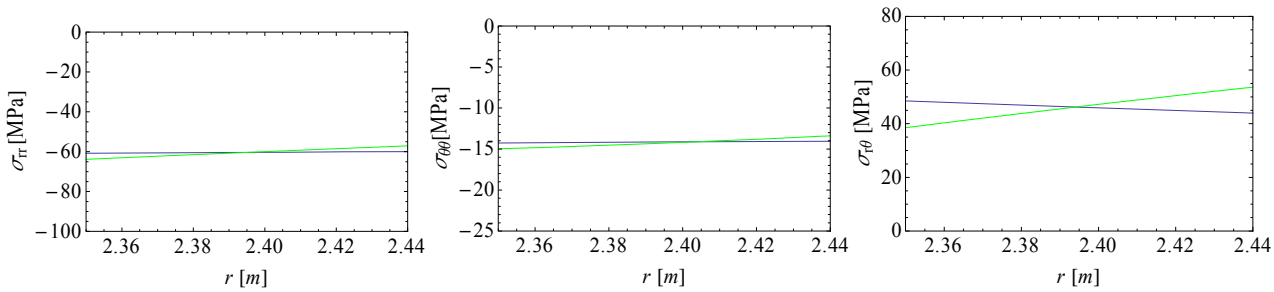

Figure 2-9: Stress components with $f = 10Hz$ for 2D elastostatic and 3D elastodynamic cases.

As seen on the plots of the three stress components in Figure 2-9, somewhat larger disagreement is obtained for the 3D solution, compared with the 2D static solution. However, it is emphasized that the plots may appear more divergent, which is why the numeric difference should be observed. Nevertheless the frequency of $10Hz$ resembles the quasi-static behaviour of the grout in the connection reasonably, taking the relatively large wave speeds into account. Furthermore, the stress distribution along the z-axis is shown in Figure 2-10.

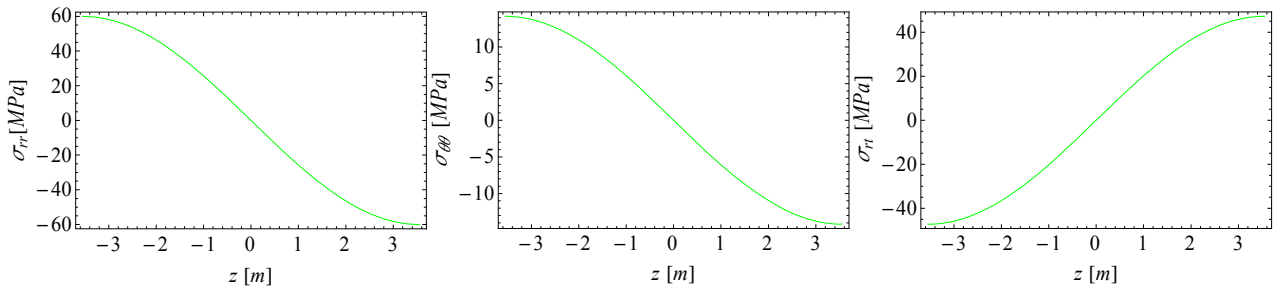

Figure 2-10: Stress components along z-axis for the 3D case with $f = 10Hz$ and $(r, \theta) = (2.4, \pi/4)$.

The graphs in Figure 2-10 illustrate the approximated distribution along z-axis, which approximately resembles the linear distribution of displacements, originally assumed in Figure 2-5 in subsection 2.4.3. Consequently, the conducted 3D elastodynamic solution method can be confirmed as a valid method for approximated solutions to the problems in elastostatics. However, in order to verify the obtained values it seems natural to evaluate the presented results by simple relations. This is done by considering a 1D situation, carried out in the following subsection.

2.7.2 1D Estimation of Maximum Stress in the Grouted Connection

The assumptions provided in Figure 2-6 in subsection 2.4.3, state that the largest displacements will occur at the top of the grout on one side and bottom of the other, due to the compression introduced by the force couple. This enables simple analysis of the grout to evaluate the maximum stress that may occur. This is done by considering the boundary surface S_1 as illustrated in Figure 2-11.

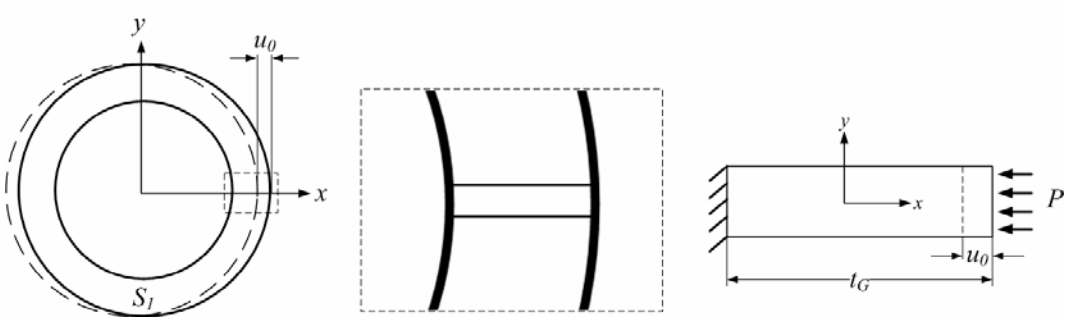

Figure 2-11: 1D idealization for maximum stress estimation.

As shown in the figure, the maximum stress can be approximately obtained by considering a small segment of the grout wall parallel to the applied force P, with the length corresponding to the thickness of the grout, i.e. $t_G = r_o - r_i$. It is assumed that the inner boundary is fixed and the maximum displacement resulting from the force P is taken as u_0, which produces the normal strain ε_{xx} along x-axis. This normal strain and the corresponding stress in the simple 1D case, assuming $\sigma_{yy} = \sigma_{zz} = 0$, are

$$\varepsilon_{xx} = \frac{u_0}{t_G} = \frac{-0.1mm}{90mm} = -0.00111 \quad ; \quad \sigma_{xx} = \varepsilon_{xx} E_G = -0.00111 \cdot 70 \cdot 10^3 MPa = -77.8MPa \tag{2.90}$$

The corresponding values from the advanced analyses are calculated at the point corresponding to the applied force in Figure 2-11, i.e. $(r, \theta, z) = (r_o, 0, L_G/2) = (2.44m, 0, 3.55m)$, noticing that $\sigma_{xx} = \sigma_{rr}$. The results are compared in Table 2-12 for the dynamic source $f = 10Hz$.

1D [MPa]	*2D Static [MPa]*	*2D Elastodynamic [MPa]*	*3D Elastodynamic [MPa]*
-77.8	-84.8	-84.8	-80.8

Table 2-12: Comparison of 1D, 2D and 3D results.

As shown in table Table 2-12, the compressive stress differs by approximately 7 MPa in 1D and 2D which is not quite negligible. However, considering the scope of idealization, it is essential to obtain a relation between the 1D simplified analysis that takes no Poisson effects into account, and a 1D case with Poisson effects, as these are embedded in the 2D and 3D analyses. This is done by advancing into a 3D formulation of the idealized 1D case, where $\varepsilon_{yy} = \varepsilon_{zz} = 0$. Considering a small cube being compresses along the *x*-axis implies that $\sigma_{yy} = \sigma_{zz}$, as the Poisson's ratio is valid in both directions. Utilizing this as well as Hooke's law, the normal strains along *y*- and *z*-axis are explicitly written as

$$\left.\begin{aligned} \frac{1}{E_G}\left(-\nu\sigma_{xx} + \sigma_{yy} - \nu\sigma_{yy}\right) = 0 \\ \frac{1}{E_G}\left(-\nu\sigma_{xx} - \nu\sigma_{yy} + \sigma_{yy}\right) = 0 \end{aligned}\right\} \nu\sigma_{xx} = \sigma_{yy}\left(1-\nu\right) \Leftrightarrow \sigma_{yy} = \frac{\nu\sigma_{xx}}{1-\nu} \Leftrightarrow \tag{2.91}$$

Thus, the relation between the two stresses in the case shown in Figure 2-11 is expressed in (2.91). Next, expressing the normal strain ε_{xx} explicitly by once more utilizing that $\sigma_{yy} = \sigma_{zz}$ and substituting (2.91), the following is obtained

$$\varepsilon_{xx} = \frac{1}{E_G}\left(\sigma_{xx} - \nu\sigma_{yy} - \nu\sigma_{yy}\right) \Rightarrow \varepsilon_{xx} = \frac{1}{E_G}\left(\sigma_{xx} - \frac{2\nu^2\sigma_{xx}}{1-\nu}\right) \tag{2.92}$$

Hence, the idealized unidirectional strain in (2.90) is expressed with the Poisson effects in (2.92). Isolating the normal stress σ_{xx} in (2.92) gives

$$\varepsilon_{xx}E_G = \sigma_{xx}\left(1 - \frac{2\nu^2}{1-\nu}\right) \Leftrightarrow \sigma_{xx} = \varepsilon_{xx}E_G\left(\frac{1-\nu}{1-\nu-2\nu^2}\right) \tag{2.93}$$

Consequently, the ratio of the normal stress expressed in the idealized case in (2.90) and the corresponding stress including Poisson effects, is given in the rightmost brackets in (2.93). Using the Poisson's ratio for grout being $\nu = 0.19$, the stress ratio becomes 1.098, such that $\sigma_{xx}(\text{2D or 3D}) = 1.098\sigma_{xx}(\text{1D})$. The results from Table 2-12 are now repeated in Table 2-13, where the 1D stress is multiplied by the obtained ratio.

1D [MPa]	*2D Static [MPa]*	*2D Elastodynamic [MPa]*	*3D Elastodynamic [MPa]*
-85.4	-84.8	-84.8	-80.8

Table 2-13: Comparison of 1D, 2D and 3D results.

Comparing the results in Table 2-13 clearly indicates that the stresses obtained by the advanced analyses fairly correspond to the value obtained by simple, but solid analysis. The stress obtained by the 3D solution involves the largest error, which is primarily caused by the one-term approximation of the displacement along *z*-axis, as introduced in equation (2.53). The difference is illustrated by the plots shown in Figure 2-12.

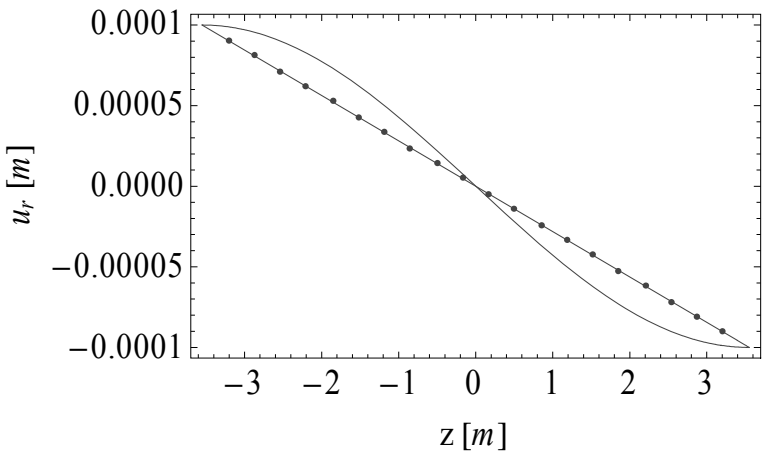

Figure 2-12: The assumed (dotted) and the approximated displacement distrubution along the grout length.

Finally, it has been demonstrated that the sequence of analyses involving approximated microscopic effects are carried out correctly and thereby must be valid in general. Prior concluding this chapter and considering numerical solutions it is convenient to round off by determining the stiffness of the grouted connection.

2.7.3 Estimation of Stiffness in the Grouted Connection

The total stiffness of the grouted connection can be easily derived by evaluating the loads acting on it. These, as well as a repeated overview of the connection, are illustrated in Figure 2-13.

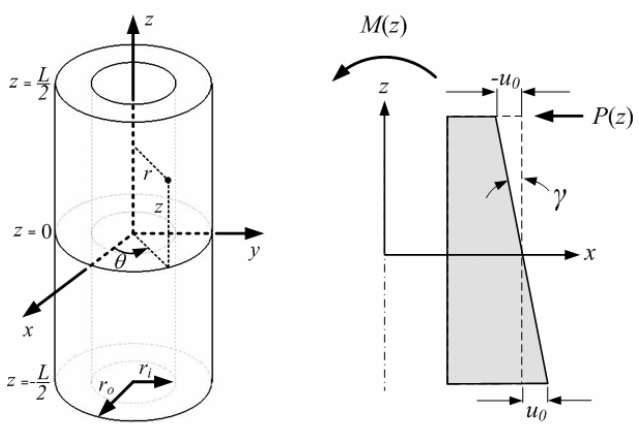

Figure 2-13:Overview of the grout subjected to loading.

With the known stresses, the force and moment distributions are obtained by simple integration. The resultant force $P(z)$ can be expressed along the connection length in 3D as

$$P(z) = \int_0^{2\pi} \left(\sigma_{rr}(r,\theta,z)\cos\theta - \sigma_{r\theta}(r,\theta,z)\sin\theta \right) r d\theta \tag{2.94}$$

Sepparating the variables for the two stress components, the integral in (2.94) can be expressed as

$$\begin{aligned} P(z) &= \int_0^{2\pi}\left(\left(\tilde{\sigma}_{rr}(r)\cos\theta\sin\frac{\pi z}{L_G}\right)\cos\theta-\left(\tilde{\sigma}_{r\theta}(r)\sin\theta\sin\frac{\pi z}{L_G}\right)\sin\theta\right)rd\theta \\ &= \int_0^{2\pi}\left(\tilde{\sigma}_{rr}(r)\cos^2\theta-\tilde{\sigma}_{r\theta}(r)\sin^2\theta\right)rd\theta\sin\frac{\pi z}{L_G} \\ &= \left(\pi r_o\tilde{\sigma}_{rr}(r_o)-\pi r_o\tilde{\sigma}_{r\theta}(r_o)\right)\sin\frac{\pi z}{L_G}\ \left[N/m\right] \end{aligned} \tag{2.95}$$

Hence, knowing the two stress components at the radial distance r_o, the force distribution along the z-axis can be obtained by (2.95). In order to obtain the rotational stiffness of the structure along this axis, i.e. deformation resistance due to bending, it is essential to obtain the maximum moment distribution along this axis. This is done by the following integration

$$\begin{aligned} M &= \int_{-L_G/2}^{L_G/2} P(z)\cdot z\cdot dz = \left(\pi r_o\tilde{\sigma}_{rr}(r_o)-\pi r_o\tilde{\sigma}_{r\theta}(r_o)\right)\int_{-L_G/2}^{L_G/2}\sin\frac{\pi z}{L_G}\cdot z\cdot dz \\ &= \left(\pi r_o\tilde{\sigma}_{rr}(r_o)-\pi r_o\tilde{\sigma}_{r\theta}(r_o)\right)\frac{2L_G^{\ 2}}{\pi^2}\ \left[Nm\right] \end{aligned} \tag{2.96}$$

By defining the angle of rotation shown in Figure 2-13 as $\gamma=\arctan\left(2u_0/L_G\right)$, the rotational stiffness k of the connection is finally expressed as

$$k=\frac{|M|}{\gamma}=\left|\frac{\left(r\tilde{\sigma}_{rr}(r_o)-r\tilde{\sigma}_{r\theta}(r_o)\right)2L_G^{\ 2}}{\arctan\left(2u_0/L_G\right)\pi}\right|\ \left[Nm/\deg\right] \tag{2.97}$$

For the dimensions and the displacement given in Table 2-5, the angle of rotation is

$$\gamma=\arctan\left(2\cdot 0.0001m/7.1m\right)=0.0016\deg$$

The shear stress is maximum at $\theta=\pi/2$ giving $\tilde{\sigma}_{r\theta}(r_o,\pi/2)=61.48MPa$, which should in principle be the same as $\tilde{\sigma}_{rr}(r_o,0)$ due to the rigid body motion assumption. The maximum radial stress is found at $\tilde{\sigma}_{rr}(r_o,0)$ and given in Table 2-13 for the 3D elastodynamic case. A slight difference is found due to the applied approximations. With these values, the rotational stiffness becomes

$$|k|=\frac{2.44m\cdot(-80.75-75.85)\cdot 10^6\,N/m^2\cdot 2\cdot 7.1^2m^2}{0.0016\deg\cdot\pi}\simeq 7.7\cdot 10^{12}\left[Nm/\deg\right]$$

As can be seen, the stiffness of the structure is found extremely high. This implies that the overall deformation of the entire monopile foundation structure due to bending is primarily caused by the flexibility of the two steel pipes. The portion of the foundation containing the grouted connection is thereby expected to behave much more rigidly, such that it resides more or less straight during bending. However, the obtained

stiffness is calculated for the assumed deformation of the grout, i.e. $u_0 = 0.1mm$, as are the results presented in the subsections 2.6.1 to 2.7.1.

An analytical model that realistically estimates this deformation is not the subject of this work, however, it is presumed that this can be done quite satisfactorily. Alternatively, experimental methods could contribute with some characteristics, but should preferably be preformed on the full scale structure. Another alternative is to address the entire problem by FEM. Basic FE methodology and an analysis of the simplified model of the grouted connection is elaborated in the next chapter.

Chapter 3

3. Finite Element Analysis of the Grouted Connection

The complexity of the structural behaviour of the grouted connection has been outlined in several contexts throughout this text. As a result, the general issues to be addressed in the Finite Element model would be the following

- Contact behaviour of the interface between grout and steel
- The nonlinear material behaviour of the grout
- Choice of element types and discretization

It is emphasized that several FE analyses of similar connections have been performed and documented in different literature, e.g. [Andersen and Petersen, 2004], where the horizontal loading has been addressed. In their assessment, the focus was directed to the nonlinear contact formulations concerning friction and penetration, as well as use of nonlinear constitutive models for the grout. Furthermore, their FE model is compared to and verified by a scaled experimental model. For this reason, no extensive analysis of the complete structure will be performed, as some of their results will be used as a reference.
The objective in this chapter is to analyse the grouted connection to confirm the results obtained in the simplified analysis conducted in the previous chapter. Consequently, the construction of the model to be analysed will be done in accordance with the assumptions and restrictions elaborated for the analytical analyses. Subsequently, this model will be briefly compared to the model considered in [Andersen and Petersen, 2004] as a secondary objective. Prior elaborating these steps, some basic aspects of the FEM, particularly with respect to static structural analyses, is given in the following section. All Computer Aided Design (CAD) and numerical analyses presented in this chapter are preformed in the FE analysis program ANSYS and ANSYS Workbench.

3.1 Basics of FEM

In the previous chapter, the grout in the connection is treated as a continuum, which implies infinite number of degrees of freedom (DOF). FEM is a numerical solution method, which approximates the infinite number

of DOF in a mechanical system to a finite number, in order to be practical. This reduction is obtained by discretization, such that a discrete model of grout is treated. In general, the discretization involves both the space and time dimensions. However, in this context it is chosen to omit the time dimension and assume a fully static structural problem, in which the state of equilibrium and the spatial discretization are the only concerns. Prior a mathematical formulation of such tasks, it is essential to introduce some basic characteristics of FEM. A simplified visualization of the role of FEM in a numerical simulation is illustrated in Figure 3-1.

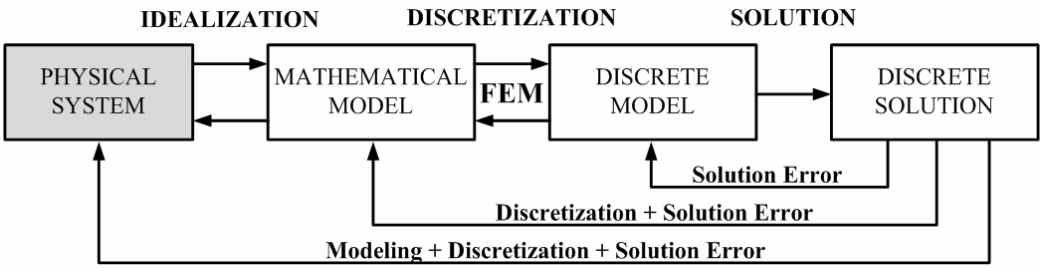

Figure 3-1: Simplified overview of the physical simulation process [Felippa, 2009].

Figure 3-1 does not directly illustrate how FEM is used, but rather the basic flow of a numerical simulation containing FEM as a sub-step, as well as the errors involved in each step from idealization through discretization to a solution. For instance, a discrete solution contains both modelling, discretization and solution errors. In principle, the analytical solution elaborated in Chapter 2 involves solely modelling errors. This demonstrates one the most important advantages in seeking generalized analytical solutions, which is attempted in Chapter 2. However, the inferiority of modelling errors in the analytical solution must be weighted with respect to the primitivism of the modelling assumptions. As the idealization process is always done by a human, this implies that wrong abstractions of the physical model directly lead to wrong results. This implies that idealization, i.e. modelling errors, is the most important step in the simulation process. The only reasonable way to evaluate the modelling errors is by experimental methods.

The discretization error is a secondary error source. This is obtained when substituting the discrete solution into the original mathematical model, for which the closed form, i.e. exact, solution is known. The solution of the discrete model with finite number of DOF is thereby only an approximation of the exact solution. The solution errors are usually small and thus ignored, as they are generally calibrated to an acceptable tolerance.

The step containing FEM is basically conducted in four overall steps involving the following, based on [Cook et.al., 2002] and [Lund, 2007].

Discretization:

The structure is created and discretized into finite elements, i.e., subdivided into nodes and elements. Either 1D, 2D or 3D elements are used. The elements are interconnected at their exterior nodes, thus approximately

composing the entire domain of the structure. The main concern in this relation is to decide how many nodes are needed, what type of elements should be used and how the boundary conditions should be imposed.

Choice of Interpolation Functions:

The interpolation functions represent the physical behaviour over an element by interpolating the nodal solution across the entire element, which is also the main reason for the approximate nature of the solution. They are formulated to satisfy the prescribed nodal values of a given quantity, usually nodal displacements of an element. The main concern is whether these are satisfactory as simple linear- or more accurate nonlinear functions, usually in form of polynomials.

Formulation of Governing Equations:

Formulation of approximate solution of the governing field equations must be obtained. Analysis tools like virtual work- and variational arguments are generally adequate for FE formulation of most problems in structural mechanics. Raleygh-Ritz variational method, see [Cook et.al., 2002, Chapter 4], or weighted residual methods like Galerkin method, see [Cook et.al., 2002, Chapter 5], can be used.

Solution:

Simultaneous solution of the system of equations by direct integration or iterative methods is preformed to obtain the element stiffness matrix, which relates the element results, e.g. nodal displacements with nodal forces. The global stiffness matrix is constructed by assembling the element nodal results to represent the entire problem. Using the nodal solutions, other information e.g. stresses and strains can be obtained straightforwardly.

The major steps characterizing the FEM are outlined above. Thus, after discretization of the physical system into elements, the solution is approximated over each element and quantified in terms of values at the element nodes. An overview of typical element geometries used in FEM is illustrated in Figure 3-2.

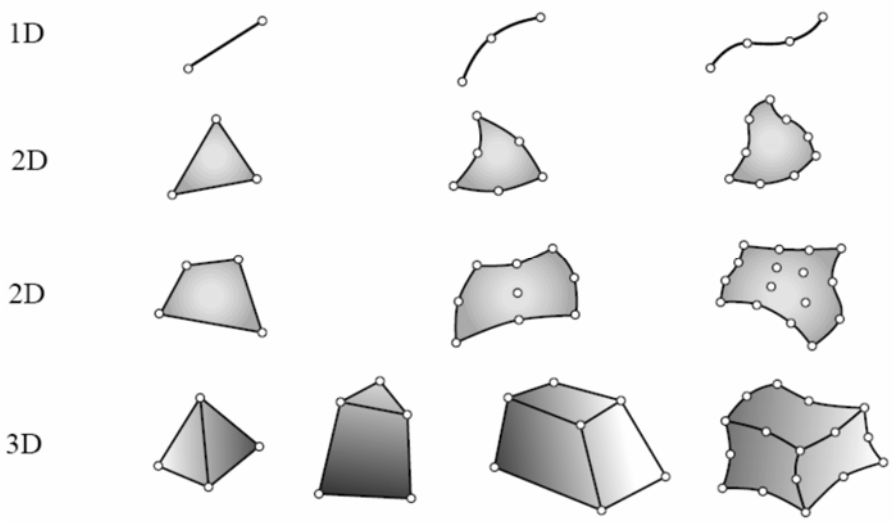

Figure 3-2: Finite element geometries in different dimensions [Felippa, 2009].

As shown in Figure 3-2, nodes are typically located at the corners or end points of elements. However, it is possible to include the nodes on sides or faces of the elements, which leads to higher-order elements exhibiting e.g. quadratic displacement behaviour. Furthermore, nodes serve both to define the geometry of the element, but also to define the number of DOF, as each node has six DOF, i.e. three translations and three rotations.

During discretization, an algebraic system of equations for the unknown nodal values is established to approximate the continuous solution. As the element size, geometry, and interpolation formulation can be adjusted to the specific problem, the FEM can simulate solutions to problems involving complex geometries and loadings very accurately. Therefore, the FEM has become one of the most effective engineering tools for practical stress analysis, but also to assist in many other fields of science. In the following section, a mathematical system of equations applying to static structural FE analyses is formulated.

3.2 Static Structural FE Analysis

The general steps in a FEM are introduced in the previous section. As described, the basic formulation of the FEM involves the development of the element equation that approximately represents the elastic behaviour of the element. Obtaining this in general allows for utilizing it for all elements in the discretized model. In section 3.1, two different methods that provide a scheme to develop approximate solutions to elasticity problems are pointed out. One of the methods is based on the *Rayleigh-Ritz method*, after the Swiss mathematical physicist Walter Ritz (1878-1909) and the English physicist John William Strutt, Lord Rayleigh (1842-1919). A detailed elaboration of this method is found in e.g. Section 4.5 in [Cook et.al., 2002]. In brief, the method is a procedure for determining parameters in an approximating field, which lead to an extremum of a given function of the field. The approximating field in structural analysis is composed of several functions, all of which satisfy the essential kinematic boundary conditions and are each associated with a single DOF. This method is found useful for eigenvalue- and equilibrium problems. As the static structural problem is essentially an equilibrium problem, it is convenient to produce FE approximations using this method.

In order to apply this method, it is required to have a functional, which in this context is an integral expression that implicitly contains the governing differential equations for a particular problem [Cook et.al., 2002]. A very useful functional is in this case that for total potential energy Π_p, which contains integrals that span the entire domain of a problem. This implies, though, that the functional is in *weak form*. To understand this term in a structural problem, it is convenient to introduce the *strong form*. In this context, the governing differential equations including the boundary conditions are, by definition, stated in strong form. Oppositely, integral expressions, such as a functionals, implicitly contain the differential equations and are referred to as in weak form. Hence, both are forms of differential equations, where the weak form involves conditions that must be met only in an integral sense, while these must be satisfied at every point in a material when in strong form. Nevertheless, both forms are equally valid for a given problem.

Prior elaborating the use of the total potential energy functional in FEM, it is assumed that the structural system under consideration is *conservative*. This implies that the work done by the internal forces and work done by external forces is equal in magnitude to the change in strain energy [Cook et.al., 2002]. Thus, the potential energy of a conservative system can be expressed in terms of its initial and final configurations. If U represents the internal strain energy of the system and Ω the external work done on the body by the applied forces, i.e. the potential of the applied loads, the total potential energy of a linearly elastic structure can be expressed by summing the two as

$$\Pi_p = U + \Omega \tag{3.1}$$

The necessary energy to deform a unit volume of the material in the structure is given by

$$U_0 = \int \{\sigma\}^T \{d\varepsilon\} = \frac{1}{2}\{\sigma\}^T \{\varepsilon\} = \frac{1}{2}\{\varepsilon\}^T \{\sigma\} \tag{3.2}$$

where the total strain energy contained in the structure for its entire volume is defined as:

$$U = \int_V U_0 dV \tag{3.3}$$

It is noted that { } and [ ] in this derivation represent a column vector and a rectangular or square matrix, respectively. In the case of an elastic material, the energy U_0 stored during deformation can be recovered once the force causing the deformation is removed. In such case U_0 is known as the elastic strain energy density [Cook et.al., 2002]. With $[E]$ being the constitutive matrix in linear elasticity and $\{\varepsilon\}$ the vector containing strain components, the stresses are expressed as

$$\{\sigma\} = [E]\{\varepsilon\} \tag{3.4}$$

In the case of a linear elastic material subjected to initial stresses σ_0 and initial strains ε_0 equation (3.4) takes the following form

$$\{\sigma\} = [E](\{\varepsilon\} - \{\varepsilon_0\}) + \{\sigma_0\} \tag{3.5}$$

By inserting (3.5) into (3.2) and integrating, the following expression is obtained

$$U_0 = \frac{1}{2}\{\varepsilon\}^T [E]\{\varepsilon\} - \{\varepsilon\}^T [E]\{\varepsilon_0\} + \{\varepsilon\}^T \{\sigma\} \tag{3.6}$$

Equation (3.6) describes the deformation energy per unit of volume. To obtain the total strain energy of the structure, the expression is integrated over the volume giving

$$U = \int U_0 dV = \int \left(\frac{1}{2} \{\varepsilon\}^T [E] \{\varepsilon\} - \{\varepsilon\}^T [E] \{\varepsilon_0\} + \{\varepsilon\}^T \{\sigma\} \right) dV \tag{3.7}$$

The potential of Ω is based on the loads applied to the structure. This can be split into volumetric loads, surface loads and point loads. Volumetric loads and the displacements produced by them are denoted as

$$\{F\} = \begin{Bmatrix} F_x \\ F_y \\ F_z \end{Bmatrix} \qquad \{u\} = \begin{Bmatrix} u \\ v \\ w \end{Bmatrix} \tag{3.8}$$

where the column vectors $\{F\}$ and $\{u\}$ in (3.8) represent the load and displacement vector, respectively. The potential for work lost by the force applied upon an infinitesimal unit of volume dV can now be expressed as

$$d\Omega_V = -\{u\}^T \{F\} dV \tag{3.9}$$

It is noted that the negative sign in (3.9) corresponds to a lost potential. Now integrating expression (3.9) over the total volume, the work done by all the volumetric loads can be obtained by

$$\Omega_V = -\int_V \{u\}^T \{F\} dV \tag{3.10}$$

Applying the same method to point and surface loads the following two equations are obtained

$$\Omega_S = -\int_S \{u\}^T \{T\} dS \tag{3.11}$$

$$\Omega_P = -\{D\}^T \{P\} \tag{3.12}$$

where $\{T\}$ are the surface tractions, $\{D\}$ is the global vector of DOF for the whole structure and $\{P\}$ are the concentrated forces applied to the structure. Equation (3.12) accounts for the work done and thereby the potential lost by the applied concentrated forces and/or moments. The sum of equations (3.10), (3.11) and (3.12) yields the total potential of the applied loads as

$$\Omega = \Omega_V + \Omega_P + \Omega_S \tag{3.13}$$

The total elastic potential as expressed in (3.1) is the sum of (3.13) and (3.7) which gives

$$\Pi_p = \int_V \left(\frac{1}{2} \{\varepsilon\}^T [E] \{\varepsilon\} - \{\varepsilon\}^T [E] \{\varepsilon_0\} + \{\varepsilon\}^T \{\sigma\} \right) dV - \int_V \{u\}^T \{F\} dV - \int_S \{u\}^T \{T\} dS - \{D\}^T \{P\} \tag{3.14}$$

For a linear elastic system with infinite DOF, the functional for the total elastic potential can be expressed as [Mouritsen, 2004]

$$\Pi_p = \Pi_p\left(\{D\}\right) = f\left(\frac{\partial\{u\}}{\partial x}, \frac{\partial\{u\}}{\partial y}, \frac{\partial\{u\}}{\partial z}, \{u\}\right) \tag{3.15}$$

Consequently, the total elastic potential is expressed as a functional which is a function of the entire set of DOF, i.e. $\{D\}$, but written alone for simplicity. Recalling the earlier definition and considering (3.15) as an exact field with infinite number of DOF, it is necessary to obtain the implicit parameters in the functional which yield extremum of the functional *f*. Thus, the elastic structure described by the functional given in (3.15) will achieve static equilibrium for the minimum value of Π_p, which is the case when

$$\left\{\frac{\partial \Pi_p}{\partial\{D\}}\right\} = \{0\} \tag{3.16}$$

The method that requires the condition in (3.16) is known as the principle of stationary, or minimum, potential energy which states that [Cook et.al., 2002]

Out of all geometrically possible displacement functions $u(x, y, z) = \{u\}$ *the one which minimizes the total potential energy,* Π_p*, in a conservative system is the displacement solution that will both satisfy equilibrium and will be the actual displacement due to the applied forces.*

Thus, a displacement function that will minimize the functional, Π_p, is desired. In far most cases an exact function that is impossible to determine for the system of infinite number of DOF. Therefore the structure must be approximated into a finite number of DOF. This is exactly where the Rayleigh-Ritz method comes into consideration, as it provides a way to approximate all displacement nodes of a system with infinite DOF $\{u\}$ with a finite subset $\{\tilde{u}\}$. Substituting this subset into equation (3.15) gives

$$\tilde{\Pi}_p = f\left(\frac{\partial\{\tilde{u}\}}{\partial x}, \frac{\partial\{\tilde{u}\}}{\partial y}, \frac{\partial\{\tilde{u}\}}{\partial z}, \{\tilde{u}\}\right) \tag{3.17}$$

By using a mere approximation of (3.15), an exact solution will not be possible in the majority of cases. However, the obtained solution will converge towards the exact value of the total elastic potential minimum with an error that depends on the number of DOF of the model. In a FE analysis of a structure the elastic potential is formulated for each element. The total elastic potential is obtained as the sum of each element's elastic potential and with n_e denoting the number of elements considered this is expressed as follows

$$\begin{aligned}\tilde{\Pi}_p = &\sum_{i=1}^{n_e}\int_V\left(\frac{1}{2}\{\varepsilon\}_i^T[E]_i\{\varepsilon\}_i - \{\varepsilon\}_i^T[E]_i\{\varepsilon_0\}_i + \{\varepsilon\}_i^T\{\sigma_0\}_i\right)dV \\ &-\sum_{i=1}^{n_e}\int_V\{u\}_i^T\{F\}_i dV - \sum_{i=1}^{n_e}\int_S\{u\}_i^T\{T\}_i dS - \{D\}^T\{P\}\end{aligned} \tag{3.18}$$

In general the initial stresses and strains are not present, such that equation (3.18) reduces to

$$\tilde{\Pi}_p = \sum_{i=1}^{n_e} \int_V \frac{1}{2} \{\varepsilon\}_i^T [E]_i \{\varepsilon\}_i dV - \sum_{i=1}^{n_e} \int_V \{u\}_i^T \{F\}_i dV - \sum_{i=1}^{n_e} \int_S \{u\}_i^T \{T\}_i dS - \{D\}^T \{P\} \tag{3.19}$$

Equation (3.19) can be solved by utilizing the fact that the displacements $\{\tilde{u}\}_i$ within an element i can be interpolated from the element nodal displacements by means of the element shape functions as follows

$$\{\tilde{u}\}_i = [N]_i \{d\}_i \tag{3.20}$$

Where $[N]$ is the shape matrix containing the shape functions N_i and $\{d\}_i$ is the nodal DOF vector. For a detailed description of general construction of shape functions, the reference is given to e.g. [Lund, 2007]. The strains can be found by derivation of displacements as

$$\{\tilde{\varepsilon}\}_i = [\partial]\{\tilde{u}\}_i \Rightarrow \{\tilde{\varepsilon}\}_i = [B]_i \{d\}_i \quad \text{where} \quad [B]_i = [\partial][N]_i \tag{3.21}$$

The matrix $[B]_i$ in equation (3.21) represents the strain-displacement matrix that transforms nodal displacements to strains at any point in the element, and $[\partial]$ is the matrix of differential operators that converts the displacement to strains [Mouritsen, 2004]. In 3D linear elasticity theory, this is defined as

$$[\partial] = \begin{bmatrix} \frac{\partial}{\partial x} & 0 & 0 & \frac{\partial}{\partial y} & 0 & \frac{\partial}{\partial z} \\ 0 & \frac{\partial}{\partial y} & 0 & \frac{\partial}{\partial x} & \frac{\partial}{\partial z} & 0 \\ 0 & 0 & \frac{\partial}{\partial z} & 0 & \frac{\partial}{\partial y} & \frac{\partial}{\partial x} \end{bmatrix}^T \tag{3.22}$$

By substituting (3.20) and (3.21) in (3.19) the following is found

$$\tilde{\Pi}_p = \frac{1}{2} \sum_{i=1}^{n_e} \{d\}_i^T [k]_i \{d\}_i - \sum_{i=1}^{n_e} \{d\}_i^T \{r_e\}_i - \{D\}^T \{P\} \tag{3.23}$$

where the stiffness matrix $[k]_i$ of element i is defined as

$$[k]_i = \int_V [B]_i^T [E]_i [B]_i dV \tag{3.24}$$

and $\{r_e\}_i$ is the consistent node load vector composed of both the volumetric- and surface loads, defined as

$$\{r_e\} = \int_V [N]^T [F] dV + \int_S [N]^T [T] dS \tag{3.25}$$

Alternatively, if initial stresses or strains are present, these should be included in the node load vector in (3.25). The stationary state of Π_p in (3.16) must be found for the global DOF vector $\{D\}$. Therefore the local

DOF $\{d\}_i$ must be substituted in (3.23). The set of global DOF $\{D\}$ and the local subset $\{d\}_i$ are related by the following expression

$$\{d\}_i = [L]_i \{D\} \tag{3.26}$$

The matrix $[L]_i$ is an $m_i \times m$ matrix where m_i is the number of DOF in an element i and m is the total number of DOF. The matrix $[L]_i$ is composed exclusively by ones and zeroes. Next, substituting (3.26) in (3.23) and applying common matrix operations gives

$$\tilde{\Pi}_p = \frac{1}{2}\{D\}^T \left(\sum_{i=1}^{n_e} [L]_i^T [k]_i [L]_i \right) \{D\} - \{D\}^T \left(\sum_{i=1}^{n_e} [L]_i^T \{r_e\}_i + \{P\} \right) \tag{3.27}$$

Next, it is possible to assemble the local stiffness matrices $[k]_i$ into a global stiffness matrix $[K]$ as shown in equation (3.28)

$$[K] = \sum_{i=1}^{n_e} [L]_i^T [k]_i [L]_i \tag{3.28}$$

Furthermore, it is possible to assemble the local node loads $\{r_e\}_i$ and point loads $\{P\}$ into a single load vector $\{R\}$ by the following relation [Mouritsen, 2004]

$$\{R\} = \{R_e\} + \{P\} = \sum_{i=1}^{n_e} [L]_i^T \{r_e\}_i + \{P\} \tag{3.29}$$

By substituting (3.28) and (3.29) into (3.27), the following reduced expression is obtained

$$\tilde{\Pi}_p = \frac{1}{2}\{D\}^T [K] \{D\} - \{D\}^T \{R\} \tag{3.30}$$

Finally, to achieve static equilibrium it is necessary to minimize the potential energy in (3.30). As discussed earlier, this can be done by applying the principle of stationary potential energy as expressed in (3.16). Hereby the following system of equations can be deduced

$$\left\{ \frac{\partial \tilde{\Pi}_p}{\partial \{D\}} \right\} = \{0\} \quad \Leftrightarrow \quad [K]\{D\} - \{R\} = 0 \quad \Leftrightarrow \quad \{R\} = [K]\{D\} \tag{3.31}$$

The system of equations in (3.31) will describe the continuum of a body with the global reaction forces and displacements as the unknowns, as long as there is no rigid body movement. In literature, this system is also referred to as *master stiffness equations*. Consequently, a continuous system with infinite number of DOF is reduced to a discrete system containing a model with a finite number of DOF, matching the global number of DOF $\{D\}$. Furthermore, it is shown that an FE formulation can basically be expressed by a single functional that and a formulation of the nodal interpolation in the elements. Ultimately, the quality of the system containing the discrete model is solely dependent on how well the displacement functions in this model, ex-

pressed by the shape matrix as $\{\tilde{u}\}_i = [N]_i \{d\}_i$, describe the displacement field in the real physical system [Mouritsen, 2004]. In FE computer programs the system of equations in (3.31) are directly developed during the pre-processing, such that the total elastic potential in (3.30) is not used at all [Cook et.al., 2002].

Using FEM in practice involves many other important considerations, such as definitions of different elements for different problems, as well as different boundary and loading conditions that may exist in the physical system. For this reason, several problem specific issues will be discussed when appropriate in the modelling, discretization and solution steps. However, the boundary conditions can be described more generally and a brief overview is given in the next section.

3.3 Boundary Conditions in Structural Problems

As discussed in section 2.2, the fundamental boundary conditions in mechanical problems are either traction- or displacement based. It was demonstrated in the previous section that FEM is essentially a displacement formulation. Some of the basic displacement BCs are described in the following [Felippa, 2009]

Ground or Support Constraints:

Such constraints directly permit the structure to exhibit rigid body motions.

Symmetry Conditions:

To impose symmetry or anti-symmetry restraints at certain points, lines or planes of structural symmetry. This allows the discretization to proceed only over part of the structure with a consequent savings in modelling effort and number of equations to be solved. An example of symmetry B.C. is illustrated in Figure 3-3.

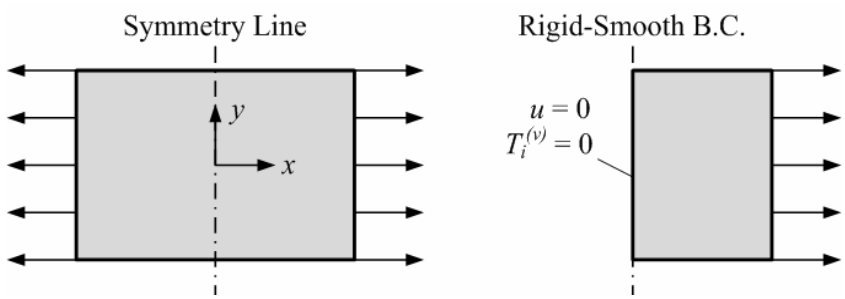

Figure 3-3: Symmetry boundary conditons.

Connection constraints:

These are used to provide connectivity to interconnected structures or substructures, or to specify relations between degrees of freedom. Many conditions of this type can be described as *multipoint constraints* (MPCs). As opposed to single-point constraints (SPC), which are defined as prescribed constraints acting on individual nodes, i.e. DOF, the MPCs involve prescribed constraints that act on several nodes simultaneously. Mathematical examples of the SPCs and MPCs are given below [Felippa, 2009].

SPC:

- Nodal displacement component = Prescribed value
- Example: $u_{x1} - \frac{1}{2}u_{y1} + 2u_{z1} = 0$, which is linear and homogeneous SPC, as it involving displacement components of node 1 solely

MPC:

- $f\left(\text{Nodal displacement components}\right)$ = Prescribed value
- Example 1: $u_{x1} - \frac{1}{2}u_{x2} + 2u_{x3} = 1$, which is a linear and inhomogeneous MPC, as it involves three nodes, 1, 3 and 3
- Example 2: $\left(x_1 + u_{x1} - x_2 - u_{x2}\right)^2 + \left(y_1 + u_{y1} - y_2 - u_{y2}\right)^2 = 0$, which is a nonlinear and homogeneous MPC, which geometrically expresses that the distance between nodes 1 and 2 in *xy*-plane remains constant.

In the above definition of MPCs, *f* is a functional which vanishes only if all spatial arguments of the nodal displacements vanish as well. All above examples are given for equality constraints. However, in nonlinear contact problems it is often more convenient to express inequality MPCs, which control e.g. the relative sliding or gap opening between two contact surfaces. An introduction to contact problems is given in subsection 3.3.1, where the MPC formulation in FE analyses is described as well.

3.3.1 Contact Problems in General

A contact problem is said to be nonlinear as the BCs become a function of the load intensity, i.e. nonlinear kinematic condition [Lund, 2008]. In general, this type of problems is considered when two nodes or surfaces of the same or two different structures either come into contact, separate or exhibit frictional sliding relative to one another.

The basic conditions that must be fulfilled in a contact formulation are the conservation of momentum and the compatibility conditions between the bodies in contact, such that no penetration or separation is allowed. Several FE formulations for such problems have been formulated, see e.g. Chapter 17 in [Cook et.al., 2002]. These formulations are based on specially developed contact/interface elements. In 2D, such elements represent two parallel surfaces which can be in contact in the normal direction and slide relative to one another, assuming Coulomb's friction law. The overall purpose is to determine the gained or lost contact forces in order to obtain the structural behaviour of the modelled system [Lund, 2008]. The physical function of contact elements is to sense contact when two surfaces collide or separate and automatically supply the necessary stiffness in order to prevent or limit penetration, or alternatively gap opening in the contact zone.

In FE analyses the contact algorithms provide a way to attach additional contact elements to existing solid or shell element surfaces, which are expected to come in contact [Cook et.al., 2002]. In ANSYS, an interface between two surfaces can be formulated by means of e.g. CONTA174 and TARGE170. CONTA174 is a 3D, 8-node higher order quadrilateral element which represents the contact and sliding that occurs between this element and a 3D *target* surface element such as TARGE170.

Contact elements are constrained against penetrating the target surface, while the opposite is possible. Thus, in rigid-flexible interface the target elements are usually associated with the more rigid structure in the interface, while the contact elements are associated with the more deformable structure. However, when dealing with flexible-flexible interfaces, the designation is not as obvious. Several guidelines are given for different cases in [Ansys, 2007]. ANSYS contains different types which efficiently determine how the contacting bodies behave relative to one another. These are summarized below, based on [Ansys, 2007].

Bonded contact type:

This corresponds to gluing two parts together. No relative motion, i.e. sliding or separation between edges or faces, is allowed. The advantage of this type is the possibility to obtain a linear solution as the contact area does not vary as a function of the applied load. Furthermore, applying this contact automatically ignores/closes the possible imperfections in the contact zone, such as initial gaps or penetration.

No separation:

Except for the fact that this type allows for small amounts of frictionless sliding along the contact faces, it is same as the bonded contact type. However, it only applies to regions of faces.

Frictionless:

This applies to regions of faces only. It models standard nonlinear unilateral contact, which allows free sliding and gaps to form at contact interface, but no friction between the contact surfaces is considered. Consequently, the model can be quite unstable using this type, unless appropriate additional constraints are applied as well.

Rough:

This is a nonlinear contact that allows gaps to form at contact interface but does not allow sliding, i.e. assumes infinite coefficient of friction. It applies to regions of faces only.

Frictional:

Assuming this type, the two contact surfaces can carry a certain magnitude of shear stresses within static friction until sliding friction occurs. An equivalent shear stress is defined as a fraction of the contact pres-

sure, at which sliding occurs. Exceeding this stress causes the two faces to slide relative to one another. The coefficient of friction between the two surfaces must be known.

In ANSYS, some of the outlined contact types are efficiently formulated by multi-point constraints, introduced in section 3.3. Applying the MPCs in a FE formulation can be based on several different methods. In general, these are conceptually accounted for by modifying the master stiffness equations in (3.31) to obtain

$$\{R\} = [K]\{D\} \xrightarrow{\text{MPC}} \{R\}^* = [K]^*\{D\}^* \tag{3.32}$$

Consequently, developing and solving the modified system in an FE program returns the modified DOF vector $\{D\}^*$. This overall procedure of applying MPCs is illustrated as the chart in Figure 3-4.

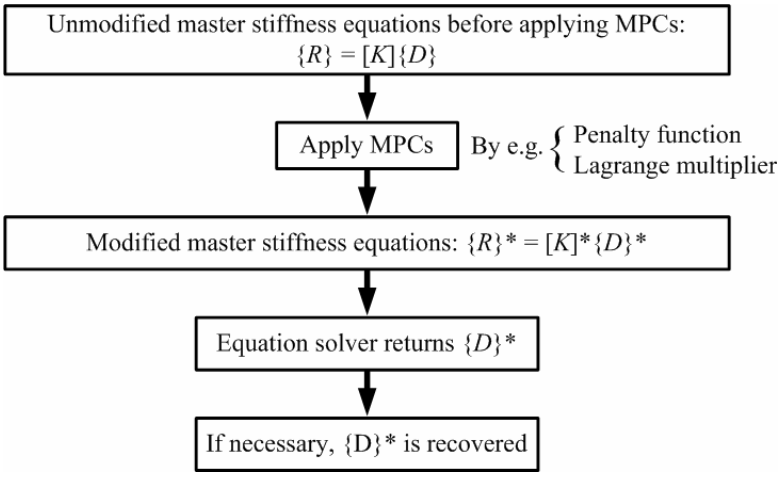

Figure 3-4: Schematic overview of the MPC application [Felippa, 2009].

In Figure 3-4, two different methods for formulating MPC contact problem are shown, namely the *penalty* method and the *Lagrange multiplier* method. It is emphasized, that these two methods can both be applied separately to formulate the problem, as well as that several modified versions of these, exist. A detailed description of the two can be found in e.g. Chapter 17 in [Cook et.al., 2002]. A brief description is given below.

Penalty method [Lund, 2008]**:**

This penalty method is based on addition of large artificial stiffness to the contact elements. Each MPC is expressed as an elastic structural element called *penalty element*, which approximately enforces the kinematic conditions. In this method, momentum is conserved while the compatibility conditions are only approximately fulfilled as the contact bodies interpenetrate. However, the penetration error is tuned by calibrating the artificial stiffness with a *penalty parameter*. The exact constraint can be recovered if this parameter goes to infinity. The MPCs are applied by augmenting the finite element model with the additional penalty elements.

Lagrange multiplier method [Lund, 2008]**:**

This method describes the kinematic conditions in a contact problem by introducing additional variables. In this case, the compatibility conditions are fulfilled while the conservation of momentum is not necessarily fulfilled, such that e.g. interface relaxation may be needed to obtain convergence. Consequently, for each MPC an additional DOF is attached to the master stiffness equations of the model. Physically, these unknowns represent contact tractions that enforce the constraints exactly, but also require additional computations to stabilize the contact conditions.

So far, some of the basic formulations of contact problems have been described. Consequently, the contact type and the finite element formulation for the contact problem in the grouted connection can be chosen. Nonetheless, it is now possible to advance into a detailed modelling of the grouted connection, as given in the next section.

3.4 Discretized Model of the Grouted Connection

The general assembly of the three main components of the monopile foundation is shown in Figure 2-5 in Chapter 2. The initial objective in this section is to create a model that entirely resembles the assumptions made in Chapter 2. The purpose of this simplified model is to verify the analytical results by comparing the stresses at chosen coordinate points in the grout. The second key issue is to create and briefly analyse a model corresponding to the physical boundary conditions, in order to evaluate the quality of the simplified model. The main assumptions from the analytical model are repeated in Figure 3-5 for convenience.

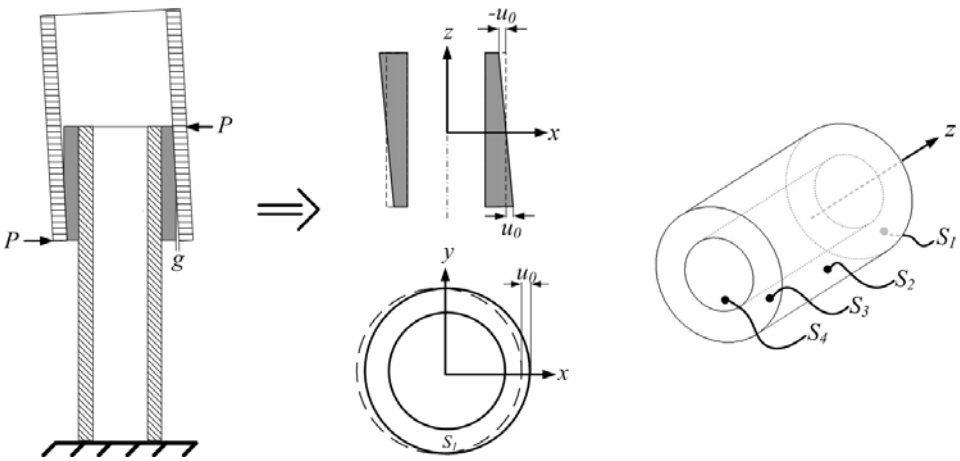

Figure 3-5: Assumptions from the analytical solution repeated.

The inner boundary surface S_1 of the grout is assumed entirely fixed, while the outer boundary surface S_2 displaces at top and the bottom skew-symmetrically with the magnitude u_0, as shown in Figure 3-5. Furthermore, the outer "rings" of the top and bottom boundary surfaces S_3 and S_4 are assumed to retain their circular shape during deformation. One way of modelling this kind of deformation of the grout is by including a portion of the sleeve, i.e. transition piece, and prescribing the known displacement u_0 to the top and the bottom

of this sleeve portion. Next, increasing the stiffness of the sleeve portion by substantially increasing its modulus of elasticity, the grout can be compressed precisely as shown in Figure 3-5. A model of this arrangement is created in ANSYS as illustrated in Figure 3-6.

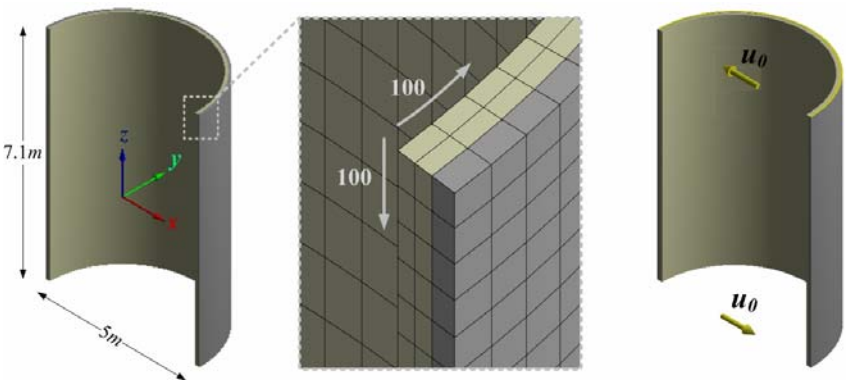

Figure 3-6: The model geometry, the mesh geometry and the prescribed displacements.

As shown in Figure 3-6, the symmetry boundary conditions have been utilized in the model, such that only a half of the structure is considered. The number of elements is thereby halved as well. The discretization of the grout and sleeve half-cylinders is subdivided into 100 elements both along *z*-axis and in the angular direction. Furthermore, the grout is given two divisions in the thickness as shown in Figure 3-6. The total number of elements is thus 30.000, while the total number of nodes is 182.608. This large number of DOF is caused by two reasons, one of which is the relatively large number of elements and the other is that the nodes on the sides of each element are included. These mid-side nodes are not shown in Figure 3-6.
Thus, both grout and sleeve are discretized into 20-node structural solid elements, as illustrated earlier in Figure 3-2. In ANSYS, this element is defined as SOLID186, which is a higher order solid element, assuming quadratic interpolation functions for the nodal displacements. This higher order element is chosen rather than a lower-order 8-node element, defined as SOLID185 in ANSYS, in order to interpolate the displacements between the nodal values more accurately. However, the general capabilities of the two elements are equal, covering e.g. plasticity, stress stiffening, large deflection and large strain. The advantage of SOLID186 is that it attains any spatial orientation in the mesh, such that more irregular solid geometries can be modelled. Detailed description of this element can be found in [Ansys, 2007].

The loading input representing the force couple in the model are defined by the equivalent displacements u_0, which acts skew-symmetrically on the top and bottom surface of the sleeve, as shown in Figure 3-6. In ANSYS, these are modelled as rigid surface constraints, defined as *remote* boundary conditions. In general, such boundaries can be located arbitrarily in space and are coupled to the reference nodes as either rigid or deformable. The rigid surface constraints, related to the nodes on the two surfaces, are coupled to the motion of a single pilot node displaced by the magnitude u_0. In this case, the pilot node is located at the symmetry line

of the top and bottom plane of the connection. This formulation utilizes the capability of MPCs, introduced in section 3.3, as these efficiently describe the rigid relation between the pilot node and the contact surfaces. To preserve consistency with the analytical model, the inner surface of the grout, i.e. interface between grout and pile, is entirely fixed. Furthermore, the vertical displacement of the top and bottom of both grout and sleeve are constrained, in order to ensure that these solely displace horizontally during deformation, as assumed in the analytical model. The possible gap between the sleeve and grout, or alternatively pile and grout, is disregarded in the analytical procedure. Therefore it is essential to utilize the properties of the bonded contact type for the interface between grout and the sleeve, as described in subsection 3.3.1. The fact that this contact type leads to a linear solution reduces the solution time and matches the fact that no nonlinear effects are considered in the analytical analysis. Furthermore, the MPC formulation is chosen to efficiently constraint the two surfaces such that no gaps or sliding occurs. Here, the interface surface of the sleeve portion is chosen as the rigid target by "attaching" TARGE170 target elements on it, while the grout is the deformable contact body that includes CONTA174 contact elements. The entire system is solved in ANSYS using a direct solver, based on direct elimination of master stiffness equations in (3.32). The results obtained by this model are presented and compared to the analytical solution in the following section.

3.5 Comparison of Analytical and Numerical Results

In subsection 2.7.2 the analytical results were compared to a simplified 1D model, which gave good correspondence. In this section the results, obtained by the analytical and numerical 3D analyses, will be compared. The main purpose is to verify whether the derivation and computer coding of the analytical solution is done correctly, as the FEM results should be in a good resemblance. The normal and the shear stress distribution in the grout obtained by the FE model described in previous section are as shown in Figure 3-7.

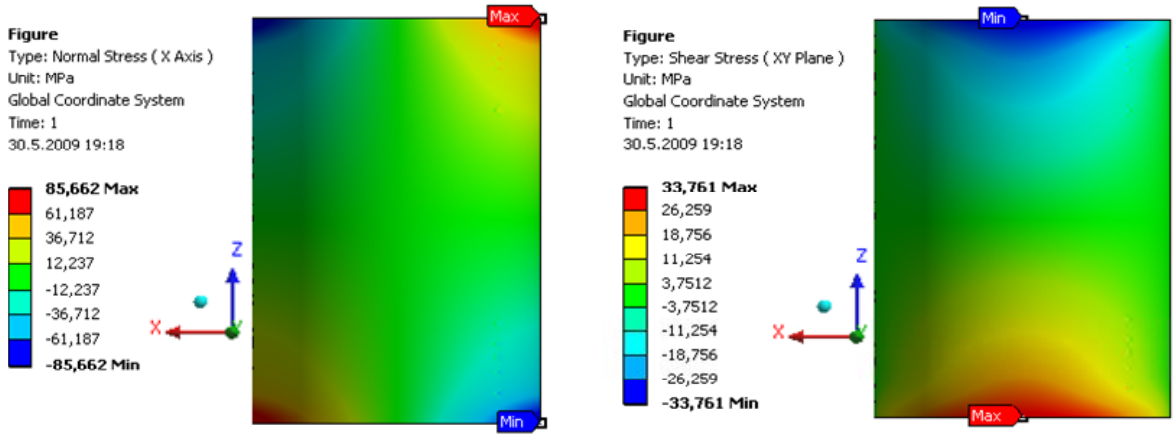

Figure 3-7:Normal stress and shear stress results in the grout from the FEM model.

As expected, a skew-symmetric distribution of compressive and tensile stresses is obtained, which corresponds to the made assumptions. The stresses at different coordinate points on the top of the grout are compared in Table 3-1.

$(r,\theta,z)=(2.44m,0,3.55m)$						
Solution Method	σ_{rr} [MPa]	$\sigma_{\theta\theta}$ [MPa]	σ_{zz} [MPa]	$\sigma_{r\theta}$ [MPa]	$\sigma_{\theta z}$ [MPa]	σ_{rz} [MPa]
3D Analytical	-80.8	-18.9	-18.9	0	0	0
FEM	-85.7	-19.8	-18.7	0.7	0	0
$(r,\theta,z)=(2.4m,\pi/4,3.55m)$						
3D Analytical	-59.9	-14.2	-14.1	23.6	0	0
FEM	-60.5	-13.9	-12.9	22.9	0	0
$(r,\theta,z)=(2.4m,\pi/2,3.55m)$						
3D Analytical	0	0	0	33.4	0	0
FEM	0	0	0	32.4	0.1	0

Table 3-1: Stresses at 3 points in the grout by 3D analytical and FEM solutions.

The maximum value of the normal stress, found at $(r,\theta,z)=(2.44m,0,3.55m)$, is found to be in good conformity with the 1D and the two 2D solution methods, presented in subsection 2.7.2. These results are repeated in Table 3-2 for convenience.

1D [MPa]	*2D Static [MPa]*	*2D Elastodynamic [MPa]*	*3D Elastodynamic [MPa]*	*FEM [MPa]*
-85.4	-84.8	-84.8	-80.8	-85.7

Table 3-2: Maximum normal stress by 1D, 2D, 3D and FEM solution methods.

As before, the error of the 3D analytical solution is approximately 5 %. It is once again emphasized that the 2D elastostatic and elastodynamic solutions are exact, with respect to the assumptions made, which is why the value of -84.8 *MPa* is taken as the correct value. Nevertheless, Table 3-1 demonstrates that a very good correspondence is found at all three points, which confirms that the analytical solution and all coding in Mathematica program codes are carried out correctly. Further verification is shown in Figure 3-7, proving that results along the entire boundary are in coherence. The angle is measured counter-clockwise from *x*-axis.

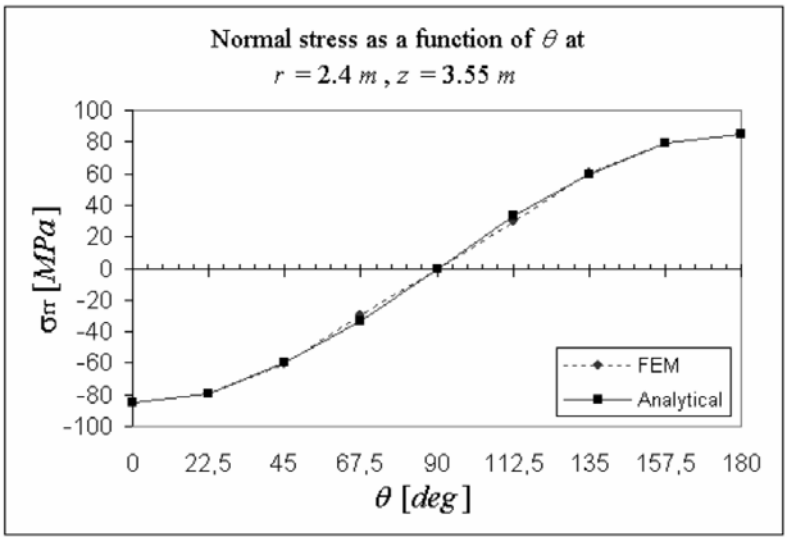

Figure 3-8: Conformity of the angular distribution of normal stresses at top of the grout.

Hence, the results at the upper and lower boundaries, i.e. surfaces S_1 and S_3 shown in Figure 3-5, are verified. As FEA showed good correspondence for these, it is presumed that the stress distribution along the grouted connection is reasonable in as well. However, observing the distribution along the connection length, a larger error is found. This is illustrated in Figure 3-9.

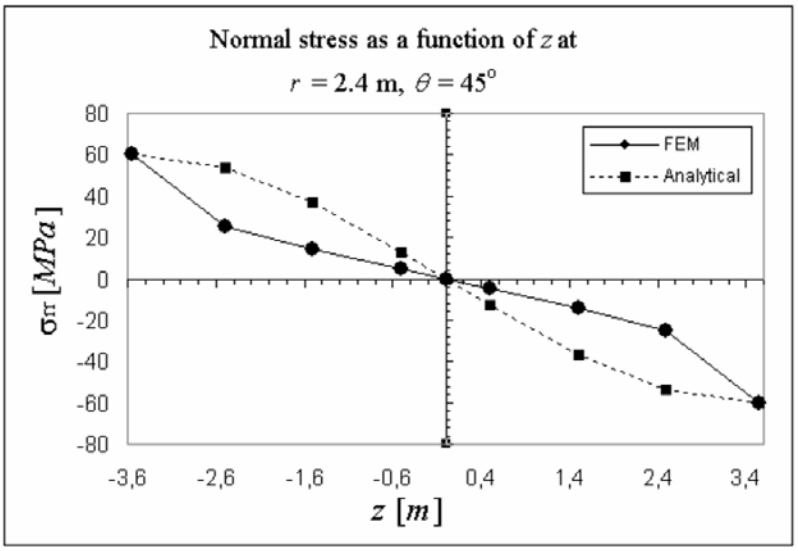

Figure 3-9: Analytical and FEM radial stress distribution along the connection length.

As seen in Figure 3-9, the values at top and bottom are coincident, while a difference up to 30 *MPa* is obtained at approximately ± $L_G/4$. As discussed earlier, this is a direct consequence of the displacement distribution along the connection being the one-term approximation of the odd sine series. Nevertheless, the largest stresses can be effectively determined as the error is much lower in the vicinity of the top and bottom boundaries, where these occur. Consequently, the overall results have been verified. The next step is to evaluate whether load transfer in the connection is efficiently modelled by means of the force couple and the equivalent displacements. This is carried out by referring to a more detailed model, as elaborated in the next section.

3.6 Comparison of the Simplified and Advanced FE Model

So far, the simplified analytical solution has been presented and fairly verified by corresponding FEA. However, these analyses assume that the deformation of the grout is maximum at the two opposite ends of the connection and zero precisely at the middle of the connection. This implies that the efficient contact length of the interface between grout and sleeve, respectively grout and pile, during deformation is $L_G/2$. Whether this is a too rough assumption or not should be estimated experimentally. As this has not been an option, the alternative is an extensive FE model of the entire connection. As stated at the beginning of this chapter, an equivalent connection has been modelled and analysed by [Andersen and Petersen, 2004]. Some of the relevant results obtained in their analysis are presented in the following.

3.6.1 Result from the Advanced FEA

The paper given in [Andersen and Petersen, 2004] is based on work carried out in connection with the development of the DNV standard [DNV-OS-J101, 2007], together with experiences from verification work for grouted connections. In relation to the development of this standard, FE analyses are preformed in order to lay down guidelines for FE calculations of grouted connections subjected to bending. This load is considered as the governing load from the wind turbine, as discussed in Chapter 1. Therefore, the results contained in their paper are assumed unquestionable. It is noted that this paper is enclosed in the attached CD, see [Andersen and Petersen, 2004].

The main conclusion to the analysis preformed in their paper is the fact that load transfer in the connection is in fact mainly transferred as force-couple in the top and the bottom of the grouted region. This is verified by FEA models that apply a frictional contact formulation to describe the interface between the grout and steel surfaces, as presented in subsection 3.3.1, as well as a nonlinear constitutive model for the grout. The details of the model can be found in [Andersen and Petersen, 2004]. Figure 3-10*a)* shows the deformed state of the pile and sleeve, respectively, where colour plots indicate von Mises stresses and the red circles the zones with high stress concentrations.

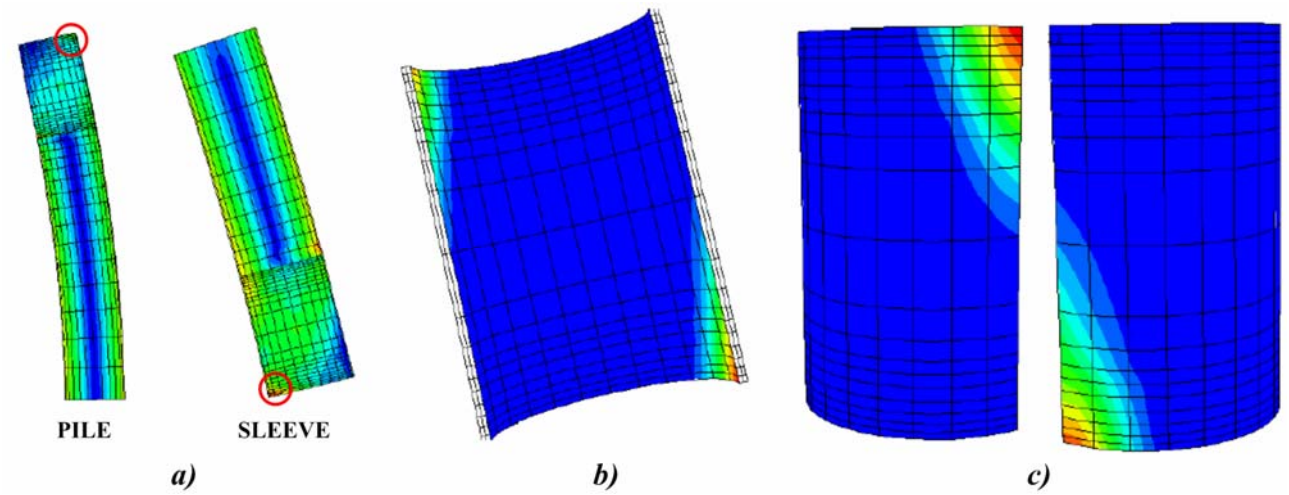

Figure 3-10: Gap opening between pile and grout in a) and between sleeve and grout in b).

Furthermore, Figure 3-10*b)* and *c)* illustrate regions containing gap opening in the pile-grout and sleeve-grout interfaces, respectively. Thus, the shown plots confirm that the highest stresses in the grout will occur at the opposite ends of the top and bottom, as well as that gap openings in the two interfaces will occur reversely. Consequently, it can be verified that the loads are in fact mainly transferred as a force-couple, which corresponds to the same assumption made for the analytical analysis in Chapter 2. Furthermore the work done by [Andersen and Petersen, 2004] is compared to an experimental scale model, conducted in the Structural Laboratory at Aalborg University, DK, in 2001. The test setup is shown in Figure 3-11.

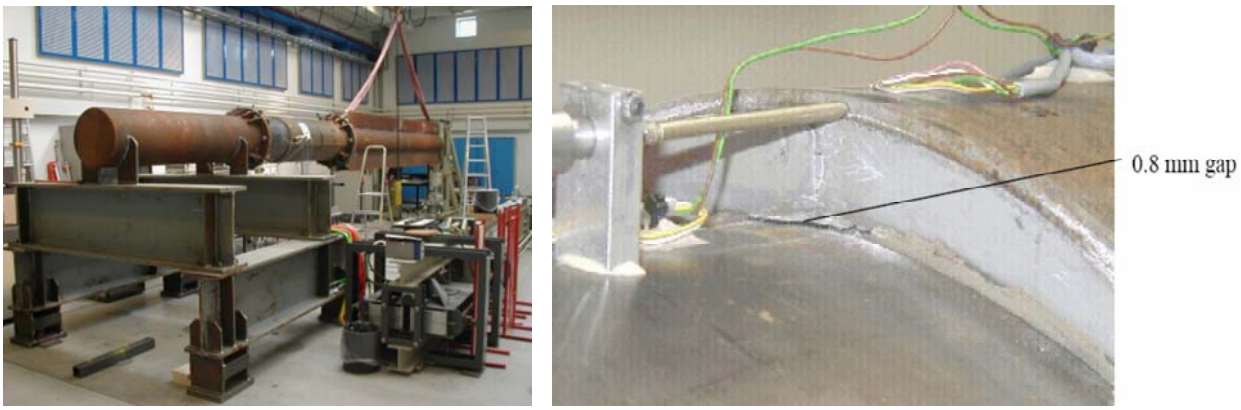

Figure 3-11: The experiment setup (left) and a gap between pile and grout (right).

During the experiments a minor gap at one end of the connection has been observed, as shown in Figure 3-11. This is a further verification of the load being transferred as a force-couple. Consequently, the simplified model considered in the analytical part of this report is hereby validated as very reasonable.

In the next chapter, all assumptions and simplifications made during creation and analysis of the simplified model are summarized and discussed in order to evaluate the quality of the overall results obtained in this report.

Chapter 4

4. Discussion

The problem statement for the project underlying this report is addressed by analytical and numerical solution procedures, as experimental procedures. Generally, analytical solutions are particularly satisfying if they can be used to a wide class of problems, such that particular solutions can be obtained by substituting the values of the parameters involved. However, such solutions are usually restricted to regular geometries and simple boundary conditions. For this reason, numerical procedures are far more popular among engineers, even though approximate results are obtained.

The problem treated in this report appears rather simple, considering the relatively simple and axis-symmetric geometry of the grouted connection. The analytical part has been preformed by utilizing the characteristics of symmetry in which trigonometric functions have been advantageously used to describe the state of deformation. However, it has been necessary to perform several simplifications, in order to use such simple relations. All simplifications and restrictions assumed throughout the report are summarized and discussed in the following section.

4.1 Evaluation of the Utilized Restrictions and Simplifications

Physical structure simplifications

All external equipment, welded or bolted to the structure has been disregarded, thus idealizing the structure solely by pile, grout and sleeve. In view of a static structural analysis, this step is both convenient and reasonable. One reason is the fact that the three components have much larger geometries, compared to the attached equipment. The effect of welds on the structure, particularly that of the alternative shear keys, are primarily to be considered in fatigue analyses, if stress concentrations involved with these are found significant. Consequently, this step is not found to influence the end results.

The two pipes and the grout filling the annuli are assumed concentric and cylindrical. The verticality tolerances that may occur during piling and grouting process are most likely to be different from one foundation to another. However, this tolerance is of minor importance as this usually involves low angles of rotation,

which primarily influence the frictional forces when considering vertical load transfer. Both analytical and numerical analyses assume perfect symmetry. The effect of large tolerances has not been the subject in this report, but dealing with large difference in grout thickness at two sides of one end of the connection may require particular numerical analyses.

Loading simplifications

The equivalent horizontal load at the top of transition piece has been modelled as a force-couple transferred directly to the grouted connection. This appears quite natural considering that the moment is usually characterized as a force-couple. In addition, this has been verified in the previous chapter by considering FE and experimental model compared in [Andersen and Petersen, 2004].

The equivalent displacement u_0 from the force-couple is used as the sole input in the analytical analysis. This is found very convenient in the performed analysis, however, a preferable load input would be the actual horizontal load transferred from the sleeve to the pile through the grout. Estimation of this equivalent displacement in terms of the horizontal load has not been a topic in this work. This could be a subject of further work in which e.g. a model based on Mechanics of Materials can be formulated to obtain this input.

Frictional contact effects have been disregarded in both analytical and numerical parts of this work. As discussed in several contexts, this effect is of main importance when considering the vertical load transfer. Dealing with relatively large coefficients of friction may introduce significant shear stresses in the grout along the two interfaces. Nevertheless, these will presumably always be irrelevant compared to the radial stresses, when considering horizontal load transfer.

Material simplification

Both in analytical and numerical parts of this work, the reinforced grout/concrete has been treated as linearly elastic and isotropic material. In reality, concrete does exhibit elastic behaviour up to cracking. However, the assumption of isotropy in concrete at the material macro level should be used only in an approximate sense [Kotsovos and Pavlovic, 1995]. Anisotropic effects in the compression could be small but this would require experimental verification before it could be safely assumed. However, considering that the steel fibres in the reinforced concrete are randomly distributed, it is presumed that the effect of anisotropy is of minor importance for the derived solution.

Modelling simplifications

In order to simplify the analytical work, the linear distribution of the displacement along the grouted connection is assumed, which is equivalent to a bonded connection. This imposes a skew-symmetric deformation by which one half of the length is compressed, while the other is in tension. It is obvious that no tension can

occur as no bonding in the interface exists, making this a "virtual" assumption. Thus the parts of the grout assuming tension should be ignored when evaluating the results. However, due to symmetry and the isotropic material assumption, both tensile and compressive stresses are equal in value with different signs, such that no particular precautions need to be taken when defining the direction of the load input.

The outer boundary of the grout, whish corresponds to the inner surface of the sleeve, is assumed to deform as a rigid body, i.e. maintain the circular shape during deformation. This is found reasonable as the stiffness, being a function of the elastic modulus, of the sleeve is three times larger than of the grout, as E_G = 70 GPa and E_S = 210 GPa. This applies as the linear isotropic elasticity is assumed.

Mathematical simplifications

It has been demonstrated in Chapter 3 that the largest error in the analytical solution method is related to the one-term approximation of the Fourier power series of the sine function. This is used to describe the displacement distribution along the length of the grouted connection as simple as possible. In general, a function describing a given relationship can be arbitrary, as long as some underlying conservation principles are satisfied. This is valid, as it is always possible to expand this function by means of e.g. Taylor polynomial or Fourier power series expansion, where several higher order terms can be included. Thus, including several higher order terms would definitely improve the end results. However, this would also demand larger effort during the analytical derivations.

4.2 Overall Evaluation of the Obtained Solutions

In view of the utilized one-term approximation, the correspondence between the analytical solution and the corresponding FE solution is found rather satisfactory. Comparing the computational solution effort in the two methods, the analytical solution returns displacements, strains and stresses at any point in the grout in a matter of seconds, while either direct or iterative FE solver needs at least the order of minutes to do the same. Even though the analytical method does not account for contact effects and nonlinear material behaviour, it is argued that these effects are of minor importance when considering the horizontal load transfer. Consequently, the quality of the obtained analytical solution method is comparatively high, considering the discussed advantages / disadvantages, and thereby much more competitive than the corresponding FE solution method.

Another satisfactory outcome of this report is demonstration of the ease and efficiency of solving elastostatic problems by means of an elastodynamic approach. The advantage of this approach is demonstrated in section 2.5. It is shown that elastostatic problem can be approached by solving the 4th order biharmonic equation with four unknowns for each potential function (= 12 unknowns in 3D). Subsequently, it was demonstrated that it is more efficient and equally exact to approach the elastostatic problem by solving the 2nd order har-

monic equations with 6 unknowns altogether, in which frequency is set to a very low value. The latter approach produces both faster and easier solutions, with less concern of developing relations between the unknowns to match the number of available equations.

Furthermore, in [Olsson, 1984, p.128], the author claims that: *"...it seems clear that a decomposition into Lamé potentials in the elastostatic case is, if not useless, at least highly unnatural."* Thus, his statement can be disconfirmed as the opposite has been demonstrated in this work. The only reservation is, however, that the frequency cannot be set to zero but to a small value in stead. Assuming a sufficiently small value fairly characterizes a fully static structural behaviour.

Chapter 5

5. Conclusion

The primary objective of this report was to develop parametric formulae for the 3D governing field equations in grouted connections due to horizontal load transfer. The analytical treatment is initialized by assuming that the horizontal load is transferred to the grout as a force-couple. Benchmarking was made by considering an advanced FE analysis conducted by an external source, where it was found that this approximation was very reasonable.

In stead of utilizing the magnitude of this force-couple directly, an equivalent displacement has been defined, which deformed the grout skew-symmetrically at the two ends. This has advantageously allowed the problem to be defined as a displacement, i.e. Neumann, boundary value problem. In addition, the axis-symmetry of the connection has allowed a description of the boundary conditions in terms of simple trigonometric relations for the radial and angular displacement components, while longitudinal component had to be approximated by Fourier power series. The governing field equations are derived accordingly, namely as a displacement solution formulation. It was chosen to derive this formulation by means of elastodynamic equations of motion, rather than elastostatic equilibrium equations, although the static loading is considered.

The first issue encountered was that the derived equations were stating a coupled system, but resolved by introducing a decomposed displacement field expressed by harmonic functions. Further derivation led to a system expressed by wave equations, which describe the wave propagation in elastic media as a function of the displacement field. Next, separation of variables in these was performed in order to separate the spatial and time harmonic dependence. The final outcome was that the entire system was described by 2nd order ordinary differential equations, taking the form of modified Bessel's equation.

The first attempt to solve these was by reducing the problem into 2D and omitting the time harmonic part by assigning zero angular frequency. This attempt was of no use as it led to an inconsistent system of equations. The second attempt included the time harmonic part leading to a consistent system that was solved exactly. This is verified by a comparison to a corresponding elastostatic solution. Comparison of the two exact solutions gave excellent correspondence with low values of frequency in the elastodynamic solution. This veri-

fied that the same was valid in a 3D attempt, which was solved approximately and compared to the 2D exact solutions. The latter comparison gave very good correspondence of the field values for the radial and angular components.

Further comparison with a corresponding 3D FE model gave excellent correspondence in the radial and angular directions, while the larger disagreement was obtained in the longitudinal direction. This difference was found to be due to the one-term approximation of the displacement along this direction. Furthermore, it has been proven that use of displacement decomposition and elastodynamic approach can be applied to elastostatics, even though it is claimed differently in e.g. [Olsson P, 1984]. However, this requires that the frequency is sufficiently small.

The overall result obtained in this project comprises an analytical solution of the 3D field equations in the grouted connection in an approximate sense. This result is satisfactory for obtaining maximum field values but involves larger tolerances when evaluating these at several other points. However, this is a direct consequence of the one-term approximation for the one of the displacement components, such that additional terms should reduce the errors involved. Consequently, using the obtained analytical solution is very reasonable and very time efficient compared to FE analyses, especially if a quick evaluation of the stress state in the connection is desired.

REFERENCES

[Andersen and Petersen, 2004]
Andersen S. Morten and Petersen M. Peter (2004). Structural Design of Grouted Connection in Offshore Steel Monopile Foundations. *Global Windpower 2004, Det Norske Veritas, Roskile*, DK, 2004
CD Path: CD\Lecture Notes and Papers\Structural Design of Grouted Connection.pdf
URL: www.dnv.com/certification, 20 April 2009.

[Andreasen, 2007]
Andreasen H. Jens (2007). Brudmekanik. *Institut for Maskinteknik, Aalborg Universitet, Lecture Notes*.
CD Path: CD\Lecture Notes and Papers\Brudmekanik.pdf

[Ansys, 2007]
ANSYS (2007). Release 11.0 Documentation for ANSYS Workbench. Ansys Inc., 2007.

[Aster, 2008]
Aster Rick (2008), The Seismic Wave Equation, January 25, 2008, pp. 9, URL: http://www.ees.nmt.edu/Geop/Classes/GEOP523/Docs/waveeq.pdf, May 05 2009.
CD Path: CD\Lecture Notes and Papers\The Seismic Wave Equation.pdf

[Britanica, 2009]
Bessel's equation**.** *Encyclopædia Britannica*, 2009. Encyclopædia Britannica Online, 14 May 2009, URL: http://www.britannica.com/EBchecked/topic/63055/Bessels-equation

[Brodachev, 1995]
Brodachev N.M. (1995). Three-Dimensional Elasticity Theory - Problem in Terms of the Stress. *International applied mechanics, vol, 31, no. 12, 1995.* Online available at URL: http://www.springerlink.com/content/ph7388632w2363t2/fulltext.pdf, May 20, 2009.
CD Path: CD\Lecture Notes and Papers\Problem in Terms of the Stress.pdf

[Chan et.al., 2005]
Nguyen V.B. and Andrew H.C. Chan (2005). Comparisons of Smeared Crack Models for RC bridge Pier Under Cyclic Loading, *Department of Civil Engineering, University of Birmingham*, Birmingham B15 2TT, UK. URL: http://www.acmeuk.org/13_Conference/paper_26.pdf, April 30 2009.

[Cook et.al., 2002]
D. Cook Robert, S. Malcus David, E. Plesha Michael and J. Witt Robert (2002). Concepts and Applications of Finite Element Analysis – Fourth Edition. *John Wiley & Sons. Inc.*, NJ, United States

[Densit, 2009]
Densit ApS, Grouting Offshore Wind Turbine Foundations: Offshore Wind. URL: http://www.densit.com/Offshore_wind/Ducorit(R)_Grout.aspx, 30. April 2009.

[Drucker & Prager, 1952]
Drucker, D. C. and Prager, W. (1952). Soild mechanics and plastic analysis for limit design. *Quarterly of Applied Mathematics*, vol. 10, no. 2, pp. 157–165.

[Felippa, 2009]
Felippa Carlos (2009). Introduction to Finite Element Methods. *ASEN 5007, Department of Aerospace Engineering Sciences, University of Colorado at Boulder*, Fall 2008
URL: http://www.colorado.edu/engineering/cas/courses.d/IFEM.d/, April 24. 2009

[Franca, 2009]
Franca Leopoldo (2009). Derivation of Helmholtz Equation from the Wave Equation. *Research Activities and Group of Leo Franca,* May 14 2009
URL: http://www-math.cudenver.edu/~lfranca/research/students/tim/presentation/derive/

[Gere, 2002]
Gere M. James (2002). Mechanics of Materials – 5th SI Edition. *Nelson Thornes Ltd 2001*, Cheltenham, UK, pp. 655 & 888

[Guz, 1986]
Guz A.N. (2986). Elastic Waves in Prestressed Continua, Vol.2. *Propagation of Waves – Kiev: Naukova Dumka*, 1986, 536p. (In Russian).

[Irvine et. al, 2003]
Irvine, J.H., Allan, P.G., Clarke, B.G., Peng, J.R., (2003). Improving the Lateral Stability of Monopile Foundations, *Proceedings of the BGA International Conference on Foundations innovations, observations, design and practice,* Thomas Telford, London, pp.371-380.

[Kanvinde et.al., 2001]
Kanvinde, A, Deierlein, G, Hajjar, J (2001). Material Nonlinear Analysis of Structures – A Concentrated Plasticity Approach, *John A Blume Earthquake Engineering Center Civil and Environmental Engineering, Stanford University*, May 2001, US. URL: http://cee.engr.ucdavis.edu/faculty/kanvinde/concenplast.pdf, April 10 2009

[Kraft, 2009]
Kraft, M.K. (2009). Why Cure Concrete? *KE: Kraft Energy – Concrete Curing Systems*. URL: http://www.kraftenergy.com/intro-whycure-concrete.htm, May 03 2009.

[Lund, 2007]
Lund Erik (2007). Noter/overheads til Elementmetoder 3 for DMS7, Lektion1. Department of Mechanical Engineering at Aalborg University, 2007
CD Path: CD Path: CD\Lecture Notes and Papers\FEM 3 Noter.pdf

[Lund, 2008]
Lund Erik (2007). Introduction to Contact Problems. *Notes/Slidess for Finite Element Methods 4, DMS8, Lecture 3*. Department of Mechanical Engineering at Aalborg University, 2008
CD Path: CD Path: CD\Lecture Notes and Papers\FEM 4 Noter.pdf

[Morse, 1953]
Morse P.M. and Feshbach H. (1953). Methods of Theoretical Physics Vol.2. McGraw-Hill, N.Y., 1953, 886p

[Olsson, 1984]
Olsson Peter (1984). Elastostatics as a Limit of Elastodynamics – A Matrix Formulation. *Applied Scientific Research 1984, Institute of Theoretical Physics*, *Göteborg, Sweden*.
CD Path: CD\Lecture Notes and Papers\ Elastostatics as a Limit of Elastodynamics.pdf

[P7, 2007]
Sørensen J., Montes H.U., Nessari M., Dedic N. (2007). Stress and deformation analysis of a load carrying structural element. *Personal Semester Dissertation at Institute of Mechanical Engineering – Aalborg University*, Autumn 2007, pp. 20-24
CD Path: CD\ Lecture Notes and Papers\P7 Report.pdf

[Rao, 2004]
Rao S. Singiresu (2004). Mechanical Vibrations, Fourth Edition. *Pearson Education International, Prentice Hall*, Upper Saddle River, New Jersey, US, 2004, pp.45-47

[Rogers et. al, 2003]
Rogers, A.L., Manwell, J.F. and McGowan, J.G., (2003). A Year 2000 Summary of Offshore Wind Development in the United States, *Energy Conversion and Management*, Vol. 44, pp.215-229.

[Sadd, 2004]
Sadd, Martin H. (2005). Elasticity: Theory, Applications, and Numerics. *Elasavier Academic Press*, *Elsavier Butterworth-Heinemann*, New York, NY, USA, pp. 83-86. Online available at URL: http://books.google.com/

[Schjødt, 2005]
Schjødt J.T. (2005). Lecture Notes On: Continuum Mechanics – Selected Topics. Aalborg University, June 2005.
CD Path: CD\Lecture Notes and Papers\Lecture Notes on Continuum Mechanics.pdf

[Shames & Dym, 2003]
Shames H.I and Dym, L.C. (2003). Energy and Finite Element Methods in Structural Mechanics. *SI units edition, Taylor & Francis Books, Inc*, New York, USA, pp.46-48

[Slepyan, 1972]
Slepyan L.I. (1972). Transient Elastic Waves. *Leningrad: Sudostroenie, 374p* (In Russian).

[Stein, 1994]
Stein Seth and Michael Wysession (1994). An introduction to seismology, earthquakes, and earth structure. *Wiley-Blackwell, 2003*, pp. 53. Online available at URL: http://books.google.com/

[Sørensen, 2009]
Personal interview with the Associate Professor M.Sc. Ph.D. Eigil V. Sørensen from Department of Civil Engineering, Aalborg University, DK, February 10. 2009

[WindEnergy, 2009]
Wind Energy – The Facts (WindFacts). *European Wind Energy Association (EWEA)*. URL: http://www.wind-energy-the-facts.org/en/part-i-technology/chapter-5-offshore, 10. April 2009

[Weisstein, 2009]

Weisstein, Eric W. (2009). Harmonic Function. From *MathWorld* - A Wolfram Web Resource. Online available at URL: http://mathworld.wolfram.com/HarmonicFunction.html

[Westgate et. al. 2005]
Zachary J. Westgate, Jason T. DeJong (2005). Geotechnical Considerations for Offshore Wind Turbines, Report on Planning, Designing and Constructing an Offshore Wind Farm, UK
CD Path: CD\Lecture Notes and Papers\Geotechnical Considerations for Offshore Wind Turbines.pdf

[Kotsovos and Pavlovic, 1995]
Kotsovos M. D. and Pavlovic M. (1995). Structural Concrete: Finite-Element Analysis for Limit-State Design. Online available at: http://books.google.com

APPENDIX

Appendix 1 – Overall Monopile Installation Procedure

Installation methods and tools

Hammer size and drive force

The German manufacturer Menck is offering hydraulic hammers for driving big monopiles in the below classes.

MHU	Energy	Weight	Length	
	(KJ)	(t)	(m)	(feet)
550S	550	135	13.8	45
800S	800	167.4	15	49
1900S	1900	292	23.2	76

Pile in drive gate with hammer in place

Drive drill drive

Two different applications for drilling inside the pile in order to drive the pile to final depth

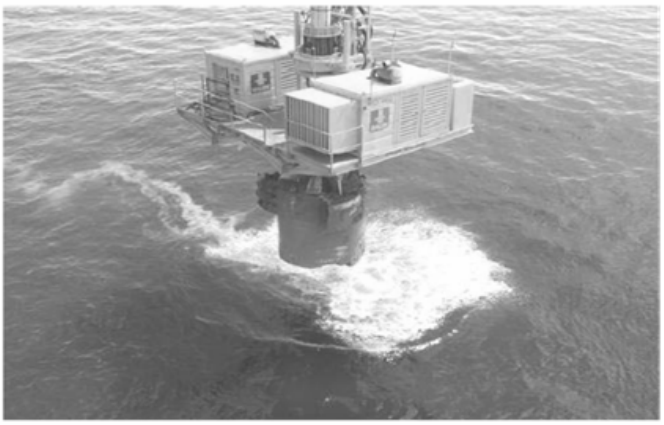

Installation of transition piece

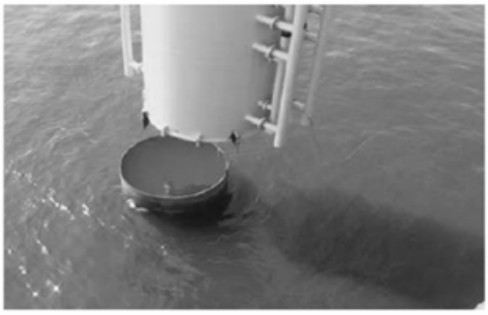

Photographs and descriptions are based on “Efficient offshore wind turbine foundations“ by [Densit2, 2007].

Appendix 2 – Grout Properties by Provider

Data Sheet
Ducorit®

- ultra high performance grout

Densit has developed a series of unique products especially for offshore wind turbine application. The Ducorit® grouts show extreme mechanical properties, accommodating with any grout material requirement.

DUCORIT®

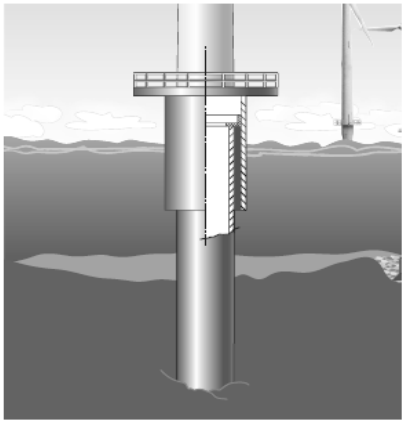

APPLICATIONS

Ducorit® is used within the offshore wind turbine industry, connecting the tower section to the monopile. The material has unique properties and the grouting technique has the following advantages:

- Easy and swift installation
- Possibility of adjusting for verticallity
- Proven technology
- J-tubes, boat landings and other accessories can be mounted on the transition piece for quick installation

PRODUCTS

The core of the Ducorit® products is the unique Densit® Binder. The different properties of Ducorit® S1, Ducorit® S5 and Ducorit® D4 are obtained by adding aggregates such as quartz sand or bauxite.

Ducorit® products are characterised by extreme strength and stiffness, making them a strong structural component and not just a "filling material". Using Ducorit® for offshore application does not require special precautions with respect to environmental or personal hazards.

SHRINKAGE

Ducorit® products exhibit very low shrinkage, thus grout and surrounding steel remain in physical contact after curing. When cast in a 100% RH environment, the shrinkage is virtually reduced to zero.

HEAT OF HYDRATION

Due to the material composition and low water/cement ratio, Ducorit® shows limited heat of hydration eliminating the risk of thermal cracking and deterioration, also when casting in large volumes.

Densit

PUMPABILITY & UNDERWATER OPERATIONS

Ducorit® products are pumpable up to several hundred metres through 2" and 3" hoses. Due to viscosity and high inner cohesion of the mixed material, there is no risk of washing out cement particles, separation or mixture with water when cast below sea level.

EARLY STRENGTH DEVELOPMENT

Ducorit® products develop a significant early strength. After curing just 24 hours at 20°C (68°F), the strength reaches 50% of the long term value. The early strength is even more pronounced in regard to the material stiffness.

FATIGUE

Due to ultra high strength and durability of Ducorit® products, the fatigue strength is outstanding compared to normal concrete. As fatigue strength depends upon the static strength of concrete, the fatigue strength of Ducorit® can be up to more than 50 times the strength of normal concrete.

FIBRE REINFORCEMENT

Steel fibres can be added to Ducorit® S5 and D4. Applying steel fibres, the tensile and bending strength reaches considerable levels as the material shows significant ductility and high fracture energy. The pumpability remains intact.

DOCUMENTATION

The mechanical properties below have been documented through extensive test work.

Mechanical Properties

		D4 Mean	S5 Mean	S1 Mean
Compressive strength f_c	[MPa/psi]	200 / 29,000	130 / 18,850	110 / 16,000
Static modulus of elasticity E_c	[GPa/ksi]	70 / 10,000	55 / 8,000	35 / 5,000
Dynamic modulus of elasticity E_d	[GPa/ksi]	88 / 12,800	60 / 8,700	37 / 5,400
Tension strength f_t	[MPa/psi]	10 / 1,500	7 / 1,000	5 / 725
Flexural strength f_{cf}*	[MPa/psi]	23.5 / 3,400	18 / 2,600	13.5 / 2,000
Density ρ	[kg/m³]	2740	2440	2250
Poisson's ratio ν		0.19	0.19	0.19
Fracture energy G_f*	[kN/m]	12	5.6	4.0
Static coefficient of friction μ		0.6	0.6	0.6

Note that the stipulated values are mean values, based on 75x75 mm cubes i.e. the recommendable design values are slightly smaller.

(minimum 28 days curing at 20°C)
** with 1.9% by volumen of steel fibres*

Densit

Densit ApS · Tel. +45 9816 7011 · Fax +45 9933 7788 · E-mail: mail@densit.com · Internet: www.densit.com

Appendix 3 – Provided Geometry and Load Input

The following sketch has been received from ISC [Lundgaard A., 2009]:

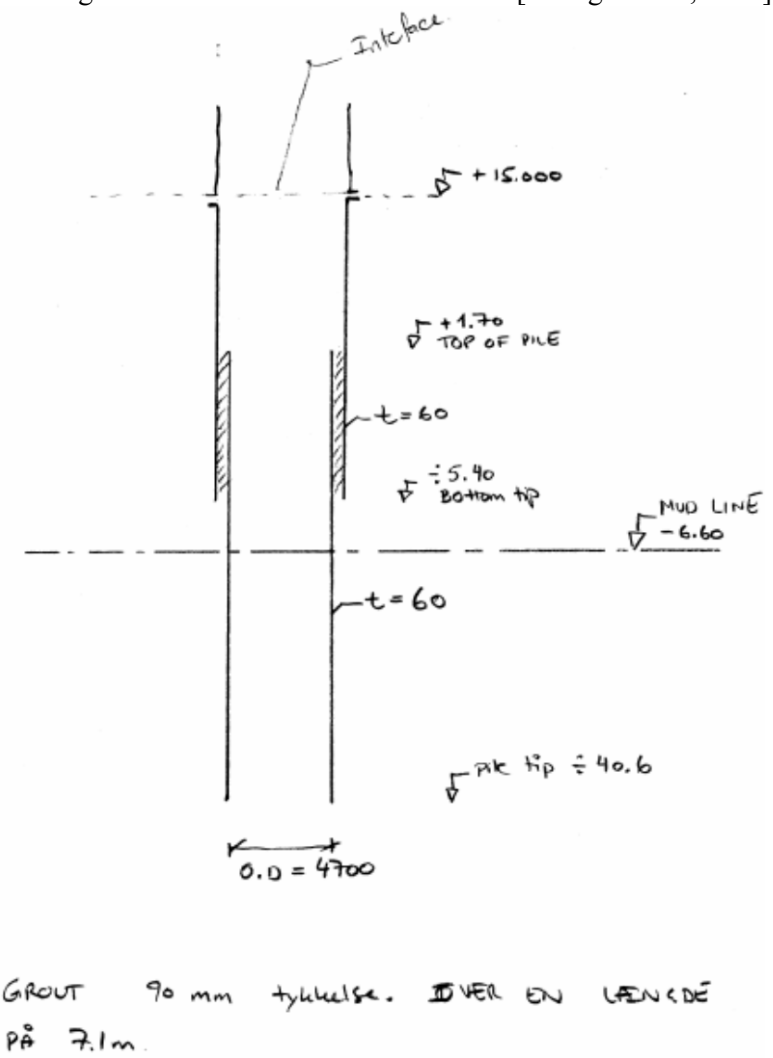

In addition, the following horizontal load at the top of the transition piece (Interface) has been provided: ***P* = 2650 *kN*.** The geometry is specified according to the Figure 1-4 as:

Outer pile diameter, D_p:	4700 *mm*	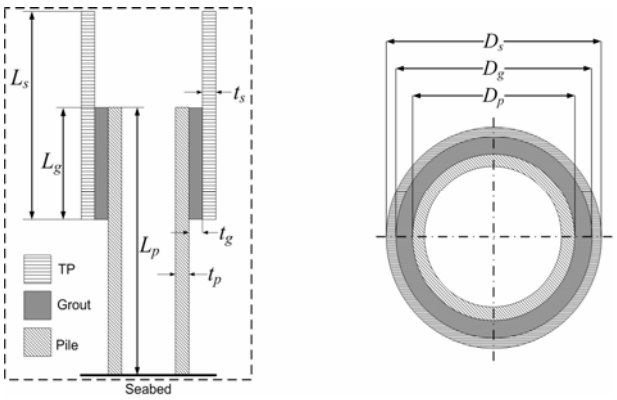
Outer grout & sleeve diameter, D_g, D_s:	4880 *mm* 5000 *mm*	
Thickness of the grout / annuli, t_g:	90 *mm*	
Thicknesses of pile and sleeve, t_p , t_s:	60 *mm*	
Length of the pile, L_p:	15000 *mm*	
Length of the sleeve, L_s:	20400 *mm*	
Length of grouted connection, L_g:	7100 *mm*	

The properties of steel utilized for the pile and the transition piece, both 60 *mm* in thickness, according to [Lundgaard A., 2007]:

Table 0-1: Yield strength [MPa]

Thickness [*mm*]	Ultimate Load State S355 Yield strength	
	f_y [*MPa*]	f_{yd} [*MPa*]
$t \leq 16$	355	309
$16 < t \leq 40$	345	300
$40 < t \leq 63$	335	291
$63 < t \leq 80$	325	283

Table 0-2: Ultimate tensile strength [MPa]

Thickness [*mm*]	ULS S355 (DnV_1 NV36) ultimate Tensile strength	
	f_u [*MPa*]	f_{ud} [*MPa*]
$t \leq 100$	490	377

Table 0-3: Characteristic Material values for steel in general

Steel	
Modulus of elasticity, E [*MPa*]	210000
Shear modulus, G [*MPa*]	81000
Density, ρ [kg/m^3]	7850
Poisson's ratio, ν [-]	0.3

Appendix 4 – Coordinate Transformation and Vector Identities

Operation	Cartesian coordinates (x,y,z)	Cylindrical coordinates (r,θ,z)
Definition of coordinates	$r=\sqrt{x^2+y^2}$ $\theta=\arctan(y/x)$ $z=z$	$x=r\cos\theta$ $y=r\sin\theta$ $z=z$
Definition of unit vectors	$\vec{i_r}=\frac{x}{r}\vec{i}+\frac{y}{r}\vec{j}$ $\vec{i_\theta}=-\frac{y}{r}\vec{i}+\frac{x}{r}\vec{j}$ $\vec{i_z}=\vec{k}$	$\vec{i}=\cos\theta\vec{i_r}-\sin\theta\vec{i_\theta}$ $\vec{j}=\sin\theta\vec{i_r}+\cos\theta\vec{i_\theta}$ $\vec{k}=\vec{i_z}$
Vector field A	$A_x\vec{i}+A_y\vec{j}+A_z\vec{k}$	$A_r\vec{i_r}+A_\theta\vec{i_\theta}+A_z\vec{i_z}$
Gradient ∇f	$\frac{\partial f}{\partial x}\vec{i}+\frac{\partial f}{\partial y}\vec{j}+\frac{\partial f}{\partial z}\vec{k}$	$\frac{\partial f}{\partial r}\vec{i_r}+\frac{1}{r}\frac{\partial f}{\partial\theta}\vec{i_\theta}+\frac{\partial f}{\partial z}\vec{i_z}$
Divergence $\nabla\cdot A$	$\frac{\partial A_x}{\partial x}+\frac{\partial A_y}{\partial y}+\frac{\partial A_z}{\partial z}$	$\frac{1}{r}\frac{\partial(rA_r)}{\partial r}+\frac{1}{r}\frac{\partial A_\theta}{\partial\theta}+\frac{\partial A_z}{\partial z}$
Laplace operator $\Delta f=\nabla^2 f$	$\frac{\partial^2 f}{\partial x^2}+\frac{\partial^2 f}{\partial y^2}+\frac{\partial^2 f}{\partial z^2}$	$\frac{1}{r}\frac{\partial}{\partial r}\left(r\frac{\partial f}{\partial r}\right)+\frac{1}{r^2}\frac{\partial^2 f}{\partial\theta^2}+\frac{\partial^2 f}{\partial z^2}$ $=\frac{\partial^2 f}{\partial r^2}+\frac{1}{r}\frac{\partial f}{\partial r}+\frac{1}{r^2}\frac{\partial^2 f}{\partial\theta^2}+\frac{\partial^2 f}{\partial z^2}$
Vector Laplacian $\Delta A=\nabla^2 A$	$\Delta A_x\vec{i}+\Delta A_y\vec{j}+\Delta A_z\vec{k}$	$\left(\Delta A_r-\frac{A_r}{r^2}-\frac{2}{r^2}\frac{\partial A_\theta}{\partial\theta}\right)\vec{i_r}+\left(\Delta A_\theta-\frac{A_\theta}{r^2}+\frac{2}{r^2}\frac{\partial A_\theta}{\partial\theta}\right)\vec{i_\theta}$ $+(\Delta A_z)\vec{i_z}$
Differential displacement l	$dl=dx\vec{i}+dy\vec{j}+dz\vec{k}$	$dl=dr\vec{i_r}+rd\theta\vec{i_\theta}+dz\vec{i_z}$
Differential normal area dS	$dS=dydz\vec{i}+dxdz\vec{j}+dxdy\vec{k}$	$dS=rd\theta dz\vec{i_r}+drdz\vec{i_\theta}+rdrd\theta\vec{i_z}$
Differential volume dV	$dV=dxdydz$	$dV=rdrd\theta dz$

Non-trivial calculation rules:

1. $div\ grad\ f=\nabla\cdot(\nabla f)=\nabla^2 f=\Delta f$ (Laplacian)
2. $curl\ grad\ f=\nabla\times(\nabla f)=0$
3. $div\ curl\ A=\nabla\cdot(\nabla\times A)=0$
4. $curl\ curl\ A=\nabla\times(\nabla\times A)=\nabla(\nabla\cdot A)-\nabla^2 A\ \Leftrightarrow\ \nabla^2 A=\Delta A=\nabla(\nabla\cdot A)-\nabla\times(\nabla\times A)$

REF URL: http://en.wikipedia.org/wiki/Nabla_in_cylindrical_and_spherical_coordinates

Appendix 5 – Basic Field Equations in Cartesian and Cylindrical Coordinates

For convenience, the basic three-dimensional field equations of elasticity are listed here for Cartesian and cylindrical coordinate systems. This will eliminate searching for these results in the text. Cylindrical coordinates are related to the basic Cartesian system, as shown in the figure to the right. The basic field equations are given in the table below for the three axial components. Obtained from Appendix A in [Sadd M.H, 2004].

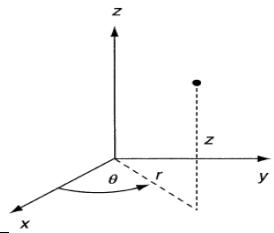

Cartesian Coordinatres	Cylindrical Coordinates
Strain-Displcement Relations	
$e_x = \frac{\partial u}{\partial x},\ e_y = \frac{\partial v}{\partial y},\ e_z = \frac{\partial w}{\partial z}$ $e_{xy} = \frac{1}{2}\left(\frac{\partial u}{\partial y} + \frac{\partial v}{\partial x}\right)$ $e_{yz} = \frac{1}{2}\left(\frac{\partial v}{\partial z} + \frac{\partial w}{\partial y}\right)$ $e_{zx} = \frac{1}{2}\left(\frac{\partial w}{\partial x} + \frac{\partial u}{\partial z}\right)$	$e_r = \frac{\partial u_r}{\partial r},\ e_\theta = \frac{1}{r}\left(u_r + \frac{\partial u_\theta}{\partial \theta}\right),\ e_z = \frac{\partial u_z}{\partial z}$ $e_{r\theta} = \frac{1}{2}\left(\frac{1}{r}\frac{\partial u_r}{\partial \theta} + \frac{\partial u_\theta}{\partial r} - \frac{u_\theta}{r}\right)$ $e_{\theta z} = \frac{1}{2}\left(\frac{\partial u_\theta}{\partial z} + \frac{1}{r}\frac{\partial u_z}{\partial \theta}\right)$ $e_{zr} = \frac{1}{2}\left(\frac{\partial u_r}{\partial z} + \frac{\partial u_z}{\partial r}\right)$
Equilibrium Equations	
$\frac{\partial \sigma_x}{\partial x} + \frac{\partial \tau_{yx}}{\partial y} + \frac{\partial \tau_{zx}}{\partial z} + F_x = 0$ $\frac{\partial \tau_{xy}}{\partial x} + \frac{\partial \sigma_y}{\partial y} + \frac{\partial \tau_{zy}}{\partial z} + F_y = 0$ $\frac{\partial \tau_{xz}}{\partial x} + \frac{\partial \tau_{yz}}{\partial y} + \frac{\partial \sigma_z}{\partial z} + F_z = 0$	$\frac{\partial \sigma_r}{\partial r} + \frac{1}{r}\frac{\partial \tau_{r\theta}}{\partial \theta} + \frac{\partial \tau_{rz}}{\partial z} + \frac{1}{r}(\sigma_r - \sigma_\theta) + F_r = 0$ $\frac{\partial \tau_{r\theta}}{\partial r} + \frac{1}{r}\frac{\partial \sigma_\theta}{\partial \theta} + \frac{\partial \tau_{\theta z}}{\partial z} + \frac{2}{r}\tau_{r\theta} + F_\theta = 0$ $\frac{\partial \tau_{rz}}{\partial r} + \frac{1}{r}\frac{\partial \tau_{\theta z}}{\partial \theta} + \frac{\partial \sigma_z}{\partial z} + \frac{1}{r}\tau_{rz} + F_z = 0$
Hooke's Law	
$\sigma_x = \lambda(e_x + e_y + e_z) + 2\mu e_x$ $\sigma_y = \lambda(e_x + e_y + e_z) + 2\mu e_y$ $\sigma_z = \lambda(e_x + e_y + e_z) + 2\mu e_z$ $\tau_{xy} = 2\mu e_{xy}$ $\tau_{yz} = 2\mu e_{yz}$ $\tau_{zx} = 2\mu e_{zx}$ $e_x = \frac{1}{E}[\sigma_x - \nu(\sigma_y + \sigma_z)]$ $e_y = \frac{1}{E}[\sigma_y - \nu(\sigma_z + \sigma_x)]$ $e_z = \frac{1}{E}[\sigma_z - \nu(\sigma_x + \sigma_y)]$ $e_{xy} = \frac{1+\nu}{E}\tau_{xy}$ $e_{yz} = \frac{1+\nu}{E}\tau_{yz}$ $e_{zx} = \frac{1+\nu}{E}\tau_{zx}$	$\sigma_r = \lambda(e_r + e_\theta + e_z) + 2\mu e_r$ $\sigma_\theta = \lambda(e_r + e_\theta + e_z) + 2\mu e_\theta$ $\sigma_z = \lambda(e_r + e_\theta + e_z) + 2\mu e_z$ $\tau_{r\theta} = 2\mu e_{r\theta}$ $\tau_{\theta z} = 2\mu e_{\theta z}$ $\tau_{zr} = 2\mu e_{zr}$ $e_r = \frac{1}{E}[\sigma_r - \nu(\sigma_\theta + \sigma_z)]$ $e_\theta = \frac{1}{E}[\sigma_\theta - \nu(\sigma_z + \sigma_r)]$ $e_z = \frac{1}{E}[\sigma_z - \nu(\sigma_r + \sigma_\theta)]$ $e_{r\theta} = \frac{1+\nu}{E}\tau_{r\theta}$ $e_{\theta z} = \frac{1+\nu}{E}\tau_{\theta z}$ $e_{zr} = \frac{1+\nu}{E}\tau_{zr}$
Equilibrium Equations in Terms of Displacements	
$\mu\nabla^2 u + (\lambda+\mu)\frac{\partial}{\partial x}\left(\frac{\partial u}{\partial x} + \frac{\partial v}{\partial y} + \frac{\partial w}{\partial z}\right) + F_x = 0$ $\mu\nabla^2 v + (\lambda+\mu)\frac{\partial}{\partial y}\left(\frac{\partial u}{\partial x} + \frac{\partial v}{\partial y} + \frac{\partial w}{\partial z}\right) + F_y = 0$ $\mu\nabla^2 w + (\lambda+\mu)\frac{\partial}{\partial z}\left(\frac{\partial u}{\partial x} + \frac{\partial v}{\partial y} + \frac{\partial w}{\partial z}\right) + F_z = 0$	$\mu\left(\nabla^2 u_r - \frac{u_r}{r^2} - \frac{2}{r^2}\frac{\partial u_\theta}{\partial \theta}\right) + (\lambda+\mu)\frac{\partial}{\partial r}\left(\frac{1}{r}\frac{\partial}{\partial r}(ru_r) + \frac{1}{r}\frac{\partial u_\theta}{\partial \theta} + \frac{\partial u_z}{\partial z}\right) + F_r = 0$ $\mu\left(\nabla^2 u_\theta - \frac{u_\theta}{r^2} + \frac{2}{r^2}\frac{\partial u_r}{\partial \theta}\right) + (\lambda+\mu)\frac{1}{r}\frac{\partial}{\partial \theta}\left(\frac{1}{r}\frac{\partial}{\partial r}(ru_r) + \frac{1}{r}\frac{\partial u_\theta}{\partial \theta} + \frac{\partial u_z}{\partial z}\right) + F_\theta = 0$ $\mu\nabla^2 u_z + (\lambda+\mu)\frac{\partial}{\partial z}\left(\frac{1}{r}\frac{\partial}{\partial r}(ru_r) + \frac{1}{r}\frac{\partial u_\theta}{\partial \theta} + \frac{\partial u_z}{\partial z}\right) + F_z = 0$
Equations of Motion in Terms of Displacements with no Body Forces	
$\mu\Delta u_x + (\lambda+\mu)\frac{\partial}{\partial x}\left(\frac{\partial u_x}{\partial x} + \frac{\partial u_y}{\partial y} + \frac{\partial u_z}{\partial z}\right) - \rho\frac{\partial^2 u_x}{\partial t^2} = 0$ $\mu\Delta u_y + (\lambda+\mu)\frac{\partial}{\partial y}\left(\frac{\partial u_x}{\partial x} + \frac{\partial u_y}{\partial y} + \frac{\partial u_z}{\partial z}\right) - \rho\frac{\partial^2 u_y}{\partial t^2} = 0$ $\mu\Delta u_z + (\lambda+\mu)\frac{\partial}{\partial z}\left(\frac{\partial u_x}{\partial x} + \frac{\partial u_y}{\partial y} + \frac{\partial u_z}{\partial z}\right) - \rho\frac{\partial^2 u_z}{\partial t^2} = 0$	$\mu\left(\nabla^2 u_r - \frac{u_r}{r^2} - \frac{2}{r^2}\frac{\partial u_\theta}{\partial \theta}\right) + (\lambda+\mu)\frac{\partial}{\partial r}\left(\frac{1}{r}\frac{\partial(ru_r)}{\partial r} + \frac{1}{r}\frac{\partial u_\theta}{\partial \theta} + \frac{\partial u_z}{\partial z}\right) - \rho\frac{\partial^2 u_r}{\partial t^2} = 0$ $\mu\left(\nabla^2 u_\theta - \frac{u_\theta}{r^2} + \frac{2}{r^2}\frac{\partial u_r}{\partial \theta}\right) + (\lambda+\mu)\frac{1}{r}\frac{\partial}{\partial \theta}\left(\frac{1}{r}\frac{\partial(ru_r)}{\partial r} + \frac{1}{r}\frac{\partial u_\theta}{\partial \theta} + \frac{\partial u_z}{\partial z}\right) - \rho\frac{\partial^2 u_\theta}{\partial t^2} = 0$ $\mu\nabla^2 u_z + (\lambda+\mu)\frac{\partial}{\partial z}\left(\frac{1}{r}\frac{\partial(ru_r)}{\partial r} + \frac{1}{r}\frac{\partial u_\theta}{\partial \theta} + \frac{\partial u_z}{\partial z}\right) - \rho\frac{\partial^2 u_z}{\partial t^2} = 0$

Appendix 6 – Complex Number Representation of Harmonic Motion

In general, vector representation of harmonic motion requires the description of both the horizontal and vertical components, which is why it is more convenient to use a complex number representation [Rao S., 2004]. This states that harmonic motion can be seen as projection of the tip of a rotating vector, say $\vec{X}$, which can be represented as a complex number, illustrated in the figure below and expressed in (3.33).

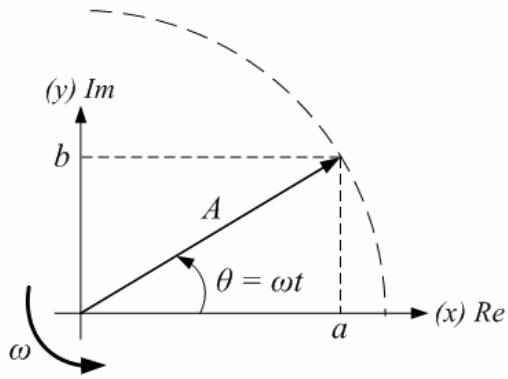

Figure 0-1: Harmonic motion of a rotating vector represented by a complex number.

$$\vec{X} = a + ib \tag{3.33}$$

The rotating vector $\vec{X}$ in (3.33) is composed of a real and an imaginary part, *a* and *b*, corresponding to the *x* and *y* components of this vector and $i = \sqrt{-1}$. If *A* is the length of the vector $\vec{X}$, i.e. $A = \sqrt{a^2 + b^2}$, the vector in (3.33) can also be expressed as

$$\vec{X} = A\cos\theta + iA\sin\theta \tag{3.34}$$

Expanding the trigonometric parts in (3.34) in a series and noting that $\theta = \omega t$, this equation reduces to

$$\vec{X}(t) = A\left(\cos\omega t + i\sin\omega t\right) = Ae^{i\omega t} \quad \text{or} \quad \vec{X}(t) = A\left(\cos\omega t - i\sin\omega t\right) = Ae^{-i\omega t} \tag{3.35}$$

where ω is the angular frequency, measuring the rate of rotation. The left expression in (3.35) corresponds to counter-clockwise rotation, as shown in (3.35), while the right one expresses the clockwise rotation of vector $\vec{X}$ as a function of time *t*. A full derivation can be found in e.g. [Rao S., 2004].

Appendix 7 – Derivation of the Displacement Field

The displacement field $\vec{u}(r,\theta,z)=\left(u_r,u_\theta,u_z\right)$ can be expressed in terms of 3 potentials as:

$$\vec{u}(r,\theta,z)=\nabla\varphi(r,\theta,z)+\nabla\times\vec{e}_3\psi_1(r,\theta,z)+\nabla\times\nabla\times\vec{e}_3\psi_2(r,\theta,z)$$

The following guesses are assumed for the 3 potentials:

$$\varphi\left(r,\theta,z\right)=\tilde{\varphi}(r,z)\cos\theta \quad ; \quad \psi_1\left(r,\theta,z\right)=\tilde{\psi}_1(r,z)\sin\theta \quad ; \quad \psi_2\left(r,\theta,z\right)=\tilde{\psi}_2(r,z)\cos\theta$$ [i]

The first term in (1) is obtained as follows:

$$\nabla\varphi(r,\theta,z)=\nabla\tilde{\varphi}(r,z)\cos\theta=\left(\frac{\partial\tilde{\varphi}}{\partial r}\cos\theta\right)\vec{i}_r+\left(\frac{1}{r}\frac{\partial\tilde{\varphi}}{\partial\theta}\cos\theta\right)\vec{i}_\theta+\left(\frac{\partial\tilde{\varphi}}{\partial z}\cos\theta\right)\vec{i}_z$$
$$=\underline{\left(\frac{\partial\tilde{\varphi}}{\partial r}\cos\theta\right)\vec{i}_r+\left(-\frac{1}{r}\tilde{\varphi}\sin\theta\right)\vec{i}_\theta+\left(\frac{\partial\tilde{\varphi}}{\partial z}\cos\theta\right)\vec{i}_z}$$

The second term in (1) is obtained as follows:

$$\nabla\times e_3\psi_1(r,\theta,z)=\nabla\times(0,0,\tilde{\psi}_1(r,z)\sin\theta)=\begin{vmatrix}\vec{i}_r & \vec{i}_\theta & \vec{i}_z\\ \frac{\partial}{\partial r} & \frac{1}{r}\frac{\partial}{\partial\theta} & \frac{\partial}{\partial z}\\ 0 & 0 & \tilde{\psi}_1(r,z)\sin\theta\end{vmatrix}$$
$$=\left(\frac{1}{r}\frac{\partial\tilde{\psi}_1(r,z)}{\partial\theta}\sin\theta-0\right)\vec{i}_r+\left(0-\frac{\partial\tilde{\psi}_1(r,z)}{\partial r}\sin\theta\right)\vec{i}_\theta+\frac{1}{r}(0-0)\vec{i}_z$$
$$=\underline{\left(\frac{1}{r}\tilde{\psi}_1(r,z)\cos\theta\right)\vec{i}_r+\left(-\frac{\partial\tilde{\psi}_1(r,z)}{\partial r}\sin\theta\right)\vec{i}_\theta}$$

The third term in (1) is obtained as follows:

$$\nabla\times e_3\psi_2(r,z)=\nabla\times(0,0,\tilde{\psi}_2(r,z)\cos\theta)=\begin{vmatrix}\vec{i}_r & \vec{i}_\theta & \vec{i}_z\\ \frac{\partial}{\partial r} & \frac{1}{r}\frac{\partial}{\partial\theta} & \frac{\partial}{\partial z}\\ 0 & 0 & \tilde{\psi}_2(r,z)\cos\theta\end{vmatrix}$$

The first curl operation:
$$=\left(\frac{1}{r}\frac{\partial\tilde{\psi}_2(r,z)}{\partial\theta}\cos\theta-0\right)\vec{i}_r-\left(\frac{\partial\tilde{\psi}_2(r,z)}{\partial r}\cos\theta-0\right)\vec{i}_\theta+\frac{1}{r}(0-0)\vec{i}_z$$
$$=\left(-\frac{1}{r}\tilde{\psi}_2(r,z)\sin\theta\right)\vec{i}_r+\left(-\frac{\partial\tilde{\psi}_2(r,z)}{\partial r}\cos\theta\right)\vec{i}_\theta$$

The final curl operation:

$$\nabla\times\nabla\times e_3\psi_2(r,z)=\nabla\times\left(-\frac{1}{r}\tilde{\psi}_2(r,z)\sin\theta,-\frac{\partial\tilde{\psi}_2(r,z)}{\partial r}\cos\theta,0\right)$$

$$=\begin{vmatrix}\vec{i}_r & \vec{i}_\theta & \vec{i}_z\\ \frac{\partial}{\partial r} & \frac{1}{r}\frac{\partial}{\partial\theta} & \frac{\partial}{\partial z}\\ -\frac{1}{r}\tilde{\psi}_2(r,z)\sin\theta & -\frac{\partial\tilde{\psi}_2(r,z)}{\partial r}\cos\theta & 0\end{vmatrix}$$

$$=\left(0+\frac{\partial^2\tilde{\psi}_2(r,z)}{\partial z\partial r}\cos\theta\right)\vec{i}_r-\left(0+\frac{1}{r}\frac{\partial\tilde{\psi}_2(r,z)}{\partial z}\sin\theta\right)\vec{i}_\theta+\left(-\frac{\partial^2\tilde{\psi}_2(r,z)}{\partial r^2}\cos\theta+\frac{1}{r^2}\frac{\partial\tilde{\psi}_2(r,z)}{\partial\theta}\sin\theta\right)\vec{i}_z$$

$$=\left(\frac{\partial^2\tilde{\psi}_2(r,z)}{\partial r\partial z}\cos\theta\right)\vec{i}_r+\left(-\frac{1}{r}\frac{\partial\tilde{\psi}_2(r,z)}{\partial z}\sin\theta\right)\vec{i}_\theta$$

$$+\left(-\frac{1}{r}\frac{\partial\tilde{\psi}_2(r,z)}{\partial r}\cos\theta-\frac{\partial^2\tilde{\psi}_2(r,z)}{\partial r^2}\cos\theta+\frac{1}{r^2}\tilde{\psi}_2(r,z)\cos\theta\right)\vec{i}_z$$

The displacement field becomes:

$$\begin{aligned}\vec{u}(r,\theta,z)&=\nabla\varphi(r,\theta,z)+\nabla\times\vec{e}_3\psi_1(r,\theta,z)+\nabla\times\nabla\times\vec{e}_3\psi_2(r,\theta,z)\\&=\nabla\tilde{\varphi}(r,z)\cos\theta+\nabla\times\vec{e}_3\tilde{\psi}_1(r,z)\sin\theta+\nabla\times\nabla\times\vec{e}_3\tilde{\psi}_2(r,z)\cos\theta\\&=\left(\frac{\partial\tilde{\varphi}(r,z)}{\partial r}\cos\theta\right)\vec{i}_r+\left(-\frac{1}{r}\tilde{\varphi}(r,z)\sin\theta\right)\vec{i}_\theta+\left(\frac{\partial\tilde{\varphi}(r,z)}{\partial z}\cos\theta\right)\vec{i}_z\\&+\left(\frac{1}{r}\tilde{\psi}_1(r,z)\cos\theta\right)\vec{i}_r+\left(-\frac{\partial\tilde{\psi}_1(r,z)}{\partial r}\sin\theta\right)\vec{i}_\theta+0\vec{i}_z\\&+\left(\frac{\partial^2\tilde{\psi}_2(r,z)}{\partial r\partial z}\cos\theta\right)\vec{i}_r+\left(-\frac{1}{r}\frac{\partial\tilde{\psi}_2(r,z)}{\partial z}\sin\theta\right)\vec{i}_\theta\\&+\left(-\frac{1}{r}\frac{\partial\tilde{\psi}_2(r,z)}{\partial r}\cos\theta-\frac{\partial^2\tilde{\psi}_2(r,z)}{\partial r^2}\cos\theta+\frac{1}{r^2}\tilde{\psi}_2(r,z)\cos\theta\right)\vec{i}_z\end{aligned}$$

The displacement components are finally obtained by summing the i_r, i_θ, and i_z vectors for the *r*, *theta* and the *z* component.

Appendix 8 – Galerkin Averaging

In order to obtain the 3 unknown potentials the following guesses are assumed, noticing that the θ dependence is already factored out:

$$\varphi(r,\theta,z)=\tilde{\varphi}(r,z)\cos\theta=\tilde{\varphi}_0(r)\sin\frac{\pi z}{L}\cos\theta\Rightarrow\tilde{\varphi}(r,z)=\tilde{\varphi}_0(r)\sin\frac{\pi z}{L}$$
$$\psi_1(r,\theta,z)=\tilde{\psi}_1(r,z)\sin\theta=\tilde{\psi}_{1,0}(r)\sin\frac{\pi z}{L}\sin\theta\Rightarrow\tilde{\psi}_1(r,z)=\tilde{\psi}_{1,0}(r)\sin\frac{\pi z}{L}$$
$$\psi_2(r,\theta,z)=\tilde{\psi}_2(r,z)\cos\theta=\tilde{\psi}_{2,0}(r)\cos\frac{\pi z}{L}\cos\theta\Rightarrow\tilde{\psi}_2(r,z)=\tilde{\psi}_{2,0}(r)\cos\frac{\pi z}{L}$$

With new guesses we have for the circumferential displacement:

$$\begin{aligned}u_\theta&=\left(-\frac{1}{r}\tilde{\varphi}(r,z)-\frac{\partial\tilde{\psi}_1(r,z)}{\partial r}-\frac{1}{r}\frac{\partial\tilde{\psi}_2(r,z)}{\partial z}\right)\sin\theta\\&=\left(-\frac{1}{r}\tilde{\varphi}_0(r)\sin\frac{\pi z}{L}-\frac{\partial}{\partial r}\tilde{\psi}_{1,0}(r)\sin\frac{\pi z}{L}-\frac{1}{r}\frac{\partial}{\partial z}\tilde{\psi}_{2,0}(r)\cos\frac{\pi z}{L}\right)\sin\theta\\&=\left(-\frac{1}{r}\tilde{\varphi}_0(r)-\frac{\partial}{\partial r}\tilde{\psi}_{1,0}(r)+\frac{\pi}{Lr}\tilde{\psi}_{2,0}(r)\right)\sin\frac{\pi z}{L}\sin\theta\end{aligned}$$

Applying the boundary condition gives:

$$u_\theta=u_\theta^*\Leftrightarrow\left(-\frac{1}{r}\tilde{\varphi}_0(r)-\frac{\partial}{\partial r}\tilde{\psi}_{1,0}(r)+\frac{\pi}{Lr}\tilde{\psi}_{2,0}(r)\right)\sin\frac{\pi z}{L}\sin\theta=w_0\sin\theta\left(\frac{z}{L}\right)\Leftrightarrow$$
$$\left(-\frac{1}{r}\tilde{\varphi}_0(r)-\frac{\partial}{\partial r}\tilde{\psi}_{1,0}(r)+\frac{\pi}{Lr}\tilde{\psi}_{2,0}(r)\right)\sin\frac{\pi z}{L}=2w_0\left(\frac{z}{L}\right)$$

The Galerkin averaging for u_θ^* is preformed by multiplying by *sine* function again and integrating as follows:

$$\int_{-L/2}^{L/2}\left(-\frac{1}{r}\tilde{\varphi}_0(r)-\frac{\partial\tilde{\psi}_{1,0}(r)}{\partial r}+\frac{\pi}{Lr}\tilde{\psi}_{2,0}(r)\right)\sin^2\left(\frac{\pi z}{L}\right)dz=\int_{-L/2}^{L/2}2w_0\frac{z}{L}\sin\left(\frac{\pi z}{L}\right)dz\Leftrightarrow$$
$$\left(-\frac{1}{r}\tilde{\varphi}_0(r)-\frac{\partial\tilde{\psi}_{1,0}(r)}{\partial r}+\frac{\pi}{Lr}\tilde{\psi}_{2,0}(r)\right)\int_{-L/2}^{L/2}\sin^2\left(\frac{\pi z}{L}\right)dz=w_0\frac{1}{L}\int_{-L/2}^{L/2}z\sin\left(\frac{\pi z}{L}\right)dz\Leftrightarrow$$
$$-\frac{L}{2r}\tilde{\varphi}_0(r)-\frac{L}{2}\frac{\partial\tilde{\psi}_{1,0}(r)}{\partial r}+\frac{\pi}{2r}\tilde{\psi}_{2,0}(r)=w_0\frac{4L}{\pi^2}\Leftrightarrow-\frac{1}{r}\tilde{\varphi}_0(r)-\frac{\partial\tilde{\psi}_{1,0}(r)}{\partial r}+\frac{\pi}{Lr}\tilde{\psi}_{2,0}(r)=w_0\frac{8}{\pi^2}$$

For u_z there is no need for integration as it is homogeneous giving:

$$u_z = u_z^* \Leftrightarrow \left(\frac{\partial \tilde{\varphi}(r,z)}{\partial z} - \frac{1}{r}\frac{\partial \tilde{\psi}_2(r,z)}{\partial r} - \frac{\partial^2 \tilde{\psi}_2(r,z)}{\partial r^2} + \frac{1}{r^2}\tilde{\psi}_2(r,z) \right)\cos\theta = 0 \Leftrightarrow$$

$$\left(\frac{\partial}{\partial z}\tilde{\varphi}_0(r)\sin\frac{\pi z}{L} - \frac{1}{r}\frac{\partial}{\partial r}\tilde{\psi}_{2,0}(r)\cos\frac{\pi z}{L} - \frac{\partial^2}{\partial r^2}\tilde{\psi}_{2,0}(r)\cos\frac{\pi z}{L} + \frac{1}{r^2}\tilde{\psi}_{2,0}(r)\cos\frac{\pi z}{L} \right)\cos\theta = 0 \Leftrightarrow$$

$$\left(\frac{\pi}{L}\tilde{\varphi}_0(r) - \frac{1}{r}\frac{\partial}{\partial r}\tilde{\psi}_{2,0}(r) - \frac{\partial^2 \tilde{\psi}_{2,0}(r)}{\partial r^2} + \frac{1}{r^2}\tilde{\psi}_{2,0}(r) \right)\cos\theta\cos\frac{\pi z}{L} = 0 \Leftrightarrow$$

$$\frac{\pi}{L}\tilde{\varphi}_0(r) - \frac{1}{r}\frac{\partial}{\partial r}\tilde{\psi}_{2,0}(r) - \frac{\partial^2 \tilde{\psi}_{2,0}(r)}{\partial r^2} + \frac{1}{r^2}\tilde{\psi}_{2,0}(r) = 0$$

Finally, the three boundary equations for the surface S_2 and S_4, and in terms of r only, are:

For S_1:

$$u_r = u_{r1}^* \Leftrightarrow \frac{\partial \tilde{\varphi}_0(r)}{\partial r} + \frac{1}{r}\tilde{\psi}_{1,0}(r) - \frac{\pi}{L}\frac{\partial \tilde{\psi}_{2,0}(r)}{\partial r} = 0$$

$$u_\theta = u_{\theta 1}^* \Leftrightarrow -\frac{1}{r}\tilde{\varphi}_0(r) - \frac{\partial \tilde{\psi}_{1,0}(r)}{\partial r} + \frac{\pi}{Lr}\tilde{\psi}_{2,0}(r) = 0$$

$$u_z = u_{z1}^* \Leftrightarrow \frac{\pi}{L}\tilde{\varphi}_0(r) - \frac{1}{r}\frac{\partial \tilde{\psi}_{2,0}(r)}{\partial r} - \frac{\partial^2 \tilde{\psi}_{2,0}(r)}{\partial r^2} + \frac{1}{r^2}\tilde{\psi}_{2,0}(r) = 0$$

For S_2:

$$u_r = u_{r2}^* \Leftrightarrow \frac{\partial \tilde{\varphi}_0(r)}{\partial r} + \frac{1}{r}\tilde{\psi}_{1,0}(r) - \frac{\pi}{L}\frac{\partial \tilde{\psi}_{2,0}(r)}{\partial r} = w_0\frac{4}{\pi^2}$$

$$u_\theta = u_{\theta 2}^* \Leftrightarrow -\frac{1}{r}\tilde{\varphi}_0(r) - \frac{\partial \tilde{\psi}_{1,0}(r)}{\partial r} + \frac{\pi}{Lr}\tilde{\psi}_{2,0}(r) = w_0\frac{4}{\pi^2}$$

$$u_z = u_{z2}^* \Leftrightarrow \frac{\pi}{L}\tilde{\varphi}_0(r) - \frac{1}{r}\frac{\partial \tilde{\psi}_{2,0}(r)}{\partial r} - \frac{\partial^2 \tilde{\psi}_{2,0}(r)}{\partial r^2} + \frac{1}{r^2}\tilde{\psi}_{2,0}(r) = 0$$

Appendix 9 – Characteristics of Bessel's Ordinary and Modified Functions

The general solutions of the three-dimensional equations of equilibrium for elasticity theory in cylindrical coordinates are in many cases expressed in terms of Bessel functions, i.e. cylindrical or harmonic functions. They are used in the solution of boundary-value problems for deformable bodies with cylindrical bounding surfaces, for example, static problems for circular geometries subjected to axisymmetric or nonaxisymmetric forces, which can be represented in the form of Fourier series.

In a majority of cases the solution of the indicated class of boundary-value problems requires calculations of the modified Bessel functions $I_n(r)$ and $K_n(r)$ of large argument r and order n. The two types are described below.

Ordinary Bessel functions *J* and *Y*:

Bessel functions of the first kind, $J_n(r)$, are solutions of Bessel's differential equation which are finite at $r = 0$ for n being an integer or non-negative. Bessel functions of the second kind, $Y_n(r)$, are solutions which are singular (infinite) at $r = 0$. So, J_n and Y_n are the Bessel functions of the first and second kind, respectively, that satisfy the ordinary Bessel's equation of the form (in Cartesian coordinates):

$$x^2 \frac{d^2 y}{dx^2} + x \frac{dy}{dx} + (x^2 - n^2) y = 0$$

The ordinary Bessel functions are illustrated below.

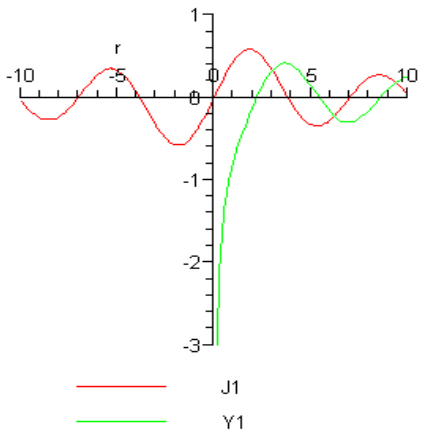

Above is a plot of $J(1,r)$ and $Y(1,r)$ in an interval $r = [-10;10]$.

Modified Bessel functions *I* and *K*:

The Bessel functions are also valid for complex arguments r, as well as in case of a purely imaginary argument. In such case, the solutions to the Bessel equation are called the modified Bessel functions I_n and K_n of

the first and second kind, respectively. They are chosen to be real-valued for real arguments r. They are the two linearly independent solutions to the modified Bessel's equation (in Cartesian coordinates):

$$x^2 \frac{d^2 y}{dx^2} + x \frac{dy}{dx} - (x^2 + n^2) y = 0$$

Unlike the ordinary Bessel functions J_n and Y_n, which are oscillating, I_n and K_n are exponentially growing and decaying functions, respectively. Like the ordinary Bessel function J_n, the function I_n goes to zero at $r = 0$ for $n > 0$ and is finite at $r = 0$ for $n = 0$. Analogously, K_n diverges at $r = 0$ just like Y_m. This is illustrated below.

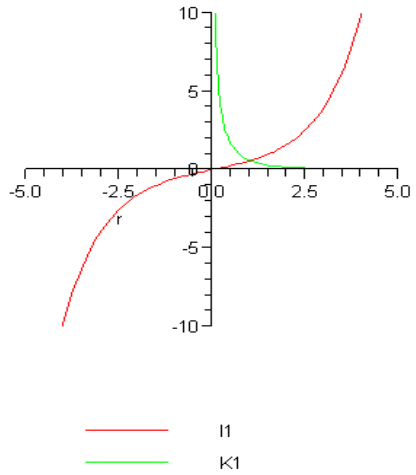

Above is a plot of $I(1,r)$ and $K(1,r)$ in an interval $r = [-5;5]$.

As it can be noticed the ordinary and modified Bessel equations only differ by the sign convention in the last term of the left hand side.